

Get back to work.

—Taschuk

University of Alberta

DISASSEMBLING GLANCING ANGLE DEPOSITED FILMS FOR
HIGH THROUGHPUT GROWTH SCALING ANALYSIS

by

JOSHUA MORGAN ARTHUR SIEWERT

A thesis submitted to the Faculty of Graduate Studies and Research in partial fulfilment of the
requirements for the degree of

MASTER OF SCIENCE

in

MICROSYSTEMS AND NANODEVICES

Department of Electrical and Computer Engineering

© Joshua Morgan Arthur Siewert

Fall 2012

Edmonton, Alberta

Permission is hereby granted to the University of Alberta Libraries to reproduce single copies of this thesis and to lend or sell such copies for private, scholarly or scientific research purposes only. Where the thesis is converted to, or otherwise made available in digital form, the University of Alberta will advise potential users of the thesis of these terms.

The author reserves all other publication and other rights in association with the copyright in the thesis and, except as herein before provided, neither the thesis nor any substantial portion thereof may be printed or otherwise reproduced in any material form whatsoever without the author's prior written permission.

To my mother and father,
for supporting, loving, and molding me.

ABSTRACT

Glancing angle deposition (GLAD) is a thin film fabrication technique capable of creating arrays of nanocolumns from numerous materials. Optimizing these films for applications requires an understanding of their growth, prompting research into the columns' growth scaling behaviour. Columns are generally represented with a power law, capturing broadening in an exponent p . Existing literature measurements of p are inconsistent and difficult to repeat, in part due to complex branching in many GLAD films and subjectivity in some existing techniques.

This thesis describes a new method of studying growth scaling by disassembling films into a solvent and dispersing them across a substrate, facilitating automated measurement from top-down scanning electron microscopy. Minimizing the uncertainty and subjectivity introduced by branching, optimized implementations may permit fully-automated high-throughput film characterization. Initial results track the influence of deposition rotation on broadening, presenting the first quantitative trend and potentially improving future nanostructure morphology control.

*I used to hate writing assignments, but now I enjoy them.
I realized that the purpose of writing is to inflate weak ideas,
obscure poor reasoning, and inhibit clarity.
With a little practice, writing can be an intimidating
and impenetrable fog!*

— Calvin (Bill Watterson)

ACKNOWLEDGMENTS

I would first and foremost like to thank my family—without their guidance, I would not be the person I am. This especially includes my handsome, stylish, and long-suffering brother, who’s endured me his entire life.

Though still a little upset that the members of the GLAD and ENL group didn’t appreciate my poster palettes¹, I want to thank them for making these past few years wonderful. Dr. Jeff (Zhifeng) Huang, for guiding me through my first summer in the group and getting me accustomed the research world. Graham Hunt and Allan Beaudry, for painful workouts, camaraderie, and occasionally questionable dub-step advice. Jocelyn Westwood, for making statistics almost bearable. Ryan Tucker and Al Lalany, just for being the stylish people that they are. Jon Kwan for that one time he wasn’t using my microwave when I needed it. Jason Sorge for reliably beating Taschuk at cards. And to all the others—Steven Jim, Dr. Nicole Beckers, Michael Thomas, Dr. Jeremy Sit, Martin Kupsta, Jaron van Dijken, Dr. Katie Krause, Dr. Jane Wang, Anthony Oko, Josh Krabbe—thanks for making the lab the wonderful place that it was.

I especially thank Dr. Brett for providing such an ideal research environment, abundantly supplied with the tools, support, and community required to produce quality work. Most of all, though, I’d like to thank him for his dedication to helping students with their larger goals in life, even in paths outside academia—in my case, providing the immense flexibility and support that allowed me to pursue entry into medicine. I consider myself extremely fortunate to have had such a supervisor.

Joshua LaForge deserves special mention for providing assistance, advice, arguments, and generally enduring me for the years of my tenure. May your students’ filenames be forever standardized.

Finally, I thank Dr. Taschuk, who bore the brunt of my squabbling and frippery for three years—more, counting meeting-induced premature ageing. I may have seemed impervious to improvement, and

¹ Note: if Taschuk passes off a violently yellow and green poster as mine, I’d like to make clear in print that this was the result of a tragic color-mapping glitch, rather than the clean, tasteful original. Evidence is available upon request.

was doubtless a common source of frustration. Yet you remained an unwavering source of advice, assistance, and necessary goading—upholding a relentless dedication to quality I will always respect and that I would do well to emulate. Thank you for being my mentor; sea-changes hereafter are at least partially your fault.

I would like to acknowledge funding from the Natural Sciences and Engineering Research Council of Canada, the University of Alberta, and Alberta Innovates Technology Futures, without which this work would not have been possible.

CONTENTS

1	INTRODUCTION	1
1.1	Motivation	1
1.2	Outline	2
2	THEORY AND BACKGROUND	4
2.1	Evaporation	4
2.1.1	The vacuum chamber	4
2.1.2	Electron beam evaporation	5
2.1.3	Adatoms and nucleation	6
2.2	Glancing Angle Deposition	8
2.2.1	The development of the GLAD Technique . . .	8
2.2.2	GLAD growth basics	9
2.2.3	Basic GLAD structures	11
2.3	GLAD growth scaling theory	15
2.3.1	Fractal concepts in surface growth	15
2.3.2	Universality classes	16
2.3.3	Applications to oblique angle deposition	21
2.3.4	Extension to vertical post morphology	23
2.3.5	Experimental studies of GLAD growth scaling .	24
2.4	Titanium dioxide	27
2.4.1	Applications	27
2.4.2	Chemical and physical properties	28
2.4.3	Stoichiometry of evaporated titania	28
2.4.4	GLAD Titania	29
3	MATERIALS AND METHODS	30
3.1	Sample fabrication	30
3.1.1	Substrate preparation	30
3.1.2	Deposition	31
3.1.3	Near-substrate defects	32
3.2	Rotation Stage	33
3.2.1	Design considerations	33
3.2.2	Phi-sweep considerations	35
3.3	Initial film characterization	36
3.3.1	Effect of pitch on gross nanostructure morphology	39
3.3.2	Film thickness control	42
3.3.3	Rotation stage morphologies	43
4	INITIAL MEASUREMENTS OF GROWTH SCALING	45
4.1	Cross-sectional broadening measurements	47
4.2	Automated top-down scaling measurements	49
4.2.1	Overall segmentation procedure	49

4.2.2	Thresholding considerations	51
4.2.3	Watershed considerations	54
4.2.4	Variation in automated data	54
4.3	Manual top-down scaling measurements	56
4.3.1	Average area vs. average diameter	56
4.3.2	Manual count considerations	57
4.3.3	Manual count results	57
4.4	Summary of initial measurements	58
5	DISASSEMBLY OF GLAD FILMS	61
5.1	Introduction and Motivation	61
5.2	The disassembly technique	64
5.2.1	Disassembly considerations	65
5.2.2	Dispersion considerations	69
5.2.3	Imaging considerations	72
5.2.4	Image analysis considerations	73
5.2.5	Final treatment parameters	77
5.3	Limitations on data validity	78
5.3.1	Resolution limits on width profile fitting	78
5.3.2	Fragmentation	81
5.4	Analysis	82
5.4.1	Evaluation of theoretical limits	84
5.5	Discussion	86
5.5.1	Comparison of measurement techniques	88
5.5.2	Potential improvements	91
5.6	Concluding remarks	91
6	CONCLUSIONS	93
6.1	Initial growth scaling measurements	93
6.2	Disassembly technique	94
6.3	Future work	94
6.4	Summary	95
	BIBLIOGRAPHY	96
A	APPENDIX: PROCEDURES	111
A.1	Disassembly procedure	111
B	APPENDIX: CODE	113
B.1	Rotation stage equivalent gamma calculations	113
B.1.1	Equivalent Gamma Optimization	114
B.2	Disassembly image analysis	118
B.3	Method comparison	120
C	APPENDIX: SCHEMATICS	131
C.1	Initial rotation stage schematics	131

LIST OF TABLES

Table 2.1	Summary of the growth universality classes described in this thesis, with the relevant continuum equations and scaling exponents.	20
Table 4.1	Power law fit parameters from cross-sectional width measurements.	48
Table 4.2	Summary of the p measurements of Chapter 4 based off top-down and cross-sectional SEMs; results are inconsistent.	59
Table 5.1	Data from Figure 5.16, describing the “full-height” posts used in final analysis of p	87

LIST OF FIGURES

Figure 2.1	The Movchan and Demchishin structure zone model, demonstrating the effect of substrate temperature on thin film morphology.	7
Figure 2.2	Diagram of the nanoscopic shadowing process that forms the basis of GLAD.	9
Figure 2.3	Demonstration of the control of the GLAD technique over nanostructure morphology.	10
Figure 2.4	Standard definitions of GLAD angles α and ϕ	11
Figure 2.5	Sampling of the various nanostructures GLAD can produce.	12

Figure 2.6	Substrate motion of the ϕ -sweep technique for minimizing column broadening.	13
Figure 2.7	Mechanics of the ϕ -sweep technique, demonstrating the creation of broadening-suppressing sub-segments.	14
Figure 2.8	The parallel correlation length, ξ_{\parallel} , of a rough, growing surface that indicates the lateral transfer of morphological information.	17
Figure 2.9	View of simulated oblique deposition from the perspective of the vapour flux, with edges governed by the 1D KPZ equation.	22
Figure 2.10	Partial summary of literature p measurements in GLAD vertical posts, indicating lack of clear consensus or trend.	25
Figure 2.11	Anomalous growth scaling observed in metals between $0.2T_m$ and $0.4T_m$, violating the proposed KPZ limit.	26
Figure 3.1	Near-substrate defects in samples deposited at high rates.	32
Figure 3.2	Flux angles and distances relevant to optimal placement of the rotation stage.	34
Figure 3.3	Picture of the rotation stage, constructed to allow parallel depositions at multiple pitches. . .	35
Figure 3.4	Rotation stage calibration plot for ϕ -sweep GLAD films, allowing selection of optimal γ rotation angles.	37
Figure 3.5	High-resolution and oblique-angle shots of TiO_2 $\alpha = 81^\circ$ GLAD films.	38
Figure 3.6	Films produced with pitch as a function of height, leading to helical and vertical post morphologies within the same column.	40

Figure 3.7	TiO ₂ GLAD film deposited at $\alpha = 81^\circ$ and a nominal pitch of 16.7 nm, demonstrating helical ripples on a vertical post morphology. . . .	41
Figure 3.8	Control chart of deposited film thicknesses in the experimental dataset.	42
Figure 3.9	Thickness variation across rotation stage shafts.	43
Figure 3.10	Defects caused by “jerking” gear motion in rotation stage at high pitch.	44
Figure 4.1	Measuring column thickness from cross-sectional SEMs.	46
Figure 4.2	Power law fits to broadening data taken from cross-sectional SEMs.	48
Figure 4.3	Correction of object size distribution to account for field of view boundaries.	50
Figure 4.4	Demonstration of the variation in threshold locations among human observers.	52
Figure 4.5	Fits to average particle diameter measured using automated particle analysis.	53
Figure 4.6	The effect of a watershed filter on binarized top-down SEMs, leading to over-segmentation of objects.	55
Figure 4.7	Estimates of mean column diameter from manual post-counts and automated measurements of top-down area fractions.	58
Figure 5.1	Comparison of existing literature methods of measuring growth scaling in GLAD thin films.	62
Figure 5.2	Film disassembly produced by scraping substrate with a razor.	65

Figure 5.3	Effect of disassembly solvent on the dispersion of nanocolumns.	67
Figure 5.4	Effect of spin speed on nanocolumn dispersion.	70
Figure 5.5	Unknown contamination appearing in some sample disassemblies.	71
Figure 5.6	Basic overview of the analysis process for a disassembled GLAD film.	72
Figure 5.7	Comparison of total variation and Gaussian blur approaches to noise removal.	74
Figure 5.8	Process used to generate post and background markers from disassembly SEMs.	75
Figure 5.9	Marker-based segmentation of film-disassembly images.	76
Figure 5.10	Large “islands” of helical posts maintaining in-film configuration after sonication treatment. .	78
Figure 5.11	Outline of post parameters that are accurately measured at a given resolution	80
Figure 5.12	Evidence of the fragmentation of individual GLAD posts during disassembly.	81
Figure 5.13	Joined fragments from the film top that replicate near-substrate post morphology.	82
Figure 5.14	Lengths and p values of the objects measured in a disassembled film, alongside selected examples of apparently extinct posts.	83
Figure 5.15	Examples of GLAD posts with length approximating film height that violate the theoretical KPZ limit.	84

Figure 5.16	Growth scaling of a TiO_2 ($\alpha = 81^\circ$) film, demonstrating a statistically significant pitch dependence.	85
Figure 5.17	Comparison of two methods of analysing p: fitting the power law to average column widths at different heights, and averaging the p values of numerous individual columns.	89
Figure 5.18	Histogram and normal probability plot of the distribution of p values recorded for columns in a 1 nm pitch film	90

INTRODUCTION

1.1 MOTIVATION

Nanotechnology is the manipulation of matter at a molecular scale, a technological feat that has only risen to prominence in recent decades. Engineered nanostructures show incredible potential, but have required the development of new and powerful tools both in their production and in their characterization. Continued progress in nanotechnology is founded on the continued improvement of these tools, extending our control over structures dwarfed even by the cells that comprise us.

Glancing angle deposition (GLAD) is one such tool. Without costly substrate patterning, GLAD uses traditional physical vapour deposition to produce arrays of individual nanostructures out of a vast and ever-growing variety of materials. Through simple substrate rotation, these structures can be sculpted with an astonishing degree of control, producing both the graceful spirals of helical morphologies and the stolid workhorse that is the vertical post film—vertically oriented nanorods that are common candidates for device applications.

Research into GLAD applications drives interest in better understanding their growth mechanics, allowing better control of their shape and properties. It is not surprising, then, that the GLAD vertical post has attracted much investigation. These posts broaden as they grow, an oft undesirable phenomenon that is not yet fully understood. Control of this broadening effect requires a more detailed understanding of its causes.

The width of these columns is thought to obey the power law

$$d = \omega_0 h^p \quad (1.1)$$

where d is the column width in nm, ω_0 is a material-dependant constant, h is the height above the substrate, and p is an exponent that describes the posts' growth scaling. Theory also predicts upper and lower limits on this value, which numerous groups have attempted to test experimentally. Results are inconsistent from group to group, difficult to repeat, and obey few clear trends, with data outside both predicted limits. Some factors potentially affecting p , such as the effect of substrate rotation rate on vertical post morphology, have not yet been quantitatively studied. A further obstacle to repeatability comes from the difficulty in manually distinguishing nanocolumns from their neighbours, especially in densely branching oxide films.

Better control of GLAD morphology requires better understanding of GLAD growth.

Broadening measurements are challenging, and literature results are inconsistent.

I aim to reduce the existing uncertainty in GLAD growth measurements, thus providing new insights into the engineering of vertical posts for device applications. First, I present a new method of measuring GLAD growth scaling that eliminates post measurement subjectivity by physically disassembling the film into component columns. Second, using this technique, I provide the first quantitative study of the effect of rotation rate on vertical post broadening, providing useful insight into its morphological control.

1.2 OUTLINE

CHAPTER 2 begins with a brief overview of evaporation, the deposition technique with which I fabricate thin films. This includes an outline of thin film growth mechanics and the initial clustering of deposited vapour into nuclei. I then provide a concise history of the GLAD technique alongside its basic properties and mechanism.

Growth scaling theory draws heavily from literature produced in the wake of Mandelbrot's popularization of fractal mathematics. A summary of the basic fractal concepts of film growth introduces two equations important to GLAD growth—the Kardar-Parisi-Zhang equation and the Mullins-Herring equation—using simple heuristic models. These are applied first to films deposited without substrate rotation, then to the case of the vertical post. This is accompanied by a summary of the existing literature, highlighting the lack of consensus in broadening measurements. Finally, I discuss the properties and relevance of titania, the material chosen to create the films in this thesis.

CHAPTER 3 summarizes fabrication methods I employ, as well as a basic characterization of film thickness and gross morphology. I also describe the use of a rotation stage permitting simultaneous deposition of multiple films to increase experimental throughput.

CHAPTER 4 contains my initial work in analysing GLAD broadening. I utilize two methods common in literature: the manual identification of columns from film cross-sections, and the measurement of column areas from top-down microscopy. Results are inconsistent, reflecting the existing scatter in literature values, and I briefly discuss the challenges inherent to both methods.

CHAPTER 5 describes a novel approach to the study of GLAD growth scaling in which the individual columns are ultrasonically shaken from the substrate into solution, then spun onto a polished silicon wafer. Imaged with a scanning electron microscope, these columns appear white on a dark background, facilitating automated measurement of column width all along their lengths. I study films at a variety of substrate rotation rates, providing the first quantitative insight into the control of vertical post morphology through rotation rate.

Finally, CHAPTER 6 summarizes the results produced in the thesis and provides suggestions for future work, building upon the disassembly technique.

THEORY AND BACKGROUND

This chapter focuses on a GLAD film of particular importance—the vertical post—and the study of its morphology. This includes its theoretical development, an overview of existing experimental literature on its growth scaling, and a justification of my focus on TiO_2 in this work. We begin with the concept of evaporation, the phenomenon of nucleation, and the GLAD technique that forms the basis for all of the work to follow.

2.1 EVAPORATION

Thin films are commonly produced through physical vapour deposition (PVD). As its name suggests, PVD is an atomistic process of vaporizing a source material and condensing the vapour on a substrate. Vaporization can be accomplished in a variety of ways. Sputtering, for instance, uses the momentum of high-energy ions to knock atoms free from a solid target. Pulsed laser deposition does so using intense blasts of electromagnetic energy [1, 2]. Evaporation, utilized in my work, relies on thermal excitation of a source in the vacuum chamber until surface molecules have sufficient kinetic energy to break free. With all other gases evacuated, these atoms are unimpeded and radiate from the melt source in straight trajectories [3]. Many of these atoms adsorb onto the surfaces they strike, eventually coating them in the source material.

Vaporised source material travels through vacuum to the substrate.

2.1.1 The vacuum chamber

The establishment of a high vacuum is crucial both to the purity of the evaporated film and to the directionality of the material impacting the substrate—collisions with residual gas particles scatter and randomize flight paths, potentially altering the properties of the deposited film.

Most evaporation systems use base pressures below 10^{-4} Torr, where particles are so sparse that they cease to behave as a fluid and enter the molecular flow regime [1]. Gas molecules essentially travel in straight lines until they elastically collide with one another or the chamber walls. The effect of the base pressure on deposition purity is straightforward: more residual gas particles result in more collisions with the substrate, and thus greater contamination of the growing film.

High vacuum produces pure films and long vapour flight paths.

Kinetic theory provides a useful metric for this contamination in the *monolayer formation time*, which measures how long it takes residual gas to completely coat a surface in a layer one molecule thick. This can be calculated at room temperature as

$$t = \frac{N_s}{n \sqrt{\frac{k_B T}{2\pi m}}} = \frac{N_s}{3.84 \times 10^{20} \text{ m}^{-2} \text{ s}^{-1} \text{ Pa}^{-1} P} \quad (2.1)$$

where P is pressure in Pa, and N_s is the number of particles per square meter that comprise the monolayer. At a reasonable base pressure of 1×10^{-6} Torr, and using a reasonable estimation of $N_s = 1 \times 10^{19} / \text{m}^2$ [3], this equation predicts the formation of a monolayer of impurities every 3.3 s. Though not all impinging particles adhere to the surface, this underestimation still provides a useful comparison metric with the chosen deposition rate.

Attaining sufficiently low pressures is technically challenging, as no single pump design can work effectively from atmospheric pressures down to a system base pressure of 10^{-6} Torr. Rather, a mechanical roughing pump generally lowers chamber pressure to a crossover point, where an ultra-high-vacuum pump takes over. I used a chamber equipped with a cryogenic pump, which relies on a liquid-helium cooled “finger” of high surface area that freezes impinging molecules, trapping gases of the chamber [1, 4].

Cryogenic pumps establish high vacuum by trapping residual gasses.

2.1.2 Electron beam evaporation

Having attained sufficiently low pressure, there are several methods of heating the source material to the point of vaporization. The oldest and simplest form of vacuum evaporation dates back to Faraday’s 1857 work, in which current was passed through metals to the point of sublimation [5]. Modern variations of this technique continuously heat a tungsten filament or boat, coated or filled with the deposition material. Such techniques are naturally restricted to temperatures below the melting point of the boat or filament [1].

Electron beam evaporation is a more efficient approach that pulls a beam of electrons from a thermionic emitter—usually a heated tungsten filament—and accelerates it with high DC voltage into a source material stored in a water-cooled crucible [1–3]. Heating emerges from simple transfer of the electrons’ kinetic energy. This technique has the advantage of working with nearly any source type, including refractory metals, regardless of whether the material melts or sublimates. In some cases, it is also possible to tightly focus the beam in the middle of the source, leaving the surrounding material unmelted—this has the added benefit of eliminating potential contamination from the crucible liner itself.

Electron beams can evaporate a wide variety of source materials.

Modern electron-beam evaporators use a stationary magnetic field to curl the electron beam by 270° , allowing it to strike material in the crucible without exposing the filament to the resultant vapour and decreasing its useful lifetime. Accelerating voltages typically range from 4–20 kV, and the beam current is generally a function of material and desired deposition rate. As most emitters are operated in saturation, the beam current is affected only by the filament current, which also controls the temperature of the emitter itself [1, 3].

During the deposition of compounds, molecules are often broken apart by the high energies of the electron beam, and components have varying evaporation rates. This often generates a film of different composition than the source [3]. In the case of the evaporation of metal oxides, oxygen is often inserted to counteract the effects of dissociation during vaporization.

Oxide evaporation often produces sub-stoichiometric films.

To ensure a stable evaporation, many materials require *conditioning*: allowing the source to evaporate for an extended period prior to exposure of the substrate. In melting materials, this allows the entire source to become molten and reduces source material surface contamination, minimizing the alteration of film composition [6].

2.1.3 Adatoms and nucleation

If not reflected back into the vacuum, evaporated atoms striking the substrate loosely associate with it in a processes known as *physisorption*. These absorbed particles, called *adatoms*, diffuse across the substrate by hopping from lattice site to lattice site. Diffusion is largely unaffected by the particles' incoming velocities, as energy released during condensation onto the surface usually dwarfs incoming kinetic energy [7]. Adatoms are eventually consumed through [8, 9]:

1. CLUSTERING with another adatom, forming a diatomic nucleus.
2. JOINING a larger, existing adatom cluster.
3. BINDING to substrate defects, such as a step between two crystal planes.
4. RE-EVAPORATING into the vacuum, especially common at higher temperatures.

Clusters begin to grow irreversibly upon reaching critical size.

Clustering is reversible. Smaller clusters are less stable, and result in more adatoms detaching from cluster edges [8]. There is a critical size at which detachment becomes energetically unfavourable, depending on the material and temperature—at low temperatures, the critical size may be as small as a single adatom. Critical clusters begin to grow—“ripen”—as adatoms diffuse away from the unstable smaller clusters in a process known as Ostwald ripening[10].

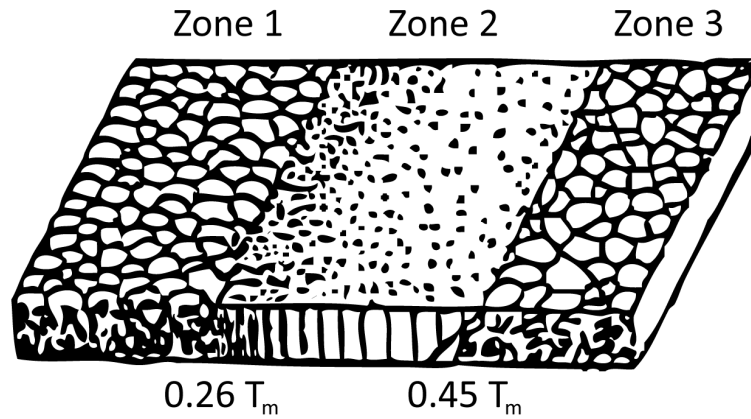


Figure 2.1: Movchan and Demchishin's structure zone model showing three distinct morphological zones in a thin film as temperature increases from left to right [12]. The transition temperatures are expressed as fractions of the material's melting point, and are given here for oxides [13]. Increasing temperature increases adatom diffusion, creating void-separated columns (Zone 1), densely-packed columns (Zone 2), and finally joined crystallites (Zone 3). Adapted from [12].

The evolution and joining of these clusters depend on the relative attraction of adatoms to the film and to each other, falling into one of three categories [9, 11]:

- A. FRANK-VAN DER MERWE GROWTH, characterized by high diffusion, sees monolayer clusters joining to cover the entire surface. This allows layer-by-layer epitaxial growth.
- B. VOLMER-WEBER GROWTH involves the formation of isolated clusters, leading to rough surfaces growing from independent nuclei.
- C. STRANSKI-KRASTINOV GROWTH is a hybrid of the two, with three-dimensional clusters growing on monolayers of perfect coverage.

Volmer-Weber growth produces rough surfaces from isolated clusters.

Without substrate heating and careful matching of the inter-atomic lattice spacing in the substrate and film, Volmer-Weber growth often dominates [10].

As the film continues to grow, internal diffusion joins surface diffusion in shaping morphology. Substrate temperature is a crucial factor, as demonstrated in the oft-cited Movchan and Demchishin structure zone model of Figure 2.1. High temperatures permit bulk diffusion and recrystallization during film growth, producing a mosaic of interconnected crystal grains (Zone 3). Decreased temperature reduces the amount of bulk diffusion, creating a densely packed array of columns with no separating voids (Zone 2). Lowering temperature

High temperatures increase diffusion, producing smoother films.

even further reduces adatom mobility, producing independent, broad-topped columns that grow from individual nuclei, separated by voids [9, 13]. These voids are created through *atomic shadowing*: protruding columns shelter the film underneath from receiving flux.

2.2 GLANCING ANGLE DEPOSITION

Atomic shadowing in collimated flux is the basis of the GLAD technique: highly oblique flux maximizes the shadowing effect, facilitating the creation of carefully sculpted nanostructure arrays. This section begins with a brief history of the method and an overview of its principles of operation, followed by a sampling of the nanostructures GLAD can produce. This provides a framework for the discussion of column broadening to follow.

2.2.1 *The development of the GLAD Technique*

As far back as 1886, researchers have noticed an unexpected change in the properties of thin films when deposition flux hits surfaces at angles far from normal¹ [16–18]. These metal films exhibited anisotropy, with properties like resistance varying with the direction of measurement along the film surface. Film morphology was the suspected cause, but the underlying mechanism was not explained until the 1950 work of König and Holder [19], who first introduced the concept of self shadowing. At oblique angles, as films nucleate and begin to grow, nuclei shadow the substrate behind them from incoming flux. Diagrammed in Figure 2.2, this shadowing causes preferential growth of the nuclei, which begin to form nano-scale columns that incline towards the source of vapour. Anisotropic properties thus reflected the anisotropy of the film itself.

Deposition at oblique angles promotes shadowing, changing film properties.

In 1959, Young and Kowal took exploitation of these anisotropies a step further, rotating the substrate during deposition to produce what they described as a “helically symmetric arrangement of crystallites, crystal growth, or voids” that could rotate polarized light [21]. Seven years later, Nieuwenhuizen and Haanstra [22] used electron microscopy to confirm the existence of columnar microstructures—alongside the columns produced on a stationary substrate, they produced “chevron” nanostructures by rotating their substrate between depositions, causing column tilt direction to reverse midway up the film.

Substrate rotation determines nanostructure shape.

Though interest continued in obliquely deposited films, particularly in the theory underlying their growth and their optical properties [23–25], the extraordinary control embodied in the GLAD technique grew out of 1995 work by Robbie *et al.* [26–28]. Depositions at

¹ Early literature on oblique-incidence is almost exclusively in German; I rely here on summaries provided in Ref. [9, 14, 15].

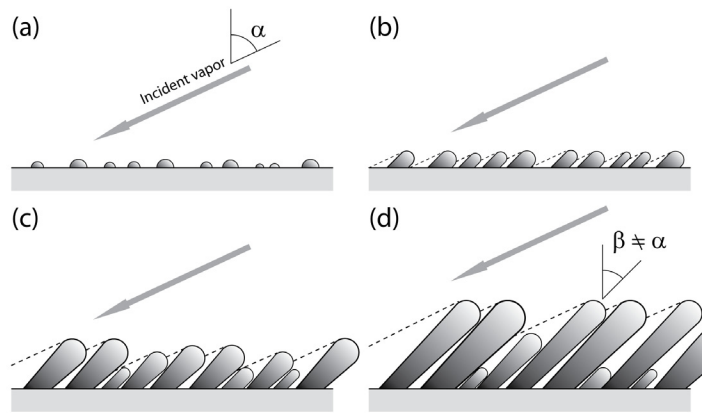


Figure 2.2: Diagram of the shadowing process at the heart of glancing angle deposition. Nuclei (a) that form in the early stages of growth shadow the regions behind them from the incoming flux, causing preferential growth into columns (b). As these grow, the shadowing process can starve slower-growing columns from flux entirely, causing column extinction (c). Columns bend toward the flux (d), but the angle of inclination β is less than the angle of incoming flux, α . Figure reproduced with permission from [20].

higher angles—generally 80° and greater—produced increased nano-column separation and focused attention on the construction of “designer” nanostructures through computerized growth control. Ensuing work has produced steady enhancement in the variety and reproducibility of GLAD films [9, 29], showcased in the arbitrary morphology of Figure 2.3. The diverse applications of GLAD films include surface-enhanced Raman spectroscopy, capacitive gas sensors, mechanical resonators, catalytic structures, magnetic data storage, and organic photovoltaics, in a list that is continually growing [20].

GLAD is an ever-expanding field of research.

2.2.2 GLAD growth basics

As column formation relies upon the shadowing principle, GLAD films generally emerge from Volmer-Weber growth and nucleation, remaining in Zone 1 of Figure 2.1. One reported exception is the organic Alq_3 , which wets the substrate completely before forming shadow-casting self-ordered droplets [31, 32]. In all cases, a well-defined shadow requires highly collimated flux impinging on the substrate with a low angular distribution. This is accomplished in an evaporation system by increasing the source-substrate distance and minimizing the ambient pressure. With a ~ 45 cm source-substrate distance, pressures should generally fall below $\sim 1 \times 10^{-3}$ Torr [20]; further pressure reductions improve shadowed structure quality as well as incurring the purity improvements discussed in Section 2.1.1.

GLAD shadowing requires highly collimated flux.

Sculpting the resulting nanostructures requires precise substrate control. Outlined in Figure 2.4, GLAD literature generally designates

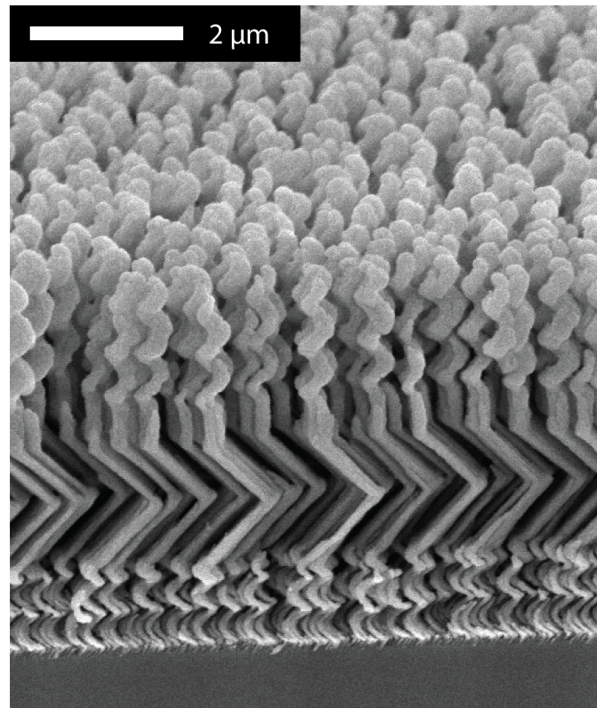


Figure 2.3: Film highlighting the breadth of control GLAD allows over nanostructure morphology. The film bottom has three turns of a right-handed TiO_2 helix, grown at $450\ \text{nm}$, followed by a SiO_2 zig-zag, a section of SiO_2 vertical post, and finally a left-handed SiO_2 helix. Figure taken with permission from [30].

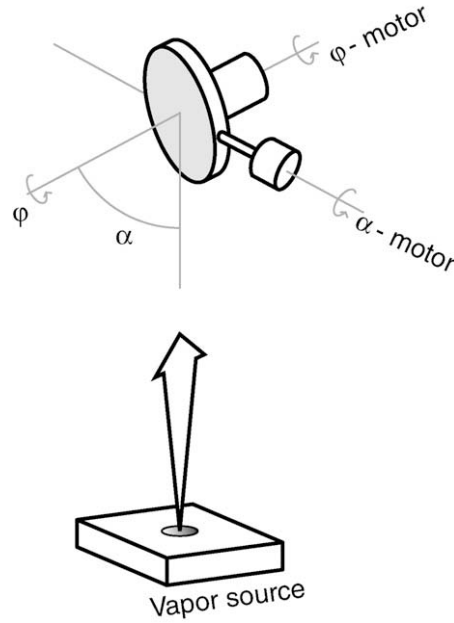


Figure 2.4: Diagram of the standard GLAD apparatus. Collimated flux travels from the vapour source to the substrate, forming an angle α with the substrate normal. Increasing α increases the influence of shadowing, resulting in a sparser film. Substrate rotation is measured by the angle ϕ , which permits the nanostructure sculpturing described here. Figure reproduced with permission from [33].

α as the angle between incoming flux and the substrate normal, while ϕ indicates substrate rotation. Bringing α closer to 90° makes shadowing more dramatic, resulting in sparser films with higher inter-column separation. Changing ϕ changes the direction of incident flux on the growing nanocolumns. The tendency of GLAD columns to tilt towards incoming flux thus allows ϕ to dictate the lateral component of growth, enabling the diverse collection of GLAD architectures reported in literature.

α is the angle between flux and the substrate normal; ϕ describes substrate rotation.

2.2.3 Basic GLAD structures

This section provides a sampling of GLAD morphologies particularly relevant to this thesis, but only scratches the surface of existing GLAD literature. A recent book chapter [20] and literature review [9] provide a much more thorough overview of GLAD theory, techniques, and application, and I encourage the interested reader to consult both.

Oblique angle deposition (slanted posts)

Oblique angle deposition, shown in Figure 2.5a, can be seen as the simplest form of glancing angle deposition: the substrate is not rotated, and seeds simply grow into columns, slanted toward the in-

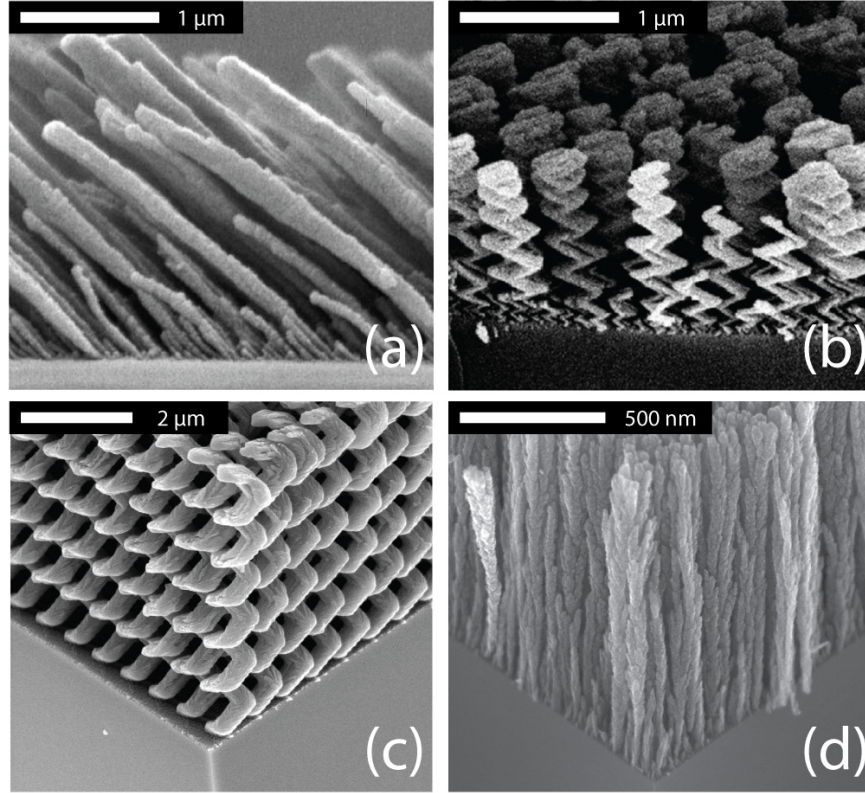


Figure 2.5: Sampling of the variety of structures glancing angle deposition can produce. A stationary substrate produces slanted posts, which broaden as they grow (a). Repeated rotation of ϕ by 180° produces zig-zag or chevron architectures (b). Rotations of 90° creates a square helix, with continuous rotation producing spiral helices (c). Under more rapid rotations, these spiral helices degenerate into vertical posts, like these TiO_2 posts produced for this thesis (d). Figures reproduced with permission from [34] (a) and [20] (b-c).

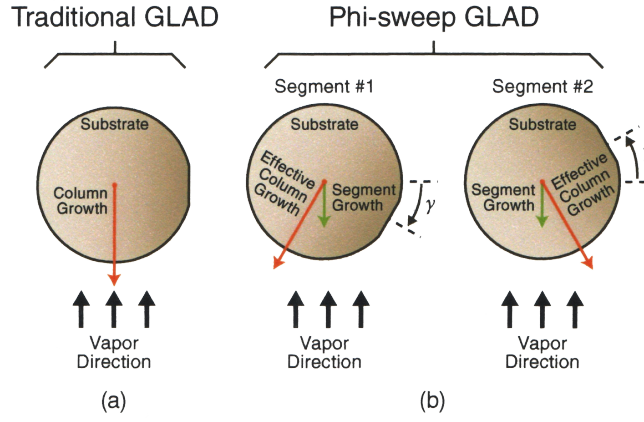


Figure 2.6: Substrate motion in the ϕ -sweep technique. Regular oblique deposition sees columns grow towards vapour flux on a stationary substrate (a). The ϕ -sweep process repeatedly alternates between two growth positions (b), separated by an angle of 2γ . The direction of effective column growth is midway between the two segment growth directions. Figure reproduced from [35] and [36].

coming flux at an angle (β). This angle is approximated by Tait *et al.* as

$$\beta = \alpha - \arcsin \frac{1 - \cos \alpha}{2} \quad (2.2)$$

where α assumes its usual definition as the angle between incoming flux and the substrate normal [25]. Material selection, deposition temperature, and chamber pressure can all cause deviations from this theoretical value [20]. Finally, as atomic shadowing only limits column growth in one direction, these columns tend to broaden perpendicular to the flux [34].

Oblique angle deposition holds ϕ constant.

PhiSweep

The broadening of slanted posts is often undesirable from an application standpoint, and the PhiSweep technique outlined in Figure 2.6 was developed to minimize it. The method relies on the periodic growth of segments in two different directions. The substrate is held in place for growth of an initial segment, quickly rotated² by 2γ , held for growth of a second segment, then rotated back. Repeating this procedure continually interrupts the broadening process, as shown in Figure 2.7, forming columns of roughly consistent diameter that point midway between the growth directions of the sub-segments [34]. The angle of these columns with the substrate normal will be less than that predicted by Equation 2.2, and can be controlled through selection of appropriate γ values.

PhiSweep minimizes broadening in slanted posts.

² Note that some published works define γ as twice the value given here, describing the complete rotation by γ' rather than 2γ [20].

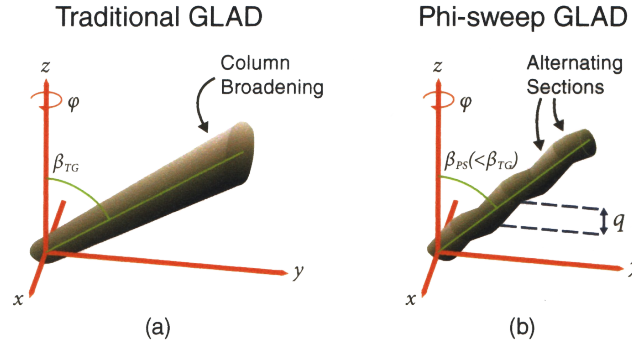


Figure 2.7: The alternating hold locations of the ϕ -sweep technique lead to the creation of numerous sub-segments, continually “resetting” the broadening process and maintaining uniform column diameter. Note that the angle of PhiSweep column inclination β_{PS} is less than that of the obliquely deposited column, β_{TG} . Figure reproduced from [35] and [36].

Chevrons and helices

Changes in ϕ change the lateral direction of column growth and can form multiple joined segments, with the same β slant, that point in different directions. Rapid 180° changes in ϕ produce the zig-zags shown in Figure 2.5b, while repeated 90° rotations grow the square spirals demonstrated in Figure 2.5c. Continuous, slow rotation sees these degenerate into helices as the growth direction follows an ever-changing flux direction.

Rotation rate determines helix tightness. Literature often describes rotation in terms of pitch, which is defined to be the thickness of film grown in a single 360° rotation of ϕ :

$$\text{pitch} = \frac{\delta h}{1 \text{ rotation}} = \frac{\delta h}{\frac{\delta \phi}{360^\circ}} \quad (2.3)$$

where h is the film height. For example, a 1500 nm film grown at 100 nm pitch would see 15 complete substrate rotations in the course of its deposition, yielding a helix with fifteen turns along its length.

Vertical posts

Increasing rotation rate—or decreasing pitch—during the deposition of helical films tightens their spirals, eventually collapsing them into dense screws with solid cores. Further increase approximates uniform flux from all azimuthal angles. This causes the screws to degenerate further into vertical nanocolumns, also referred to as vertical posts, rods, and pillars. Adatom mobility also plays a role in the transition from helix to vertical post. Even without increasing pitch, Robbie *et al.* and others observed helical growth transition into vertical post growth with rising substrate temperatures[37, 38].

Vertical post morphologies are important in many applications.

Pictured in Figure 2.5d, these vertical post are of intense interest to the research community. Explored applications of such nanorods are as diverse as atomic force microscopy calibration films [39], gas sensors [40–42], catalyst supports [43], microbatteries [44, 45], solar-cell electrodes [46], field emitters [47], chromatography media [48, 49], thermal barriers [50], reflectors [51], and precursors to nanotube arrays [52].

2.3 GLAD GROWTH SCALING THEORY

In this thesis, I study this single GLAD structure—the vertical post—as it broadens during growth. To properly frame discussions of its broadening, I first examine general surface growth scaling theory, then its application to oblique angle deposition, and finally its extension to the case of substrate rotation. I then provide a brief survey of existing experimental work on vertical post broadening and the factors that control it, setting the stage for the research presented in later chapters.

2.3.1 *Fractal concepts in surface growth*

The expanding boundaries of a wildfire, the shape of a bacterial colony in a Petri dish, and the path of a particle in Brownian motion—all these seemingly unrelated phenomena share a basic property with the growing surface of a PVD film, in that they display fractal character³ [53]. This realization intensified development of the mathematics of rough surfaces, and growth scaling theory is now generally discussed in the language of fractals [54, 55].

Many seemingly unrelated phenomena have similar scaling properties.

The term “fractal” brings to mind Mandelbrot’s famous images, which display *self-similarity*: under magnification, small features within the image are indistinguishable from the original image itself [55]. Real surfaces are generally *statistical* fractals: though they do not appear identical, their statistical properties—roughness, for instance—remain constant at different magnifications. Coastlines are one such statistical fractal. Given two maps without scales, it can be impossible to determine which has the higher magnification without outside knowledge.

Statistical fractals retain statistical properties under magnification.

Growing surfaces, in contrast, are generally not self-similar but *self-affine*: while they do reproduce their statistical properties under magnification, they only do so if the axes are scaled by different amounts.

³ Section 2.3.1 and Section 2.3.2 draw heavily from Barabási and Stanley’s “Fractal Concepts in Surface Growth,” a seemingly ubiquitous resource in recent growth-scaling literature. I strongly recommended this reference as a broad and helpful overview of growth scaling [53]. Unless otherwise indicated, this is the assumed reference for the discussion within these subsections.

In general, the function $f(x)$ is self-affine if, when scaled by the factor b ,

$$f(x) = b^{-\beta} f(bx) \quad (2.4)$$

$$f(bx) = b^{\beta} f(x) \quad (2.5)$$

where β is an exponent particular to the function. The properties of such functions, such as the height difference $\Delta = f(x_0 + \delta) - f(x_0)$, scale according to a power law⁴ such that $\Delta \sim \delta^{\beta}$ [56, p.49]. Note that true self-similarity describes the special case of $\beta = 1$.

Self-affine surfaces retain properties when axes are scaled differently.

Though discussed above in terms of magnification, this self-affine scaling is not restricted to spatial variables [57]. In dynamic surface growth, for instance, properties also scale in terms of the deposition time, t .

Surface roughness is perhaps the simplest example. The interface width, defined as the root-mean-square variation in surface height, is generally referred to as the *perpendicular correlation length* ξ_{\perp} as it is measured perpendicular to the surface. This roughness scales with time as

ξ_{\perp} represents a surface's interface width, or "perpendicular correlation length."

$$\xi_{\perp} \sim t^{\beta} \quad (2.6)$$

during the early stages of growth. The correlation length generally reaches a saturation value, $\xi_{\perp \text{sat}}$, which scales as

$$\xi_{\perp \text{sat}} \sim L^{\alpha} \quad (2.7)$$

with the size, L , of the region considered [58, 59]. Surfaces also possess a *lateral* or *parallel correlation length* ξ_{\parallel} which describes the range over which local information can spread laterally along the surface, as described in Figure 2.8. Like the interface width, this also scales with time:

ξ_{\parallel} represents the parallel correlation length, measuring the lateral spread of information.

$$\xi_{\parallel} \sim t^{1/z} \quad (2.8)$$

As might be expected, saturation of the interface width ξ_{\perp} occurs when the parallel correlation length ξ_{\parallel} is equal to the system size L . Thus, these exponents are related as $z = \alpha/\beta$ [53].

2.3.2 Universality classes

The scaling exponents above—the growth exponent, β ; the roughness exponent⁵, α ; and the dynamic exponent, z —provide predictive in-

⁴ Note that this does not necessarily imply that Δ scales *linearly* with δ^{β} —just that the exponential term dominates over the regions examined. Reference [56] contains further discussion on this notation in the context of thermodynamic power laws.

⁵ This exponent is entirely distinct from the angle of GLAD flux with the substrate normal, which also uses the symbol α .



Figure 2.8: The lateral or parallel correlation length ξ_{\parallel} is an intrinsic property of a growing surface and describes how far height information can spread laterally. The above figure highlights this information spread: a ballistic deposition simulation is performed on a surface with one high protrusion (red). Columns of pixels near the image edges are unaffected, as they are farther than ξ_{\parallel} from the protrusion and thus cannot “know” of its existence. Columns within ξ_{\parallel} of the protrusion are shadowed. Figure reproduced with permission from [53].

sight into the systems they describe. Fortunately, many diverse phenomena demonstrate similar scaling properties, and fall into natural groupings—universality classes—whose members share these same three scaling exponents. Once derived in one member of the universality class, their values can be applied to all to produce broadly useful conclusions from the study of simple models.

Insights into surface growth, for example, can come from readily-simulated two-dimensional Monte-Carlo deposition models, described below and commonly used in growth scaling literature. Atoms are represented as single pixels within a small grid, dropped from the top of a randomly-selected column onto a flat row of pixels representing the substrate. Changing the rules of these simulations exposes different universality classes, and can assist in the discovery of a continuum growth equation associated with each. This section begins with the simplest heuristic model of deposition and works upwards in complexity, finally introducing the Kardar-Parisi-Zhang and Mullins-Herring equations thought relevant to GLAD growth.

Random deposition

As its name suggests, random deposition describes particles landing randomly on surface lattice sites, independent of the sites’ heights and surroundings. A column rising above its neighbours is just as

Many diverse phenomena fall into the same universality classes.

Universality classes can be explored with simple models.

likely to receive flux as is a depression. Once particles land, they freeze into place.

With a constant deposition rate, the average height of the film $\langle h(x, t) \rangle$ increases continuously at a constant rate, v :

$$\frac{\partial \langle h(x, t) \rangle}{\partial t} = v \quad (2.9)$$

Each lattice site will also have a noise component, given the stochastic nature of the deposition. If we express this noise at position x and time t with the uncorrelated Gaussian noise term $\eta(x, t)$, we can produce a continuum growth equation for growth at position x

$$\frac{\partial h(x, t)}{\partial t} = v + \eta(x, t) \quad (2.10)$$

$$h(x, t) = vt + \int_0^t \eta(x, t) dt \quad (2.11)$$

where the expectation value of noise, $\langle \eta(x, t) \rangle$, is zero. In this simplest case, scaling coefficients can be evaluated analytically. Returning to the example of interface width, for example, we can write

$$\xi_{\perp} = \sqrt{\langle (h - \langle h \rangle)^2 \rangle} \quad (2.12)$$

$$\xi_{\perp}^2 = \langle h^2 \rangle - \langle h \rangle^2 \quad (2.13)$$

$$\xi_{\perp}^2 = (v^2 t^2 + 2 \langle \eta(x, t)^2 \rangle t) - (v^2 t) \quad (2.14)$$

$$\xi_{\perp} \sim t^{1/2} \quad (2.15)$$

Random deposition sees no lateral spread of information, so $\xi_{\parallel} = 0$.

which yields the scaling exponent $\beta = 1/2$ in all dimensions.

Similarly simple derivations of scaling constants do not exist for most universality classes, especially in higher dimensions, and more sophisticated techniques are required.

Random deposition with relaxation

At non-zero temperatures, deposited particles diffuse to minimize surface energy. The above model can change to reflect short-scale relaxation by allowing deposited particles to move to lower neighbouring sites. Note that this does not account for the long-range surface diffusion that would be seen in high-temperature depositions.

To reflect this relaxation, we must add a term to Equation 2.10. The theoretical development of such equations is greatly aided by system symmetries. As the growth equation should be independent of where the origin $h = 0$ is set, for instance, it can include no terms with direct dependence on h rather than its derivatives.

Relaxation introduces lateral spread of information, and thus non-zero ξ_{\parallel} .

In this case, similar considerations allow us to add the Laplacian, $\psi \nabla^2 h$. This term makes intuitive sense: the Laplacian is negative in regions of downward curvature, and positive in regions of upward

curvature. Thus, this term will be negative on hilltops and positive in valleys. We now have a second universality class, defined by the Edwards-Wilkinson (EW) equation [60]

$$\frac{\partial h(x, t)}{\partial t} = v + \psi \nabla^2 h + \eta(x, t) \quad (2.16)$$

where ψ , referred to as the “surface tension,” describes the intensity of the smoothing effect of relaxation.

This model is still simple enough to allow analytic derivation of scaling exponents, which depend on the number of dimensions included in the model.

Ballistic deposition

Ballistic deposition simulation extends the Edwards-Wilkinson equation by considering deposition on the edges of existing features. In this model, falling particles also stick to particles in adjacent columns, generating the branching morphologies commonly seen in real evaporations.

Again, the growth equation must expand to account for this effect. In this case, we add the non-linear term $\frac{\lambda}{2} (\nabla h)^2$, which is again intuitive. Always positive, the term is zero in flat regions and becomes positive on steep slopes, where the effect is most relevant. Adding this term produces the well-known Kardar-Parisi-Zhang (KPZ) equation [61]

The KPZ equation governs a widely studied universality class that may apply to GLAD.

$$\frac{\partial h(\vec{x}, t)}{\partial t} = v + \psi \nabla^2 h + \frac{\lambda}{2} (\nabla h)^2 + \eta(\vec{x}, t) \quad (2.17)$$

where we use the vector \vec{x} to extend the equation into higher dimensions. The non-linearity added to the KPZ equation by the final term makes the derivation of its scaling exponents challenging, and requires a perturbative renormalization group approach [62, 63] to produce the values in Table 2.1. Fortunately, once derived, these three exponents can be applied to all systems of equal dimensionality that obey the KPZ equation.

Though we have introduced the universality class heuristically, the scaling exponents α , β , and z have been experimentally shown to apply to numerous real-world systems, including some real cases of ballistic deposition, the growth of some bacterial colonies [64, 65], and the movement of interfaces in some disordered media [53]. While the equation itself remains unchanged, the terms have different interpretations in different physical contexts.

Dominant diffusion

The final relevant universality class describes growth *dominated* by surface diffusion. Symmetry considerations, as well as heuristic argu-

Name	Eqn. #	Stochastic growth equation	Exponents		
			α	β	z
RD	(2.10)	$\frac{\partial h(x,t)}{\partial t} = v + \eta(x, t)$	-	1/3	-
EW	(2.16)	$\frac{\partial h(x,t)}{\partial t} = v + \psi \nabla^2 h + \eta(x, t)$	1/2	1/4	2
KPZ	(2.17)	$\frac{\partial h(\vec{x},t)}{\partial t} = v + \psi \nabla^2 h + \frac{\lambda}{2} (\nabla h)^2 + \eta(\vec{x}, t)$	1/2	1/3	3/2
MH	(2.18)	$\frac{\partial h(\vec{x},t)}{\partial t} = v - K \nabla^4 h + \eta(\vec{x}, t)$	3/2	3/8	4

Table 2.1: Summary of the universality classes described in this chapter. The Kardar-Parisi-Zhang (KPZ) and Mullins-Herring (MH) growth equations are thought relevant to GLAD growth. Exponents shown here are given for the (1+1)-dimensional case, and change with increasing dimensions. Note that the case of random deposition (Equation 2.10) sees completely independent columns, and thus there is no correlation length or lateral spread of information. As such, interface width never saturates, and the model has no roughness exponent α or dynamic exponent z . Taschuk *et al.* summarize literature measurements of GLAD interface width, which appears to increase consistent with the power laws predicted by the above [20]. Table data is taken from [53].

ments based on chemical potentials, point to $-K\nabla^4 h$ as the dominant term. This term is positive in concave regions, reflecting binding energies lowered by the presence of extra nearby neighbours. Overall, it tends to smooth out the surface. Combining this with stochastic noise and constant average growth, we produce the Mullins-Herring (MH) equation [65]

$$\frac{\partial h(\vec{x}, t)}{\partial t} = v - K \nabla^4 h + \eta(\vec{x}, t) \quad (2.18)$$

whose scaling exponents are summarized in Table 2.1. In this model we ignore the non-linear effects in the KPZ model as well as the effects of particle desorption, which would introduce a $\psi \nabla^2 h$ term like that in the EW equation [66]. The MH equation is applicable at high temperatures and in molecular beam epitaxy (MBE), where its approximations are reasonable.

Summary of universality classes

The above universality classes, summarized in Table 2.1, make testable predictions about scaling behaviour. Experiments can thus determine the breadth of their applicability. In some cases, universality class predictions will only hold over a certain range of parameters. In viscous fluid flow through porous media, for example, smaller pore sizes introduce error that cannot be appropriately described by an uncorrelated Gaussian error term $\eta(x, t)$. When pore sizes are increased above a certain crossover point, however, they cease to be the dominant source of error, and recorded α values drop from 0.81 to the KPZ

With sufficiently high diffusion, most terms in the KPZ equation are negligible.

Systems can cross from one universality class to another.

prediction of $1/2$ [67]. Such crossovers between classes are integral to the GLAD scaling predictions below, which describe GLAD surface growth as being bounded by the MH and KPZ equations in the cases of strong and negligible diffusion, respectively.

2.3.3 Applications to oblique angle deposition

GLAD relies heavily on shadowing. Tall columns will starve their neighbours of flux, a competitive growth process that causes the extinction of smaller columns. While such growth can be studied with the $(2+1)$ -dimensional KPZ equation⁶, flux directionality adds an asymmetry that produces parallel correlation lengths in both the direction of flux, $\xi_{\parallel x}$, and at right angles to the flux, $\xi_{\parallel y}$. While shadowing effects limit the growth of $\xi_{\parallel x}$, the $\xi_{\parallel y}$ correlation length grows unhindered, reflecting the column broadening discussed in the slanted posts of Section 2.2.3. These lengths will thus scale differently with time [54]. Using Equation 2.6, we can write

$$\xi_{\parallel x} \sim t^{\beta_x} \quad (2.19)$$

$$\xi_{\parallel y} \sim t^{\beta_y} \quad (2.20)$$

for the two parallel correlation lengths.

In 1990, Meakin and Krug presented a simplification that reduced the problem from a two-dimensional surface to the analysis of one-dimensional edges [54]. At any given time, most of each growing column is shadowed by the column's neighbours and is thus no longer involved in the film's growth scaling. From the perspective of the vapour flux, as shown in Figure 2.9, only unshadowed "active zones" are visible, separated by large steps at the column tops. The evolution of the edges between the tops can be described by the $(1+1)$ -dimensional KPZ equation. The parallel and perpendicular correlation lengths of these edges, ξ_{\perp}^* and ξ_{\parallel}^* , are equivalent to the $\xi_{\parallel x}$ and $\xi_{\parallel y}$ of the full two-dimensional case. Recalling the basic scaling relations of Equation 2.6 and 2.8, this simplification allows us to apply the one-dimensional KPZ exponents given in Table 2.1:

$$\xi_{\perp}^* \sim t^{\beta_{(1+1)D}} = t^{1/3} \quad (2.21)$$

$$\xi_{\parallel}^* \sim t^{1/z_{(1+1)D}} = t^{2/3} \quad (2.22)$$

implying $\beta_x = 1/3$ and $\beta_y = 2/3$ [54]. These results are supported with ballistic deposition simulations that neglect long-range diffusion and desorption. Under the assumption of constant growth rate, col-

Oblique angle flux produces two sets of correlation lengths.

As viewed by incoming flux, growth areas are separated by gradually changing ridges.

Film growth is described by these ridges, governed by the $(1+1)D$ KPZ equation.

⁶ The $(d+1)$ notation refers to an interface of d spatial dimensions moving along the extra dimension, time. Thus, a line in a two-dimensional plane would be referred to as $(1+1)$ -dimensional, and a surface in three-dimensional space would be $(2+1)$ -dimensional. I use " $(1+1)$ -dimensional" and "one-dimensional" interchangeably.

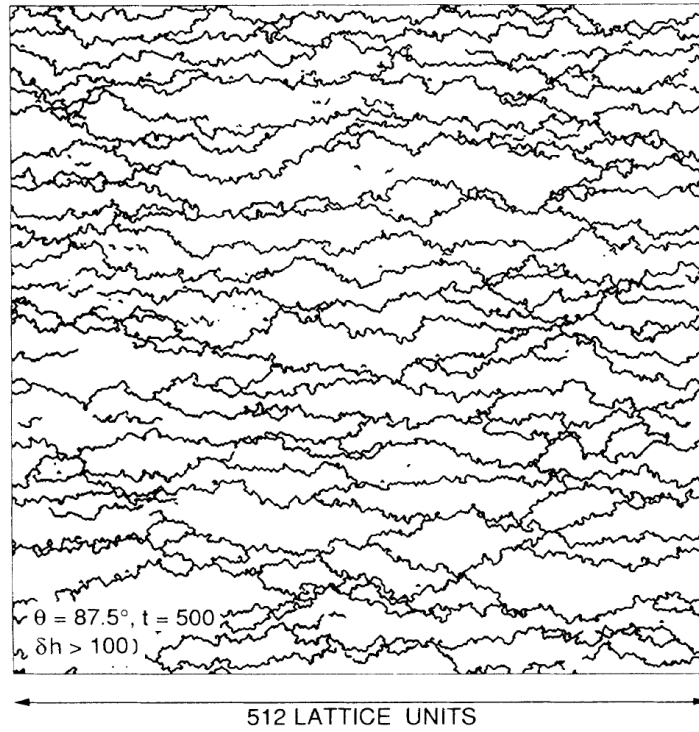


Figure 2.9: Simulation of $\alpha = 80^\circ$ oblique deposition performed by Meakin and Krug. The film is viewed from the perspective of the vapour flux—the substrate is rotated 87.5° into the page, allowing us to see what the incoming vapour “sees.” Only the unshadowed active zones are visible. Dark lines show the boundary between columns, and are governed by the $(1+1)$ -dimensional KPZ equation. The parallel correlation length ξ_{\parallel} is horizontal in the plane of the page, while the perpendicular length ξ_{\perp} is vertical. Figure reproduced with permission from [54].

umn height h scales identically with t , and we can rewrite these equations as⁷

$$\xi_{\perp}^* \sim h^{1/3} \quad (2.23)$$

$$\xi_{\parallel}^* \sim h^{2/3} \quad (2.24)$$

These equations are foundational to studies of GLAD broadening: they predict that column width and breadth scale according to a power law with film thickness. Further, in the case of minimal diffusion, they provide the relevant growth exponents.

⁷ Meakin and Krug use time $\xi_{\perp} \sim t^{\beta}$ and film height $\xi_{\perp} \sim h^{\beta}$ interchangeably in their work [54, 68], which is valid in the case of constant growth rate with constant flux.

2.3.4 Extension to vertical post morphology

Though GLAD's formalization increased interest in oblique-angle deposition theory, much early simulation work focused on the relative roles of surface diffusion and self-shadowing [7, 69, 70]. Unlike broadening oblique columns, vertical posts are generally well-separated. Examining the low-diffusion case governed by the KPZ equation, Meakin and Krug interpreted ξ_{\parallel}^* and ξ_{\perp}^* as approximations of the breadth and width of the average separated column. Not until 2003 was the above scaling theory first extended to the case of constant substrate rotation by Karabacak *et al.* [71]. Rapid substrate rotation averages these correlation lengths, producing an estimate of the average column area

$$A \sim \xi_{\parallel}^* \xi_{\perp}^* \quad (2.25)$$

Combining this with equations 2.23 and 2.24, mean column diameter can be expressed as

$$d \sim \sqrt{A} \quad (2.26)$$

$$\sim \sqrt{\xi_{\parallel}^* \xi_{\perp}^*} \quad (2.27)$$

$$\sim \sqrt{h^{\beta} h^{1/z}} \quad (2.28)$$

$$d \sim h^{\frac{\beta+1/z}{2}} \quad (2.29)$$

where h is column height d is column diameter. Karabacak *et al.* combined the exponents β and $1/z$ in Equation 2.29 to produce the relationship

$$d \sim h^p \quad (2.30)$$

which provides the basis for the power law commonly used to describe column scaling in the ensuing literature. Inserting one-dimensional KPZ values for β and $1/z$ into Equation 2.29 provides a theoretical value of

$$p_{\text{KPZ}} = \frac{1/3 + 2/3}{2} = 1/2 \quad (2.31)$$

in the limit of low-diffusion.

In the diffusion-dominated case, Karaback *et al.* propose a similar treatment of the Mullins-Herring equation. Inserting the one-dimensional MH exponents into Equation 2.29 yields

$$p_{\text{MH}} = \frac{3/8 + 1/4}{2} = 5/16 \quad (2.32)$$

in the limit of dominant diffusion. Thus, they predict the diameter of vertical posts to scale as h^p with p ranging from p_{MH} and p_{KPZ} . As I

Karabacak et al. suggested that rotation averages ξ_{\perp} and ξ_{\parallel} .

GLAD film broadening is described by a power law.

Karabacak et al. predict p between $5/16$ and $1/2$.

discuss below, early experimental evidence suggests that refinements to this model may be necessary.

Taschuk *et al.*, in their 2009 experimental study of this p exponent, proposed a variant of Equation 2.30 which captures material-to-material size variations in the parameter ω_0 [33]:

$$d = \omega_0 h^p \quad (2.33)$$

Height h is given as a unitless proportionality constant, with ω_0 is defined to be the column diameter at 1 μm thickness, measured in nm. I use this equation as the basis for scaling measurements throughout this thesis.

The power law used in this thesis.

2.3.5 Experimental studies of GLAD growth scaling

The above theoretical work provides an initial framework for vertical post morphology studies. Predicted limits on p invite experimental testing, and several groups have since reported experimental measurements of p in vertical post films [33, 71–77].

2.3.5.1 Early experimental literature

Karabacak *et al.* accompanied their initial theoretical work with experimental measurements on Si, Co, Cu, and W films grown to various heights [71, 72]. To extract p , they took width measurements at several different heights in the film, averaging several columns to produce each measurement. They then fit this data to Equation 2.33, extracting p values between 0.28 and 0.34.

GLAD broadening is most commonly measured from cross-sectional SEMs.

This method of measurement is the most popular in existing literature. Zhou and Gall use the same technique on seeded vertical posts to report $p = 0.5$ for Ta and $p = 0.6$ for Al, lying above the proposed KPZ limit. Cetinkaya studied the evolution of p in Si posts with changing flux angle, reporting a decrease in p from 0.59 to 0.32 as α increased from 75° to 89° [76]. Taschuk *et al.* studied the same angle dependence in three different oxides [33]. Though only one trend was statistically significant, they observed *increasing* p in the three materials as α increased from 75° to 87° .

Kaminska *et al.* took a different approach, studying Si vertical posts at $\alpha = 85^\circ$ [74]. Growing identical morphologies to a series of thicknesses, they analysed column diameter using particle detection algorithms on top-down scanning electron microscope (SEM) images at each thickness. Calculating a mean diameter allowed a fit to Equation 2.33, producing $p = 0.5$.

Instead of measuring average widths at different heights, Main *et al.* fit Equation 2.33 to the width profiles of individual columns, averaging these fitted values to produce a mean p between 0.32 and 0.39 [73]. Krause *et al.* studied individual $\alpha = 85^\circ$ TiO_2 columns using focused

Some groups have measured p for individual columns.

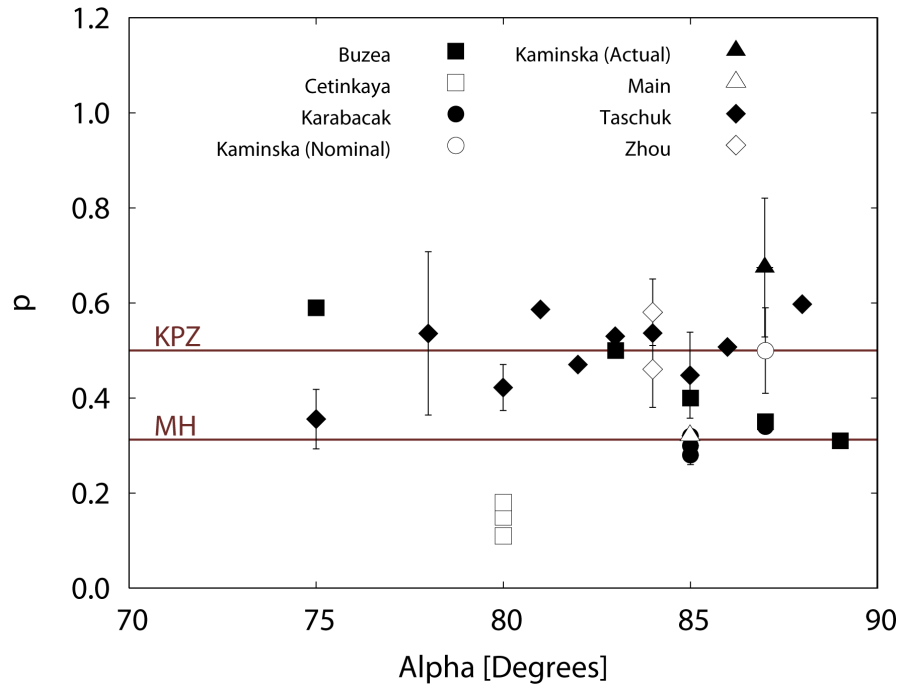


Figure 2.10: Partial summary of reported literature values for the exponent p , which describes column broadening. Existing data shows widespread scatter and no clear trends, highlighting the need for further investigation into GLAD scaling phenomena. The KPZ and MH lines are theoretical limits proposed on the broadening of these columns, discussed in Section 2.3.4; literature values lie outside both. Figure reproduced with permission from Taschuk *et al.* [33].

ion beam (FIB) tomography, which allowed full three-dimensional reconstructions of a handful of vertical posts. FIB analysis resulted in a mean of $p = 0.35$.

Power-law scaling has also been reported in organic vertical posts, with Cetinkaya *et al.* recording p between 0.11 and 0.18 in poly(p -xylylene) derivatives grown at $\alpha = 80^\circ$. The precise method of their measurements is not clear.

Taschuk *et al.* were the first to report a value for ω_0 , making comparison with previous literature difficult.

2.3.5.2 Scatter in reported p

In their 2009 oxide study, Taschuk *et al.* provided a review of existing literature p measurements, combining much of the work described above into a single plot [33]. Reproduced in Figure 2.10, this highlights the lack of consensus and repeatability in existing measurements and shows numerous values outside the proposed limits on p .

Taschuk *et al.* suggested substrate seeding as a potential confounding factor, as many groups deposited on a variety of pre-patterned

Literature p values are inconsistent.

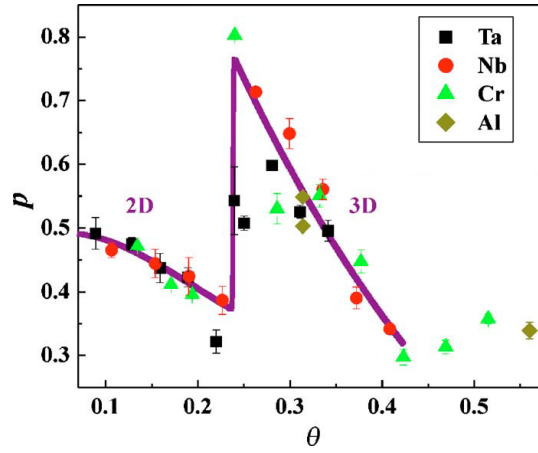


Figure 2.11: Anomalous scaling observed by Mukherjee *et al.*, where θ is the substrate temperature as a fraction of each material's melting point. Experimentally measured p values show a sharp increase at $\theta = 0.23$, which they attribute to a transition from 2D to 3D islanding as the adatom diffusion length becomes long enough to produce significant contact with terraces in the growing film. The purple curve is their theoretical prediction, based on the self-shadowing of islands on the surface of the columns. Figure reproduced with permission from [78].

substrates. As well, they note that some groups excluded widths of extinct columns from their data, hindering comparison from study to study. Lastly, they suggest film-to-film variation within statistically insignificant sample sizes may be in part responsible for observed noise [33].

In 2009, Mukherjee *et al.* revealed a further complicating factor in the effect of substrate temperature on column scaling in Ta, Nb, Cr, and Al [79, 80]. As expected from the increased contribution of surface diffusion, p decreased overall with increasing temperature. At a substrate temperature $T_s = 0.23T_m$, where T_m is the melting temperature of the material studied, they observed the unexpected scaling shown in Figure 2.11: p values rose sharply above the proposed KPZ limit.

Mukherjee *et al.* explain this trend as a transition from two- to three-dimensional islanding. With sufficiently high surface diffusion, adatoms will frequently encounter atomic terraces—steps from one monolayer to another. Falling down such terraces is energetically unfavourable, and adatoms are generally reflected. This asymmetry produces an adatom current that exacerbates growth of island height [78, 80]. While partially explaining unexpected results in measurements of low T_m materials, this does not address the question of repeatability or anomalous scaling in high- T_m films, leaving the scatter in these films an open question.

Prior to the development of the GLAD scaling power law, Dick *et al.* [81] performed an important qualitative study on the effect of

*Temperatures above
 $T_s = 0.23T_m$
produce
anomalously high p .*

pitch on vertical post morphology, measuring the effect of rotation speed $\left(\frac{d\phi}{dt}\right)$ on the growth rate of GLAD films. Increasing $\frac{d\phi}{dt}$ —that is, decreasing pitch—had the visible effect of reducing broadening in aluminum GLAD, which possesses both a low melting temperature and crystalline growth. The trend was less pronounced in less-crystalline bismuth, and was not detectable by eye in Si and SiO₂, both higher- T_m materials. Though deposition temperature was unchanged throughout, the authors theorized that slower rotation allowed atoms greater time to diffuse into preferred planes of crystal growth before being buried, thus enhancing broadening.

Despite clear qualitative results, the effect of pitch on p has not yet been quantitatively studied. Pitch may be a second major factor contributing to disparity in literature results, with some groups not reporting deposition rotation rates [33, 75, 77]. Further, the effect of pitch is of interest as a potential method for better-controlling film morphology.

This thesis aims to fill this gap in growth scaling literature. At the same time, I offer a new approach to broadening measurement that may contribute to improved reliability.

2.4 TITANIUM DIOXIDE

Though the measurement techniques employed in this thesis should be readily transferable to other materials, I focus on growth scaling phenomena in titanium dioxide (TiO₂). Colloquially known as titania, the oxide has a litany of modern applications both in bulk and on the nanoscale. This section briefly highlights some of these applications, titania's relevant chemical and physical properties, and a sampling of its existing presence in GLAD literature.

2.4.1 Applications

Titania's combination of properties and availability lend immense diversity to its uses in research and industry. Forming a bright white powder, titania is the world's most common inorganic pigment, and is found in products as diverse as paint, toothpaste, and skim milk, where it purportedly enhances palatability [82–84]. Titania nanoparticles strongly absorb UV light, and are thus the primary component of many commercial sunscreens [85]. In medicine, titanium implants are widely regarded for their strength and bio-compatibility: their native oxide surface is both resistant to corrosion and amenable to cellular adhesion [86, 87]. Nanostructured titania surfaces are consequently incorporated into cell-based assays and biosensors [88].

The photocatalytic properties of titania have been exploited in humidity sensing, air purification, anti-cancer therapies, steel corrosion prevention, and anti-microbial surfaces [41, 89–91]. Finally, titania

Pitch appears to influence broadening, but this has not been quantitatively studied.

All films in this thesis are made with TiO₂.

Titania has immense industrial and biomedical importance.

thin films have controllable, high indices of refraction, making them widespread in optical coatings [92, 93].

2.4.2 Chemical and physical properties

Though TiO_2 is the most common oxidation state, titanium also forms TiO , Ti_2O_3 , and more complex sub-stoichiometric compounds. Crystalline titania usually adopts one of three structures:

ANATASE (tetragonal) forms at low temperatures in some deposition systems and from annealing treatments of amorphous TiO_2 above $\sim 350^\circ\text{C}$ [94].

RUTILE (tetragonal) is the most thermodynamically stable form, and is thus formed in high-temperature depositions and through annealing treatments above $\sim 800^\circ\text{C}$ [94, 95].

BROOKITE (orthorhombic) is not found in evaporated films [96] and is of minimal technical importance [95].

The crystallinity of evaporated titania films depend on the chosen oxide source, the chamber oxygen concentrations, and substrate temperature [96]. With unheated substrates, the TiO_2 evaporations used in this thesis have been repeatedly shown in XRD analysis to produce amorphous films, both at normal incidence [97] and in glancing angle deposition [42, 94, 98]. With a melting point of 1840°C [99], entry into the $0.23T_m$ region of anomalous scaling identified by Mukherjee *et al.* requires a substrate temperature of $\sim 212^\circ\text{C}$ [80].

GLAD titania is amorphous.

When exposed to light wavelengths below $\sim 415\text{ nm}$, titania exhibits photocatalytic behaviour as the UV light produces free electrons and holes capable of oxidizing water [89]. This not only accounts for its antimicrobial properties but allows some control of surface properties. Sufficient UV illumination causes photocatalytic breakdown of hydrocarbons adsorbed onto the titania surface, resulting in a sudden increase in hydrophilicity that is exploited in some titania-based gas sensors [100].

UV treatment increases TiO_2 hydrophilicity.

2.4.3 Stoichiometry of evaporated titania

Evaporated thin films of titania are often grown from rutile titania chunks, though success has also been reported using less oxidized sources in the presence of oxygen gas. Rutile titania adopts a whitish hue, and blue coloration seen in evaporation sources is generally indicative of an oxygen deficiency in the source material [101]. In the absence of reactive oxygen, even a fully oxidized source of TiO_2 will dissociate during evaporation and produce a sub-stoichiometric oxide, TiO_{2-x} , which more accurately represents the films grown in

TiO_2 films in this thesis are likely sub-stoichiometric.

this thesis. For simplicity, I still refer to the oxide as TiO_2 throughout the text.

2.4.4 GLAD Titania

Titania GLAD films are investigated in a number of different applications, including:

HUMIDITY SENSING: A stable, hydrophilic oxide, TiO_2 is an excellent candidate for gas sensing. The high surface area of GLAD is leveraged to make ultrafast capacitive relative humidity sensors, with water vapor adsorbing onto nanocolumns to cause a measurable shift in permittivity [15, 42]. The photocatalytic properties of the film can be used to regenerate the sensor, improving sensor lifetimes [41, 102, 103].

GLAD titania has numerous potential applications.

ORGANIC PHOTOVOLTAICS: Intense interest in developing low-cost organic photovoltaics has prompted the use of nanostructured titania in a variety of solar cell architectures, exploiting both its surface chemistries and wide bandgap. Such applications generally require extremely high surface areas and a contiguous conductive path, making GLAD TiO_2 films a promising candidate that has been extensively investigated [104–107].

OPTICAL FILTERS: Seeded GLAD permits a high degree of morphological control over repeated arrays of nanostructures, prompting research into a variety of optical GLAD applications, including photonic crystals [108], rugate filters [109], and circular polarizers [110]. Again, titania's high refractive index and transparency in the visible regime make it a common material choice.

Even given this incomplete listing, it is not surprising that TiO_2 GLAD has been the subject of multiple morphological studies. These include the first use of krypton gas adsorption to study GLAD porosity [111], the first use of focused ion beam tomography to study GLAD broadening [77, 112], and the large-scale empirical study of the relationship between p and α described in Section 2.3.5 [33]. The material in this thesis builds particularly on the latter work, with a view to bettering our understanding and control of GLAD growth scaling, improving performance of future devices.

MATERIALS AND METHODS

Experimentally probing subtle growth scaling trends requires the deposition of numerous samples. This chapter describes the materials and methods used to create these samples, including the development of a multi-stage rotation apparatus that permits parallel deposition of samples at multiple pitches.

I also briefly cover initial sample characterization, including gross film morphology and thickness variation between depositions.

3.1 SAMPLE FABRICATION

3.1.1 Substrate preparation

I deposited films on substrates cleaved from 4" {100} *p*-doped Si wafers (University WAFER, Boston), which were stored in ambient conditions and thus coated in a thin layer of native oxide. I cleaned each substrate with the following:

1. AN ACETONE IMMERSION to remove organic contaminants. I immersed up to three quarter wafers in a 250 mL acetone-filled glass beaker, with an inverted, centrally placed 50 mL beaker keeping wafers upright and their polished faces oriented outwards, preventing damage. This beaker was then suspended on a styrofoam mount in the bath of a TruSonic 575 ultrasonic cleaner and sonicated for three minutes on the maximum power setting.
2. A RINSE IN ISOPROPANOL, in de-ionized water, and another in isopropanol to eliminate polar contaminants. Wafers were rinsed individually, held with tweezers.
3. PRESSURIZED NITROGEN to evaporate remaining isopropanol from the wafer surface.

All depositions occurred on clean Si wafers with a native oxide surface.

Double-sided polyimide adhesive tape (CAPLINQ Canada, Ottawa) fastened the cleaved substrates either to a 7" aluminium chuck or the rotation stage discussed in Section 3.2 below. Prior to insertion in the vacuum chamber, the entire chuck was cleaned again with a burst of ionized nitrogen.

3.1.2 Deposition

All depositions used an electron beam physical vapour deposition system (Kurt J. Lesker AXXIS) equipped with a custom substrate-motion controller, governing both the angle of the incident flux (α) and the chuck rotation (ϕ) as a function of the deposition rate measured by a calibrated quartz crystal microbalance (6 MHz, Al-coated, Maxtek – now Inficon). The controller accepted film parameters in a recipe file of (h, α , ϕ) triplets, where h is film height in nm and both α and ϕ are given in degrees. The following recipe, for instance:

```
0 81 0
1500 81 54000
```

produced a 1500 nm vertical post film of $\alpha = 81^\circ$ with a pitch of

$$1500 \text{ nm} \cdot \frac{360^\circ / \text{rot.}}{54000^\circ} = 10 \text{ nm} / \text{rot.} \quad (3.1)$$

Similar recipes were created for all film morphologies.

Porosity in GLAD films increases growth rate over comparable $\alpha = 0^\circ$ films. AXXIS software compensates for this with an experimentally-determined deposition ratio, dependent both on α and deposition material. The $\alpha = 81^\circ$ titania films used in this study were all produced with a ratio of 0.75, based on existing calibration studies¹. This was only approximately correct under the conditions employed, as film thicknesses—and thus film pitches—were repeatedly below nominal. As this effect was largely consistent from deposition to deposition, such differences did not affect the relationships investigated between the different films. Section 3.3.2 contains a more detailed discussion of thickness variation.

Rutile titanium dioxide chunks (99.9% purity, Cerac Inc. – now Materion Corp.) were placed in a copper crucible at a throw distance of 40 cm from the rotation chuck center and melted with a 6.5 kV, 220 mA – 250 mA electron beam. To maintain flux uniformity, I subjected the melt to a lengthy conditioning process, initially stepping current up in 25 mA increments every five minutes until reaching the desired rate. To increase throughput in later depositions, the early stages of this process were abbreviated with 50 mA steps up to 150 mA, followed with 25 mA increments. In all cases, crucible contents were molten prior to deposition onset.

Melts were incompletely consumed, and the post-deposition titania remnant was reused alongside additional fresh pieces. While rutile chunks were white or blue in colour, the remnant appeared dark gray with high sheen, indicative of under-oxidation [101]. None of the depositions used additional reactive oxygen, and studied films were

The deposition controller dynamically adjusted for changing deposition rate.

Titania films used in this study are likely under-oxidized.

¹ This deposition ratio was previously determined by Dr. J. Steele, as part of a series of titania depositions.

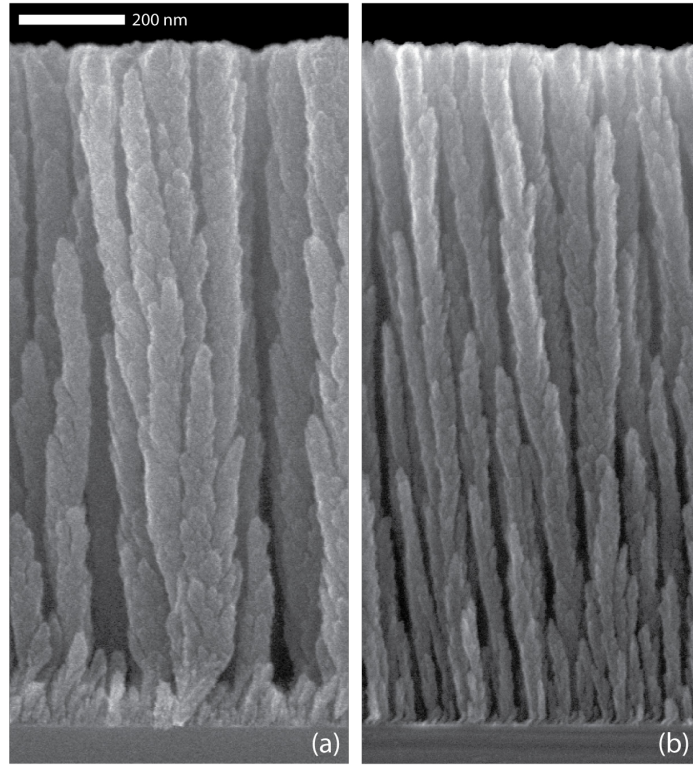


Figure 3.1: Images of TiO_2 $\alpha = 81^\circ$ films deposited at a rate of 28 \AA s^{-1} , first without shuttering (a) and then with carefully timed manual shuttering (b). By default, substrate control software does not rotate ϕ during initial α rotation, resulting in brief oblique-angle deposition. Though not obvious in low rate samples, and minimized with careful shuttering, such behaviour may affect initial film nucleation.

thus likely sub-stoichiometric (TiO_{2-x}). For simplicity, these films are still referred to as TiO_2 in this thesis.

All films were deposited at pressures below 700 \mu Pa ($5 \times 10^{-6} \text{ Torr}$), using base pressures below $\sim 100 \text{ \mu Pa}$ ($1 \times 10^{-6} \text{ Torr}$). All rates mentioned in this thesis reflect calibrated QCM output before application of the deposition ratio.

3.1.3 Near-substrate defects

High-rate depositions required an important adjustment. By default, AXXIS software holds α above 90° during conditioning, shielding the substrates from flux. When the deposition is started, α is rotated to the desired value, at which point ϕ rotation commences. The lag time prior to the onset of ϕ rotation appeared negligible at rates of 7 \AA s^{-1} , but films deposited at 14 \AA s^{-1} and 28 \AA s^{-1} demonstrated the significant defects shown in Figure 3.1. Shuttering the source until the onset of ϕ rotation is only approximately possible, as the software

governing the deposition will fail if rate drops to zero after the commencement of deposition. Though careful manual timing can reduce the impact of such defects, they are likely present to some degree in all of the films produced.

3.2 ROTATION STAGE

High-throughput study of growth scaling required faster sample fabrication and analysis. We accomplished this with a rotation stage geared to permit parallel deposition on samples rotating at different speeds². Similar stages have been described [81], but the spatial layout of our evaporation system necessitated a custom design.

3.2.1 Design considerations

A functional rotation stage requires shafts of differing rotation speeds that all see nearly identical flux from the deposition source, ensuring that no spatial factors confound trends produced by gearing.

To simplify the gearing, we placed sub-stages in a single line that lay 3.8 cm above the surface of the deposition system's chuck. This extra protrusion, necessary to fit gearing above the existing chuck mount, demanded deposition at a corrected angle α_{corr} . A throw distance of ~ 40 cm coupled with a ~ 3.8 cm protrusion produces the angular offset

$$\alpha_{\text{corr}} - \alpha = \arctan\left(\frac{3.9\text{cm}}{40 \pm 1\text{cm}}\right) = 5.4 \pm 0.1^\circ \quad (3.2)$$

which needs to be subtracted from the desired α to generate the appropriate recipe value. In our case of $\alpha = 81^\circ$, we thus utilized $\alpha_{\text{corr}} = 75.6^\circ$.

The line of sub-stages needed to be oriented to maximize flux uniformity. In the general case of electron beam evaporation, the amount of deposited mass (dM_s) per unit area of substrate (dA_s) is given as

$$\Phi = \frac{dM_s}{dA_s} = \frac{M_e(n+1)\cos^n\psi\cos(\alpha)}{2\pi|\vec{r}|^2} \quad (3.3)$$

where M_e is the total evaporated mass over a given time, \vec{r} is a vector from the source to the deposition location, and ψ is the angle between \vec{r} and the source normal [1]. In the case of electron beam evaporation, n is a constant that describes the directionality of the flux; Wakefield and Sit estimate this constant between 2 and 4 in work on a similar system [113], and it is approximated here as 3. Placing stages along

² Initial schematics of the rotation stage were drawn up by Dr. Michael Taschuk. The stage was built by personnel at the ECE Machine Shop, and I was responsible for installation, testing, and modification.

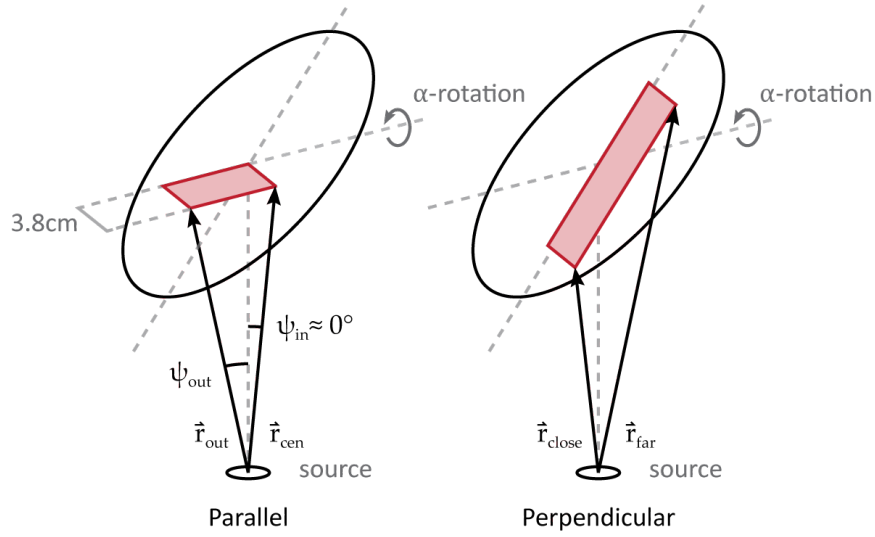


Figure 3.2: Schematic of the distances and angles required for the calculation of the maximum and minimum flux on the rotation stage, placed parallel and perpendicular to the axis of α rotation. Figure not to scale.

the axis of α rotation provides a nearly constant distance $|\vec{r}|$ from the source to each chuck, while placing them perpendicular to the axis minimizes variation in the angle ψ . Simple calculations based on the geometry shown in Figure 3.2 allowed comparison, considering both the change in \vec{r} from the central (\vec{r}_{cen}) to the outermost (\vec{r}_{out}) sub-stage and the changing angle ψ .

1. PARALLEL TO THE α AXIS, the Pythagorean theorem allows calculation of $|\vec{r}|$ based on the approximate throw distance $\vec{r}_{cen} = 35$ cm and 6.4 cm center-to-center distance between the two sub-stages. The angle of incoming flux at the outermost stage, ψ_{out} , is also calculable via basic trigonometry, yielding the ratio of flux at the outermost to the center sub-stage

$$\frac{\Phi_{out}}{\Phi_{cen}} = \frac{\frac{\cos^n \psi_{out}}{|\vec{r}_{out}|^2}}{\frac{\cos^n \psi_{in}}{|\vec{r}_{cen}|^2}} = \frac{\frac{\cos^3(9^\circ)}{(6.4\text{cm})^2 + (40\text{cm})^2}}{\frac{\cos^n 0^\circ}{40\text{cm}^2}} = 0.95 \quad (3.4)$$

indicating a 5% change in flux density.

2. PERPENDICULAR TO THE α AXIS, we can similarly calculate the flux ratio based on the assumption of nearly perpendicular deposition, such that $\psi_{out} \approx 0^\circ$. In this case, however, the greatest difference in received flux occurs between the stages at opposite edges of the chuck, rather than between the centermost and outermost stages. The approximate flux ratio is given as:

$$\frac{\Phi_{far}}{\Phi_{close}} = \frac{|\vec{r}_{close}|^2}{|\vec{r}_{far}|^2} = \frac{(40\text{cm} - 3.2\text{cm})^2}{(40\text{cm} + 3.2\text{cm})^2} = 0.74 \quad (3.5)$$

Sub-stage flux uniformity was comparable to across-substrate uniformity in regular depositions.



Figure 3.3: Photo of the rotation stage assembly. Each stage was capable of supporting an $\sim 1'' \times 1''$ substrate. The stage screwed down onto aluminium standoffs, with the root shaft (left side) screwing directly onto the system's central shaft. The rotation stage had gearing ratios of: 1:1 (blue), 3:1 (purple), 6:1 (yellow), and 12:1 (green). The stage immediately lent itself to the production of vertical post morphologies at multiple pitches, and, with the considerations outlined in Figure 3.4, ϕ -sweep films.

which indicates an unacceptable difference in flux between the two sub-stages.

These approximations indicate that conservation in throw distance is most important, and that placing the sub-stages in the axis of α -rotation yields at most 5% height variation. These results are in close agreement with Wakefield's studies on slanted post depositions [113], which examine the variation of film properties across a > 4 cm chuck.

The rotation stage used in the final design, pictured in Figure 3.3, consisted of a sub-stage spinning with the root shaft and sub-stages rotating 3, 6, and 12 times faster, permitting simultaneous deposition of vertical posts at four different pitches. Though more shafts would be desirable, as in a previously described apparatus with six sub-stages [81], existing deposition system gearing in the α -rotation axis prevents the placement of sub-stages on both sides of the central driveshaft.

3.2.2 *Phi-sweep considerations*

I performed preliminary work into the extension of this rotation stage into the parallel deposition of multiple ϕ -sweep films of different γ values, as defined in Section 2.2.3. The ϕ -sweep process rotates the substrate back and forth between two growth positions, offset by an

angle γ on either side of the effective growth direction. An ideal initial growth scaling study would produce samples evenly spanning the allowable space from $\gamma = 0^\circ$ to 90° , which would see samples with $\gamma = 18^\circ, 36^\circ, 54^\circ$, and 72° .

The task became to determine the angle of rotation in the original driveshaft that yielded the closest approximation of the desired set of effective γ rotations in the four separate stages. In the ϕ -sweep process, the transition time from one hold location to another is a fraction of a second, which can be ignored at typical TiO_2 deposition rates of $\sim 0.5 \text{ nms}^{-1}$. Thus, rotation through $\gamma=95^\circ$ is functionally the same as a rotation through 85° . More generally, $\gamma_{\text{effective}}$ is given as

$$\gamma_{\text{effective}} = \left| \left(\frac{\gamma_{\text{stage}}}{90^\circ} \bmod 2 \right) - (\gamma_{\text{stage}} \bmod 90^\circ) \right| \quad (3.6)$$

where \bmod refers to the *modulo* operator, and γ_{stage} is the actual rotation seen at a particular stage. This formula provides $\gamma_{\text{effective}}$ for any given rotation of the root shaft, plotted in Figure 3.4 for all of the four stages in the final design. From this plot, one can empirically locate the root shaft rotation that provides the desired set of $\gamma_{\text{effective}}$ values. In the simple case of wanting to evenly space $\gamma_{\text{effective}}$ across the allowable range of $0^\circ - 90^\circ$, this optimal value was calculated as a root rotation of 18° , providing the ideal $\gamma_{\text{effective}}$ values of $18^\circ, 36^\circ, 54^\circ$, and 72° .

Unlike in the simple case of vertical post deposition, traditional ϕ -sweep deposition sees the stage rotation direction change repeatedly throughout the deposition. With the addition of the rotation stage, such directional changes are infeasible, as the propagation of backlash to the final gear in the drive train may introduce an unacceptable degree of error in ϕ . This can be mitigated by again turning to Equation 3.6—rather than rotate back to the first hold position, the root shaft can simply complete the arc in the same direction as the original motion, thus eliminating directional changes over the course of film growth. This slightly increases transfer times between hold positions, but is likely not sufficient to affect film morphology.

Extensions of this method could provide similar ideal values for depositions spanning an arbitrary γ range, incorporating multiple depositions to decrease the γ spacing from one film to another; such work could extend the high-throughput research techniques described in this thesis to the ϕ -sweep morphology.

The rotation stage could also be used to deposit multiple ϕ -sweep films with different γ values.

3.3 INITIAL FILM CHARACTERIZATION

Shown in Figure 3.5 are typical TiO_2 $\alpha = 81^\circ$ vertical posts, deposited at 1 nm pitch. Though not resolved in the majority of the SEMs taken in this study, high-resolution shots reveal a rough, cauliflower-like surface across the entirety of the vertical post. The posts themselves

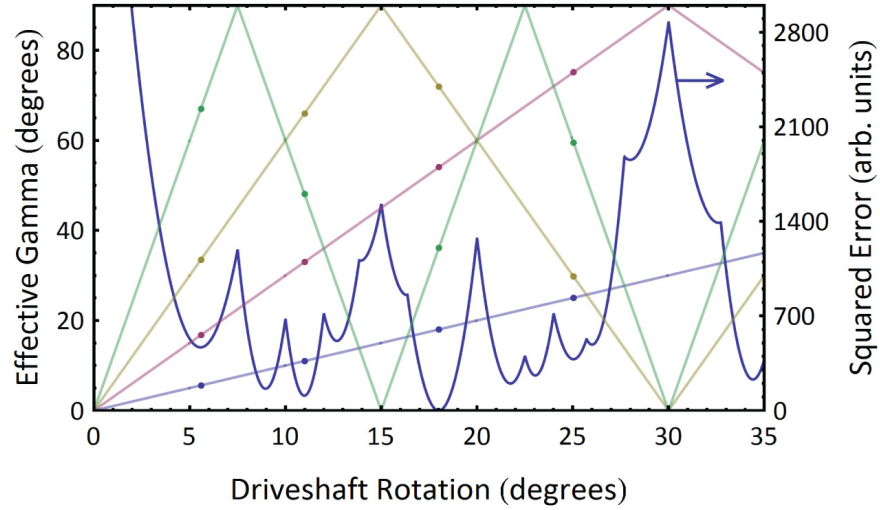


Figure 3.4: The rotation stage calibration plot for ϕ -sweep GLAD, with the goal of having the four stages evenly span the space of γ from 0° to 90° . The bottom axis gives the rotation in degrees of the central shaft, to which the four geared stages are attached. The four coloured lines show the effective rotations (γ) seen at each of the stages, with gearing ratios of: 1:1 (blue), 3:1 (purple), 6:1 (yellow), and 12:1 (green). Note that a γ value of 95° is functionally the same as a γ of 85° . The blue curve represents the squared error associated with each angle, calculated by squaring the difference between the “ideally spaced” γ values (18° , 36° , 54° , and 72°) and closest effective γ seen on the four stages. The plotted value is the sum of all four errors. Four minima were examined as potential candidates, with the effective γ values seen on the four stages marked with dots. A driveshaft rotation of 18° precisely produces the ideal γ spacing.

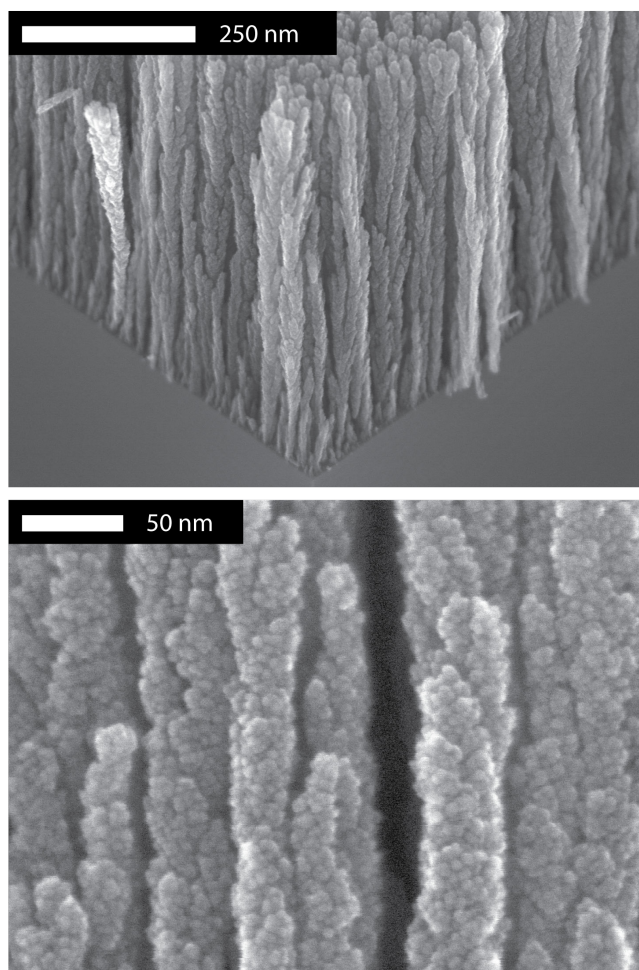


Figure 3.5: An oblique-angle SEM (upper image) of a 1 nm pitch TiO₂ $\alpha = 81^\circ$ GLAD film, providing a visual overview of the typical TiO₂ vertical post nanostructure. Note the highly branching nature of the film, as well as the presence of tapering extinct posts near the substrate. A high-resolution SEM (lower image) of a different 1 nm pitch sample reveals a complex, cauliflower-like surface that is not resolved in the majority of the lower-resolution images taken in the course of this study. This rough surface suggests that surface diffusion plays a more limited role in TiO₂ deposition than in other common GLAD materials.

are heavily branched, and throughout the film are examples of extinct columns out-competed during deposition. Branch bottoms, extinct columns, and surviving columns are difficult to distinguish morphologically. Though clearly evident in all of the films, it is extremely difficult to conclusively rank the degree of broadening among different samples due to the complex morphology of the film and the small magnitude of any existing differences.

Although these films were not subjected to XRD to determine their crystallinity, multiple authors depositing under similar conditions have indicated that titania nanocolumns are amorphous unless annealed [15, 83, 108].

TiO₂ films branch heavily and broaden as they grow.

3.3.1 Effect of pitch on gross nanostructure morphology

As a primary focus of the investigation was the analysis of the effect of pitch on growth scaling phenomena, I produced $\alpha = 81^\circ$ TiO₂ films at numerous pitches. Most obviously, pitch governs whether a film adopts vertical post or helical morphology, and this dataset spanned pitches producing both.

Early work indicated that nominal pitches below 10 nm produced vertical posts, while pitches at and above 100 nm produced films with visible helical morphology. To more precisely determine the transition point, I designed a film morphology with graduated pitch, writing a recipe file that changed deposition pitch in steps while the film was being deposited. Pitch thus became a function of height above the substrate.

During the deposition of the film in Figure 3.6a, for instance, I decreased pitch from 100 nm to 0.5 nm according to the equation:

$$\text{pitch} = 10^{\log 100 - (\log 100 - \log 0.5) \cdot \frac{h}{1500\text{nm}}} \text{nm} \quad (3.7)$$

$$= 100\text{nm} \cdot 10^{-\frac{\log 100 - \log 0.5}{1500\text{nm}} h} \quad (3.8)$$

where h is the film height in nm, rounded down to the nearest 10 nm—in effect, the logarithm of pitch is scaled linearly across the thickness of the film. The recipe file used in this case was thus

```
0 81 0
10 81 36
20 81 73
30 81 112
40 81 152
50 81 193
60 81 236
70 81 281
etc.
```

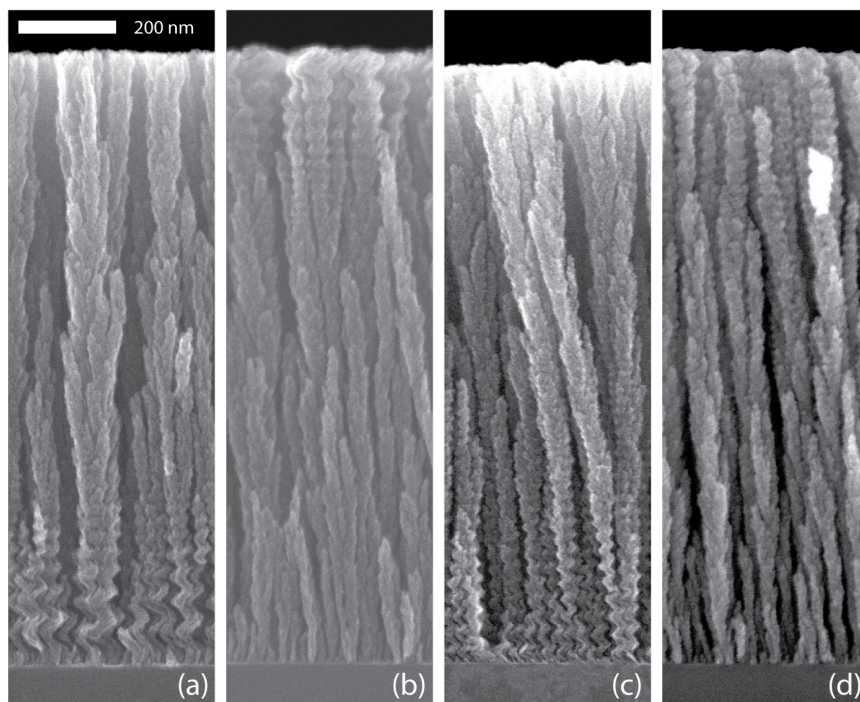



Figure 3.6: Films produced with pitch as a function of height, leading to helical and vertical post morphologies within the same column. Films (a) and (b) span pitches from 100 nm to 0.5 nm, both decreasing (a) and increasing (b) with increasing height. Films (c) and (d) focus more tightly on the transition between vertical post and helical morphology, spanning 10–45 nm pitch. In both films, the transition point is not clearly defined. Hysteresis also occurs in the films—the film pitch at the transition point is not the same when film pitch increases as it is when film pitch decreases.

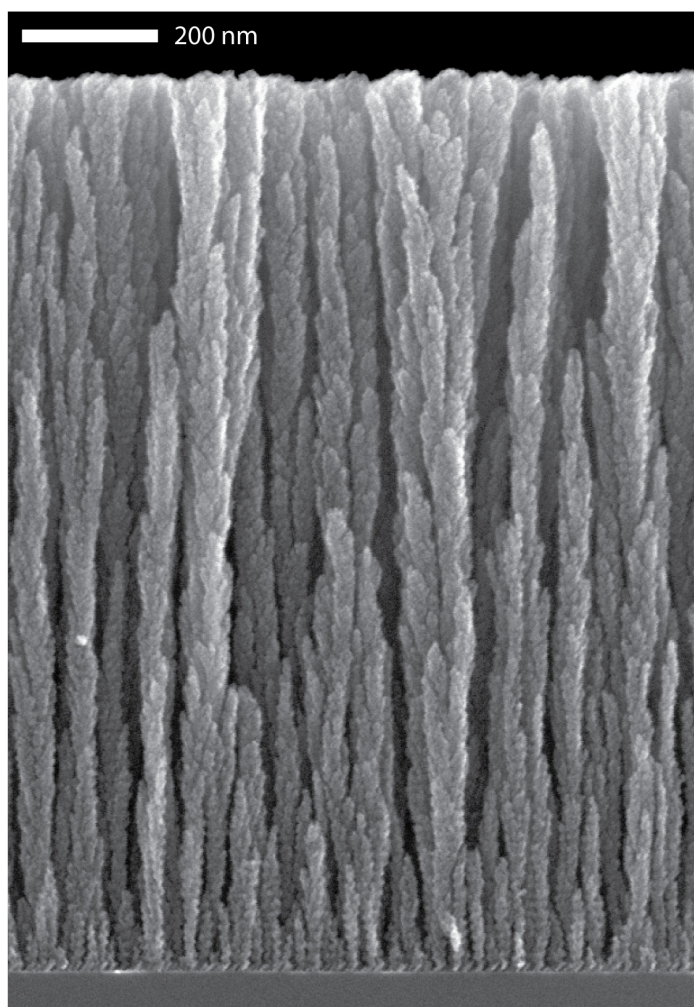


Figure 3.7: TiO_2 GLAD film deposited at $\alpha = 81^\circ$ and a nominal pitch of 16.7 nm to a 1500 nm nominal height. The film displays the characteristic ripples of a GLAD helix while exhibiting the general shape and branching structure of a vertical post film, suggesting a gradual transition regime between the two.

using the same (h, α, ϕ) triplets described in Section 3.1.2. We anticipated hysteresis in the transition point, so I also deposited the opposite film with *increasing* pitch, shown in Figure 3.6b. To improve precision, I then repeated the above across a 10 nm–45 nm pitch range, producing the films shown in Figure 3.6c–d.

In Figure 3.6c, a transition occurs at approximately 440 nm, 36% of the actual film height. Similarly, the transition in Figure 3.6d seems to be largely complete at 800 nm, or 63% of the actual height, though the point is not clearly defined. These correspond to a pitch range between 17 nm and 26 nm. An additional deposition at 33.3 nm pitch adopted distinctly helical morphology, supporting this upper bound.

Within this range, a film at 17 nm nominal pitch exhibited both vertical post-style branching and the ripples typical of helical posts,

Graduated-pitch films allowed pinpointing of the helix-post transition point.

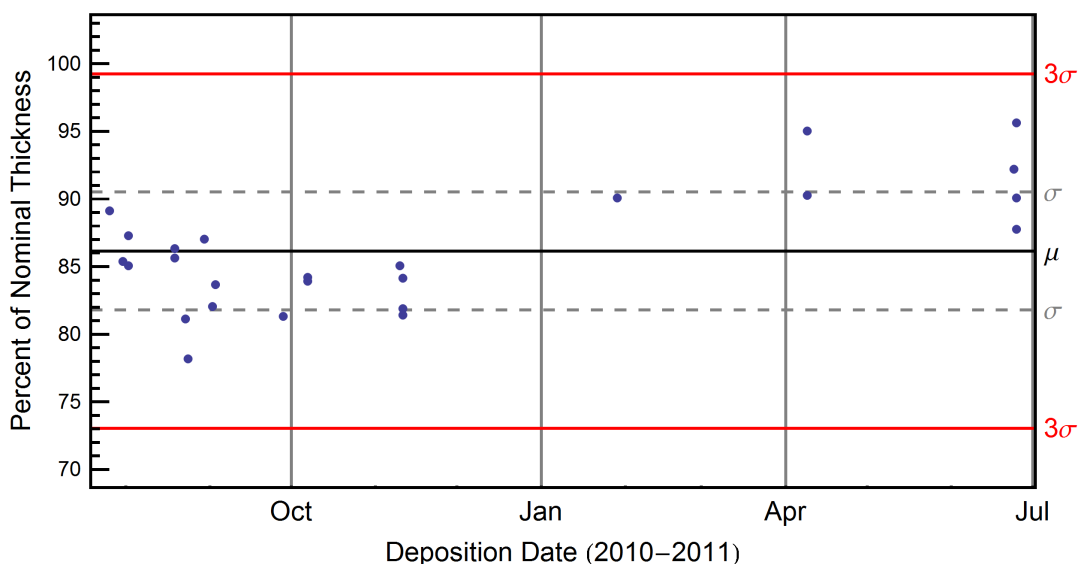


Figure 3.8: Control chart of measured film thicknesses, expressed as a percentage of nominal thickness. Measurements are taken from 2-10 cross-sectional SEMs of a $\sim 1 \text{ cm}^2$ section of each substrate. In depositions utilizing the rotation stage, thickness is only reported for the root shaft, as these thicknesses are not independent. Though no datapoints appear outside the 3σ control line, repeated values below then above the median suggest non-random changes in the process equipment [114].

suggesting a gradual transition between the regimes. This morphology is shown in Figure 3.7, and suggests that some degree of control over the surface of GLAD structures may be available without serious alteration of the overall column shape. Further investigation would be necessary to map the degree to which such control is possible.

3.3.2 Film thickness control

I deposited each film in this study to a nominal thickness of 1500 nm. A scanning electron microscope (Hitachi S-4800) imaged a $\sim 1 \text{ cm}^2$ section of each film in cross-section, allowing measurement of actual heights in ImageJ³. The SEM is guaranteed by the manufacturer to a lifetime 5% accuracy, confirmed by the SEM operators with NIST calibrated samples⁴. Measured thicknesses were consistently below the nominal value, averaging 86%—this shift likely indicates inaccuracy in the tooling factor used to calibrate the QCM output.

A consistent shift in thickness is of little concern when studying pitch effects across a wide range. Variation between depositions has

³ ImageJ v1.45 is produced by the National Institute of Health (Bethesda, USA) and available at <http://rsbweb.nih.gov/ij/index.html>

⁴ This was verified from personal correspondence with Daniel Salamon, then Technical Officer at the National Institute for Nanotechnology.

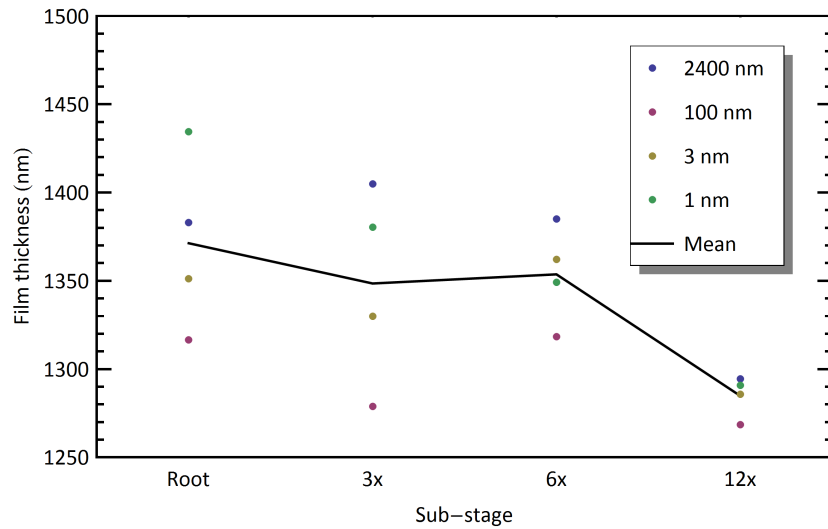


Figure 3.9: Variation in thicknesses produced by the four shafts during deposition. The legend indicates the pitch of the root shaft; all other shafts rotate faster, and thus produced films with lower pitch. As expected, films grown on the root shaft are thickest.

more significant experimental implications, however, as ϕ rotation is based on nominal height values: sub-nominal film thickness indicates sub-nominal film pitch. To better characterize variation, I developed the control chart seen in Figure 3.8, which traces measured height as a proportion of nominal height over the course of the thesis. The lop-sided nature of the measurements is indicative of long term changes to the apparatus or procedure, resulting in an unexpected thickness increase. The trend is statistically significant, with a p-value below 0.02%. The standard deviation of measured thickness is about 4% of the nominal thickness, which remains minor given the two orders of magnitude studied in pitch.

A component of thickness variation can be explained by uneven flux hitting the substrate; as discussed in Section 3.2.1, film farther from the deposition source grows slower. When ϕ is constantly rotated, the center of the chuck remains at a constant distance, and ultimately receives the least flux: in $\alpha = 70^\circ$ TiO_2 vertical posts, Wakefield and Sit reported a 1% thickness increase at a radius of 4 cm from the chuck center [113]. This discrepancy is expected to increase for film deposited farther from the chuck.

3.3.3 Rotation stage morphologies

I predicted a more extreme thickness variation across rotation stage shafts, as there is none of the chuck's large-scale motion to equalize incident flux. Rather, thickness variation should be similar to that in oblique deposition. Figure 3.9 shows thicknesses measured from four

Studied pitches spanned orders of magnitude, making thickness inconsistencies minor concerns.

Rotation sub-stages produced slight thickness variations.

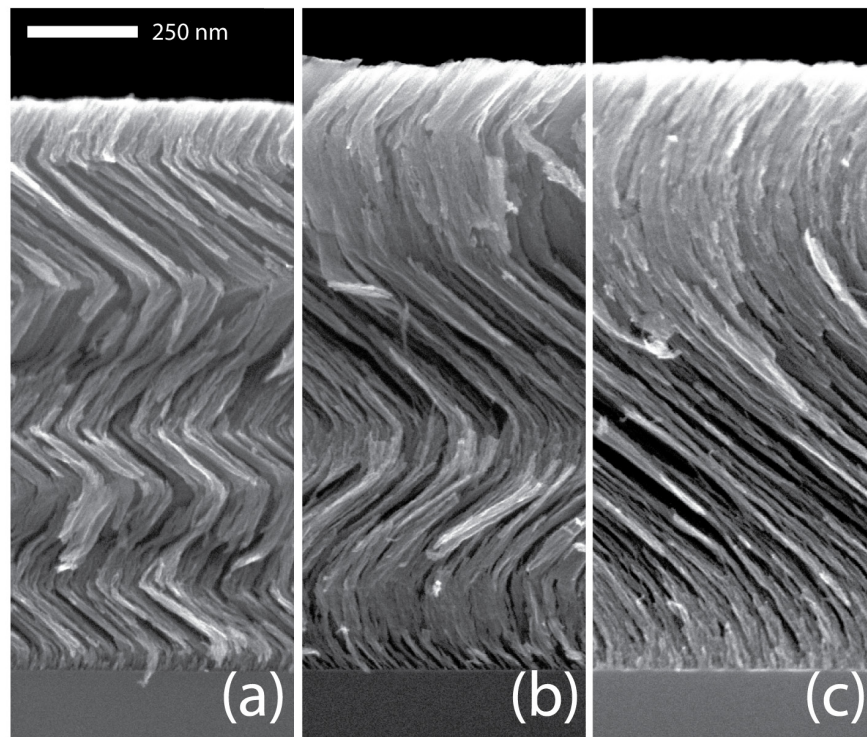


Figure 3.10: TiO_2 $\alpha = 81^\circ$ films deposited at 200 nm (a), 400 nm (b), and 800 nm (c) pitch using a rotation stage root pitch of 2400 nm. Films produced on the two stages farthest from the root shaft (a, b) display distinct jumps in their morphology caused by gears sticking at slow rotation rates. Similar defects were not observed at root pitches of 100 nm and lower, at which all gear rotation was smooth.

separate depositions, confirming the expected decrease in height in shafts further from the root shaft. The average thickness difference from the root to the outermost shaft is 6%, in close agreement with the approximations presented in Section 3.2.

At root pitches of 100 nm and below, morphologies were qualitatively indistinguishable from those produced on a traditional chuck. With a root pitch of 2400 nm, the significant defects shown in Figure 3.10 appeared in the 12x shaft's film; the extremely slow rate of rotation caused the final shaft to jerk discontinuously during deposition.

INITIAL MEASUREMENTS OF GROWTH SCALING

As the list of potential GLAD applications grows, so too does the need to carefully optimize and control nanostructure morphologies. This is especially true in the case of the vertical post, among the most widespread structures within the research community.

As described in Section 2.3, vertical posts broaden as they grow, and several groups have characterized this broadening experimentally by analysing p , defined in Equation 2.33. No clear trends have emerged in literature, and considerable variation in p exists from study to study. Furthermore, a clear understanding of the sensitivity of p to deposition pitch has not yet been attained.

Determining pitch's effect on broadening in TiO_2 , a common high- T_m oxide of great interest to the research community, was thus my first goal. This chapter describes my initial work toward this end, utilizing previously described techniques:

- A. CROSS-SECTIONAL SEMs permit direct measurement of column width, usually at a handful of discrete heights, which can then be fit to the power law (Equation 2.33). This technique allows continuity with the existing TiO_2 work of Taschuk *et al.* [33], providing insight into the method's repeatability.
- B. PARTICLE ANALYSIS ALGORITHMS identify individual posts within top-down SEMs, measuring the area of each identified objects. This allows large-scale automated measurements of column diameter in each SEM. With multiple films grown to different thicknesses, these diameters can also be fit to the the power law, as described by Kaminska *et al.* [74].
- C. MANUALLY COUNTING posts in top-down images can simplify image analysis. This only requires measurement of the total area occupied by post objects in each thresholded SEM, eliminating the need for algorithmic particle subdivision. Dividing this area by the number of posts in the field of view estimates mean post area, which can again be fit to Equation 2.33.

In all three cases, results indicated a lack of repeatability and consistency with literature values; in their survey of growth scaling literature, Taschuk *et al.* reported a similarly high degree of scatter in literature results [33]. This inconsistency, coupled with the low throughput of the techniques, provides the motivation for the subject of the next chapter: the development of a new method of measuring broadening in GLAD films.

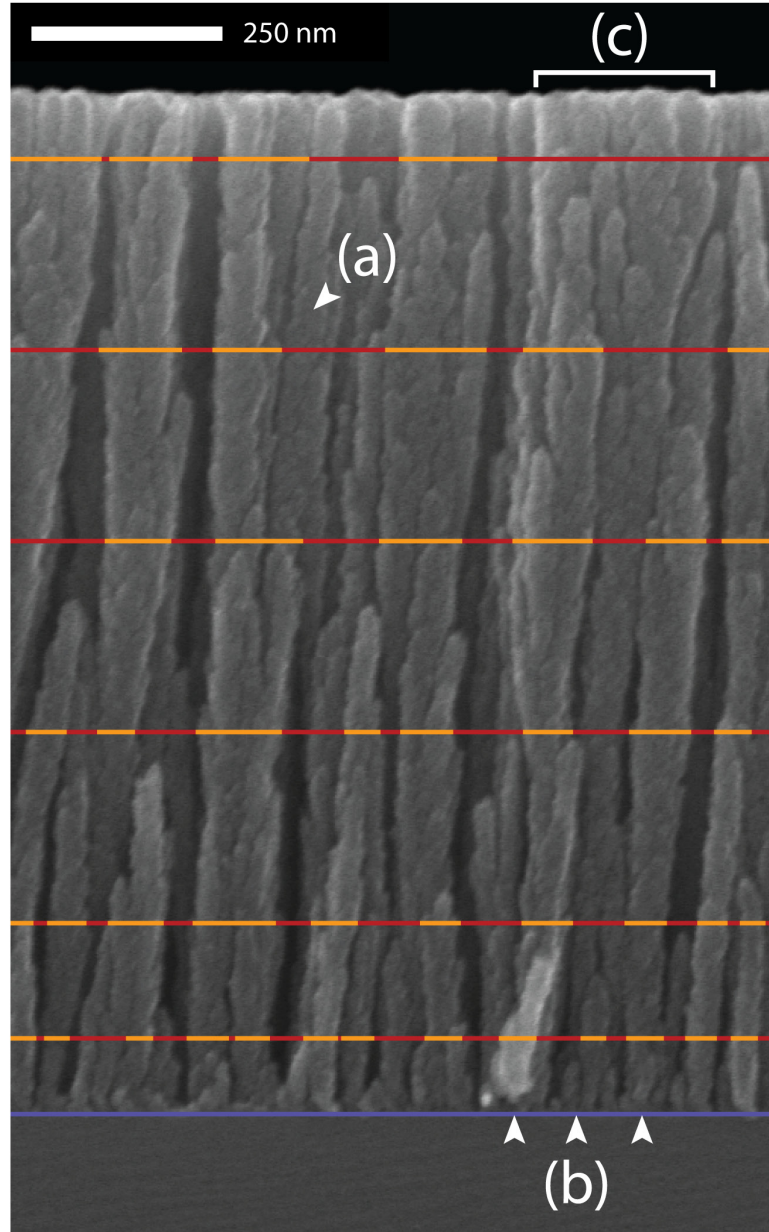


Figure 4.1: Cross-sectional SEM of a TiO_2 $\alpha = 81^\circ$ film deposited at 0.5 nm pitch. I manually measured the width of every apparently distinct column at heights of 100 nm, 250 nm, and every 250 nm thereafter; column measurements are indicated in orange. Note the uncertainty inherent in distinguishing individual columns from the branches of those columns. Misinterpreting large branches as individual columns will underestimate column width, while including too many branches in a column measurement overestimates. It is often difficult to determine whether branches belong to a particular column or those behind it (a), and columns that appear separate at the substrate (b) are often indistinguishable at the top of the film (c).

4.1 CROSS-SECTIONAL BROADENING MEASUREMENTS

I took a minimum of five separate cross-sectional SEMs at different locations on samples grown at 100 nm, 10 nm, 1 nm, and 0.5 nm pitch. The 100 nm pitch film exhibited helical morphology, while the rest produced vertical posts. To facilitate comparison with Taschuk *et al.*, I replicated his measurement procedure in ImageJ:

1. DRAW GUIDELINES along which measurements are to be taken: every 250 nm above the substrate surface, with an additional line at 100 nm. I calibrated all distances with the scalebar produced by the SEM.
2. MEASURE THE WIDTH of every distinct column along these guidelines, attempting to capture whole columns rather than individual column branches.
3. REPEAT THIS PROCEDURE for at least three SEMs per film, producing between 300 and 500 measurements. This doubles the measurements per film reported by Taschuk *et al.*[33], reducing the effect of random error.
4. FIT THE MEAN WIDTH at each height to the power law given in Equation 2.33, extracting p and ω_0 for each film using Mathematica¹. In all cases, data produced only minor scatter around power law fits. Expressed as percentages of corresponding fitted values, residuals had a standard deviation of $\sim 5\%$.

Post diameters are directly measured from cross-sectional SEMs.

Steps 1 and 2 are displayed in Figure 4.1.

Figure 4.2 displays the results of this investigation: no power law dependence is observed in the helical sample², but all three vertical post films produce fitted p values near 0.4, summarized in Table 4.1. Taschuk *et al.* report a significantly higher value of $p = 0.59$ for a TiO_2 film at $\alpha = 81^\circ$ though their experimentally determined relationship between α and p predicts the smaller value $p = 0.49$. This discrepancy is consistent with their reported film-to-film variability, with 1σ variations as high as ± 0.16 in TiO_2 films at different α values. They do not report film pitch in their paper, but it does lie within the 10 nm to 0.5 nm span covered here³.

Discrepancy in p is consistent with large spread in reported literature values.

Taschuk *et al.* report that ω_0 values are less varied, and their $\alpha = 81^\circ$ value of $\omega_0 \approx 85$ nm agrees closely with the the vertical post values reported in Table 4.1.

Much of the challenge in reproducing consistent results lies in distinguishing columns from their neighbours in the complex branching morphology of TiO_2 GLAD. The high depth of field of the scanning

Edge measurement of heavily branching films is subjective and difficult to repeat.

¹ Mathematica 8.0.1 is produced commercially by Wolfram Research, and is available at <http://www.wolfram.com/mathematica/>.

² Though the helical nanostructure does not appear to broaden, it is possible that the helix radius increases with height—an excellent candidate for study in future work.

³ This has been verified in personal correspondence with Dr. Taschuk.

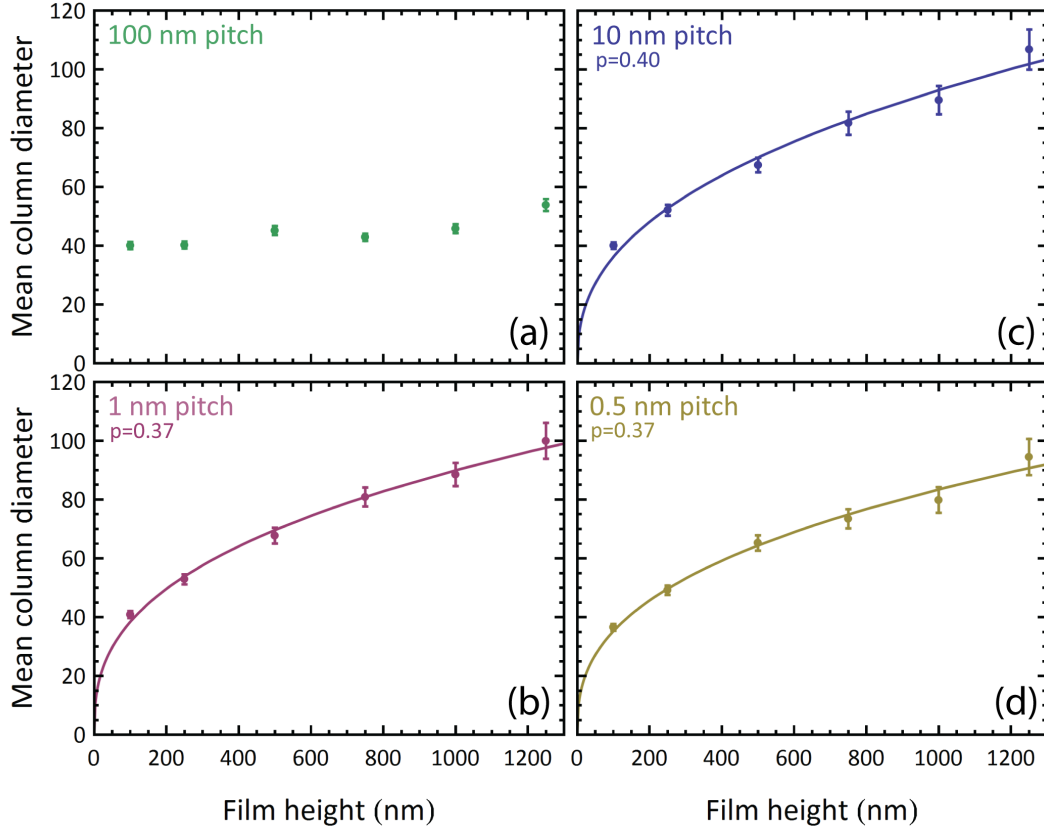


Figure 4.2: Data measured manually from cross-sectional SEMs of $\alpha = 81^\circ$ TiO_2 films, deposited at pitches of 100 nm, 10 nm, 1 nm, and 0.5 nm. I took between 300 and 500 measurements per film. Error bars represent the standard deviation of the mean; as fewer individual columns are visible higher in the film, error increases with increasing heights. The 100 nm pitch film adopted a helical morphology, and displays no power law trend in broadening. I fit the remaining films to Equation 2.33 in Mathematica, yielding the indicated values for p . These values do not display pitch dependence, nor do they agree with $p = 0.6$ reported by Taschuk *et al.* [33].

Pitch (nm)	p	ω_0 (nm)
100	-	48
10	0.41	93
1	0.37	90
0.5	0.37	84

Table 4.1: Fit parameters from Figure 4.2, created from cross-sectional measurements of four TiO_2 $\alpha = 81^\circ$ films. Though the helical film did not produce power-law dependence, the ω_0 parameter can still characterize average column width at a height of $1 \mu\text{m}$. Values for ω_0 agree much more closely with literature than do values for p .

electron microscope becomes an impediment, preventing easy column differentiation based on their depth within the film. Branches often mimic individual posts, and measuring the width of a post is largely a process of choosing which branches to include. Examples of the subjective choices in the measurement process are indicated in white in Figure 4.1; their ubiquity makes consistency from observer to observer—or even from film to film—difficult to maintain.

In addition to concerns of subjectivity, column width measurement can also be suppressed by measurement of extinct posts: outgrown and shadowed by their neighbours during deposition, these taper near their tips and do not obey power law scaling along their full length.

4.2 AUTOMATED TOP-DOWN SCALING MEASUREMENTS

Top-down SEM images of TiO_2 $\alpha = 81^\circ$ films grown to a series of thickness were available from previous, unpublished studies⁴. Analysing these films offered a separate approach to growth-scaling, introducing automation to potentially increase the number of objects measured.

The extant SEMs imaged films of 250 nm, 500 nm, 1000 nm, 1500 nm, 3000 nm, 6000 nm, and 8000 nm thickness, all deposited at 5 nm pitch. If posts do broaden according to a power law, their maximum diameter occurs very near the top of the film. Top-down SEMs thus provide a realistic estimate of average post diameter at the film's thickness, and p can be extracted by fitting the power law to the changing average diameter across a series of thicknesses.

Post diameters are extracted from measurement of post top areas.

The most obvious practical drawback of this technique is its inherently low throughput; the analysis of a single morphology requires numerous depositions to differing thicknesses. Uncovering trends across a range of pitches thus demands an impractical number of depositions, even if the process of analysis can be automated.

4.2.1 Overall segmentation procedure

To measure the width of individual columns within a SEM, I used the following basic process flow in ImageJ:

1. A GAUSSIAN BLUR with $\sigma = 2 \text{ px} \approx 2 \text{ nm}$ smoothed the image, reducing pixel noise present in the original SEMs. The blur radius is kept small to minimize its effect on the measured object areas, which are also affected by the subsequent thresholding.
2. A THRESHOLDING PROCEDURE separated the image into foreground and background regions. This is explained further below.

⁴ These films were grown and imaged by Dr. J. Steele in 2009, working alongside Dr. M. Taschuk. I performed all the analysis described in this section.

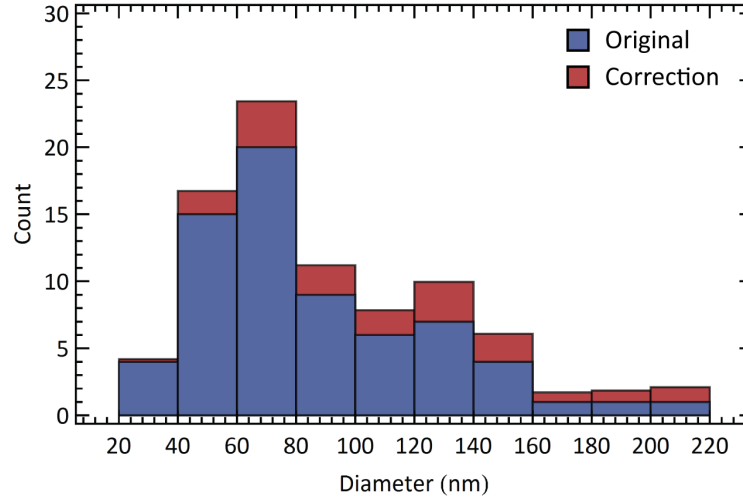


Figure 4.3: Distribution of object diameters extracted from a 250 nm film, subjected to a Gaussian blur and automated thresholding. No watershed filter was applied. Red additions indicate the correction of Equation 4.1, which weights larger objects more heavily, as they are more likely to have been excluded for lying on the edge of the image. The correction increases overall means.

3. A WATERSHED ROUTINE optionally separated individual objects incorrectly joined together after thresholding, theoretically preventing overestimation of diameter. Again, this is discussed further below.
4. BUILT-IN PARTICLE ANALYSIS identified each of the now-separated foreground regions, permitting area measurement. From each area A , I calculated an equivalent radius $r_{eq} = \sqrt{A/\pi}$, given as the radius of an equivalent-area circle. Averaging these radii estimated the mean column diameter at each height, to which I fitted Equation 2.33 in Mathematica 8.0.1.

As in any top-down SEM, a portion of objects touch the image's edge. As their full extent is unknown, they must be excluded from analysis. Simply removing them skews the distribution of objects, as larger objects are more likely to fall along the edge of the field of view. To counteract this, the "count" ζ of each object must be weighted according to the equation

$$\zeta = \frac{W_x W_y}{(W_x - F_x)(W_y - F_y)} \quad (4.1)$$

where W_x and W_y are the width and height of the field of view, F_x and F_y are the width and height of the object in question [115]. Small objects, relatively unlikely to fall on the edge, retain a corrected count

near 1, while larger objects are weighted more heavily in the corrected distribution. This affects calculation of both the mean

$$\bar{d} = \frac{\sum \zeta_i d_i}{\sum \zeta_i} \quad (4.2)$$

and the standard deviation

$$\sigma_d = \sqrt{\frac{\sum \zeta_i (d_i - \bar{d})^2}{\sum \zeta_i}} \quad (4.3)$$

of the effective diameters d_i . Figure 4.3 gives an idea of the magnitude of this change, showing distribution corrections taken from a 250 nm thick film. Such corrections become more crucial as individual posts occupy a greater portion of the field of view, as in the dataset's thicker films.

4.2.2 Thresholding considerations

Grayscale SEM images typically have pixel values between 0 (black) and 255 (white), with top-down SEMs producing light-coloured posts on a dark background. Thresholding simply maps all pixels below a certain value to black, and all pixels above the value to white. The boundary value can be determined either through manual inspection or with a thresholding algorithm [116].

Thresholding separates post from non-post in SEMs, leaving posts white.

Though knowledge of SEM content may aid accuracy, manual thresholding can be inconsistent from operator to operator [115]. Figure 4.4 provides an example of this inconsistency, with two observers measuring the same dataset. The results in Figure 4.5a also reflect the considerable variation between the two individuals, producing an unacceptable 30% discrepancy in the extracted p values of 0.12 and 0.18.

Numerous thresholding algorithms exist with strengths in different applications, often originating in studies of optical character recognition (OCR) [115, 116]. In this study I relied on the ImageJ variant of the *isodata* algorithm, developed by Riddler *et al.* [117]. One of the simplest approaches to thresholding, this iteratively divides pixels into foreground and background clusters, separating pixels at the value midway between the mean intensities of the foreground and background. Though more sophisticated algorithms may perform better, top-down SEMs do exhibit bi-modal histograms in their pixel values, supporting this midpoint as a reasonable estimate [116]. Figure 4.5b shows the fitted curve produced using this algorithm, yielding $p = 0.22$. Though Kaminska *et al.* do report the software package used in their analysis, it is not clear which underlying algorithm is employed [74].

A bi-modal intensity histogram supports isodata as a reasonable approximation.

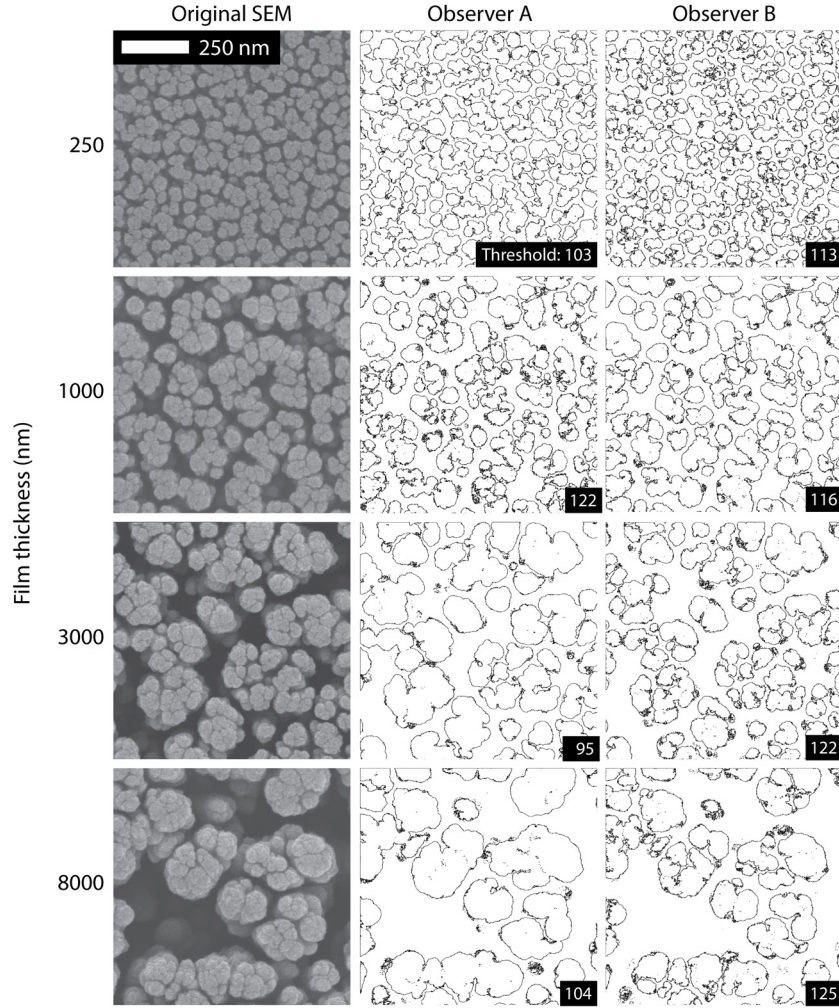


Figure 4.4: Top-down SEMs of TiO_2 $\alpha = 81^\circ$ films deposited at 5 nm pitch are binarized by two separate observers, with the outlines of thresholded objects displayed in black. The inset in each image indicates the selected threshold value between 0 and 255. Images are not blurred prior to thresholding. Generally, the *isodata* algorithm and Observer A tended to select values closer to 100, while Observer B remained between 113 and 125. Observer B thus measured more small objects, deflating his measured diameters in Figure 4.5. This subjectivity hinders measurement repeatability.

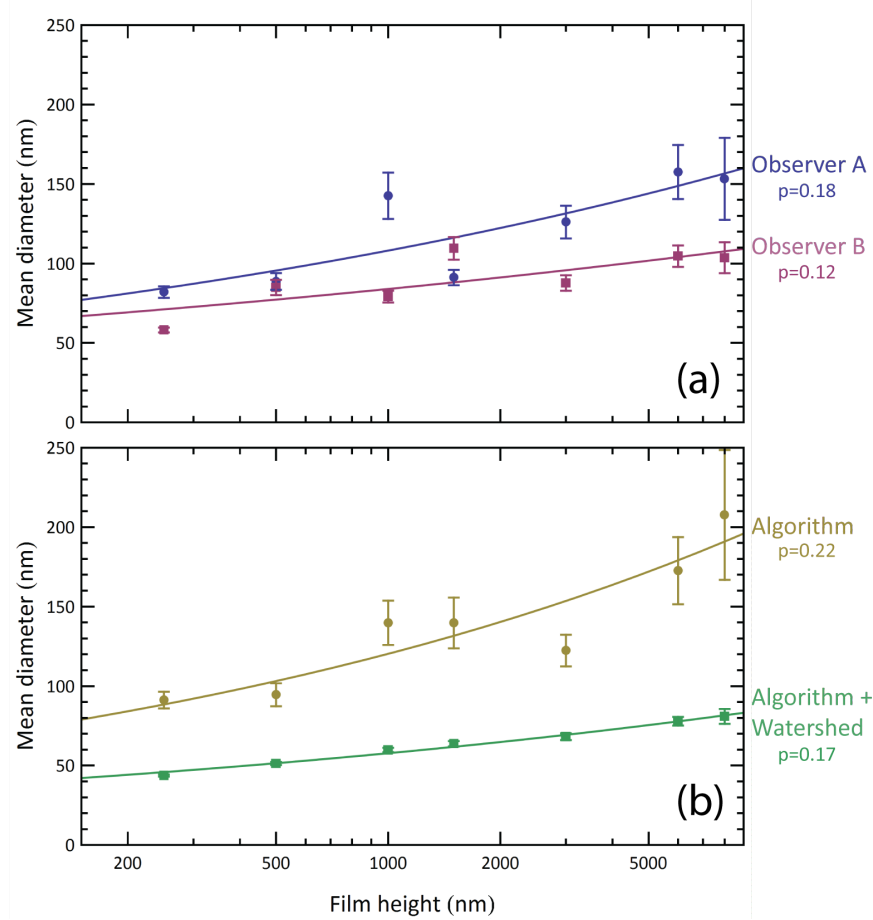


Figure 4.5: Fits of the power law (Equation 2.33) to average post diameter in a TiO_2 $\alpha = 81^\circ$ film, deposited at 5 nm pitch. Automated particle analysis measured a single SEM of each film, grown to thicknesses of 250 nm, 500 nm, 1000 nm, 1500 nm, 3000 nm, 6000 nm, and 8000 nm. In (a), two separate individuals thresholded the blurred image, producing differences in p values extracted from power law fits. No watershed filter was applied. The data in (b) use an automated thresholding routine with and without a watershed filter, which tends to over-divide large objects into smaller parts and underestimate effective diameters. Differences between the four fits highlight the challenge in producing consistent results from automated top-down particle analysis.

4.2.3 Watershed considerations

The watershed routine gets its name from an intuitive explanation of its mechanism: the routine assigns a “height” to each foreground pixel based on its distance to the nearest background pixel, with higher pixels being furthest away. This forms a mountainous topographic relief, with “peaks” in the interior of foreground regions—in our case, the interior of post objects. Water flowing down from these peaks covers all of the foreground pixels. In an object containing two peaks, there will exist a line between them that is flooded from both, thus forming a drainage divide or watershed. The algorithm draws a line of separation here, and is extremely effective at separating conjoined convex regions [115].

Figure 4.6 demonstrates the effects of a basic watershed algorithm and its qualitative success on thinner films: nearby columns joined in thresholding are split, correcting an overestimation of column diameter at lower thicknesses. The algorithm tends to divide larger posts into artificial sub-parts, however, underestimating column diameter at higher thicknesses. Diameter measurements with and without the watershed filter are visible in Figure 4.5b, demonstrating the reduction in reported diameter. A power law fit produces $p = 0.17$, significantly lower than the $p = 0.22$ produced without the watershed. Qualitatively, over-segmentation seems to affect more objects than are improperly joined, and thus the filter seems to decrease accuracy.

Kaminska *et al.* rely on a more complex grain analysis tool, dividing objects based on their aspect ratios and with algorithms similar to the watershed filter [74]. Their demonstrated data does not display similar sub-segmentation, and generally seems to separate joined convex regions. Even this separation, however, is not always desirable; joined objects often seem to be individual branches from the same column, and dividing them thus results in underestimation of column diameter. Comparisons of their oblique SEMs and the grains detected in their top-down images suggest that this negatively affected their results.

The watershed algorithm splits joined convex regions.

4.2.4 Variation in automated data

Differences among the fits shown in Figure 4.5 highlight the complexities of automated particle detection. As demonstrated, thresholding techniques severely impact resultant data, and the complex surfaces of post tops makes it unclear which thresholding algorithm is best-suited to the task, if any. Further, nearby columns are often joined in the denser, thinner films, leading to overestimation of mean diameter. While a watershed filter can separate these, applying it to the larger columns of thicker films results in excessive object sub-division and compromises diameter estimation. To a degree, this could be over-

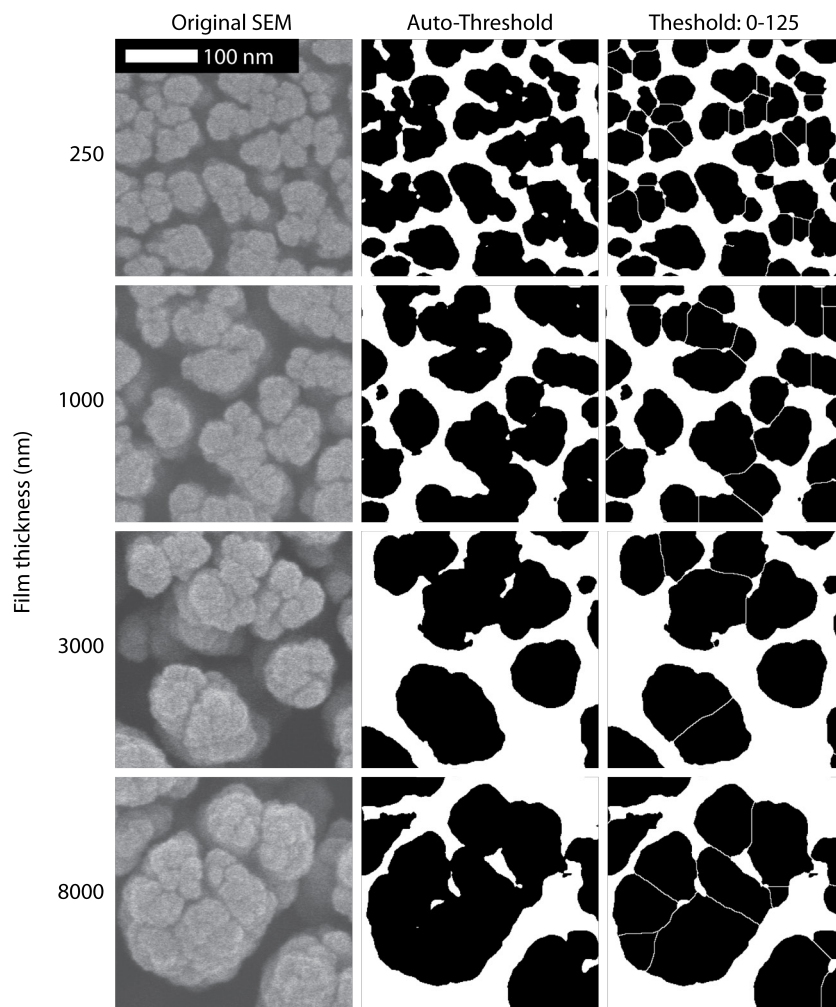


Figure 4.6: The series of 5 nm pitch films shown in Figure 4.6, subjected to a Gaussian blur and automated *isodata* thresholding. The third column demonstrates the effects of the basic watershed algorithm. The algorithm seems to correctly divide adjacent columns improperly joined in the thresholding of the 250 nm sample, but seems to over-segment the larger objects present in images of thicker films. This leads to an underestimation of the average column diameter.

come with a more complex, marker-based or multi-scale watershed filter, or by changing image magnification to maintain roughly constant object size.

Beyond such analysis considerations remain underlying challenges produced by the morphologies themselves. As in the cross-sectional SEM analysis of Section 4.1, their branching nature means that a single column can produce multiple separated objects at the full film height. If separation is too great, these objects will be treated as separate columns by particle analysis algorithms. The high SEM depth-of-field again becomes a problem, as extinct columns below film surface may also be visible.

Well-separated branches cannot easily be automatically grouped.

4.3 MANUAL TOP-DOWN SCALING MEASUREMENTS

Some complications of automated particle analysis can be sidestepped through manual post identification. I performed the Gaussian blur and thresholding routine as before, then extracted the area fraction of the SEM covered by the posts and branches. I then manually counted each apparently independent post in each image, allowing me to estimate the average post area at each thickness by dividing the area of the threshold foreground by the number of posts in the field of view.

Manually counting posts eliminates particle sub-segmentation, and human observers can group well-separated branches.

4.3.1 Average area vs. average diameter

In the automated segmentation techniques discussed above, equivalent circular diameters can easily be produced for each measured segment, and these can be averaged to find an estimate of the mean post diameter at each height. Though it may seem appropriate, it is incorrect to use the identified average post area \bar{A}_{eq} to calculate the average post radius. This can be understood by considering a distribution of radii: squaring them prior to averaging inflates the influence of larger values, skewing the average upwards when the square root is taken.

Circles described by a population's average radius and average area are not necessarily the same.

Mathematically, this is because expectation values of random variables are non-multiplicative, unless the variables are completely independent: the expectation value of the square of a random variable is not equivalent to the square of the variable's expectation value. Even in the simple case of a Gaussian distribution of r_{eq} , with mean \bar{r}_{eq} and variance σ^2 , the expectation value of the post area $\langle A \rangle$ can be calculated as:

$$\langle A \rangle = \langle \pi r_{eq}^2 \rangle = \pi \langle r_{eq}^2 \rangle = \pi (\bar{r}_{eq}^2 + \sigma^2) \quad (4.4)$$

Thus, calculating $\langle r_{eq} \rangle$ from $\langle A_{eq} \rangle$ requires knowledge of the radius variance, which manual post counting does not provide.

Recovering p from \bar{A}_{eq} requires manipulation of the standard power law (Equation 2.33) to compute a formula for the expected column area at each height:

$$2 \cdot r_{eq} = \omega_0 h^p \quad (4.5)$$

$$\pi r_{eq}^2 = \frac{\pi \omega_0^2}{4} h^{2p} \quad (4.6)$$

$$A_{eq} = \frac{\pi \omega_0^2}{4} h^{2p} \quad (4.7)$$

where $2 \cdot r_{eq}$ represents the column diameter. This then allows p to be extracted from a fit of the data across the thickness range, as before.

4.3.2 Manual count considerations

Even to a human observer, there were inherent difficulties in distinguishing posts and branches. Though I attempted to do so based on their proximity, shape, and orientation, the same objects could often be justifiably divided in several different ways. Especially in the thinner films, posts are not clearly separated and often intermingle in long, continuous chains. To estimate the impact of this subjective division on the ultimate data, I performed three counts on each image: once assuming each post to be as large as reasonably possible, once as small as possible, and once taking my best guess as to their extent.

Branch grouping causes measurement subjectivity, reducing repeatability.

As before, the effect of edges needed to be considered. Without measurements of each individual post, and thus without knowledge of their distribution, applying the counting adjustment of Equation 4.1 was impossible. Instead, I only counted posts in contact with the top and left edges of the film, discarding those touching the bottom and right. Though most accurate with perfectly convex objects, this reasonably approximates the effective number of posts contributing to the overall area fraction [115].

I thus calculated average post area by taking the total area of the foreground pixels in each image, using the *isodata* algorithm discussed above, and dividing by each of the three manual counts to attain a best estimate and a minimum and maximum value. The best estimates at each height are then fit to the power law (Equation 2.33).

Note that thresholding error is still present in this method.

4.3.3 Manual count results

Figure 4.7 shows a fit of Equation 2.33 to the best estimate of post counts, producing values of $p = 0.30$ and $\omega_0 = 117$ nm. This does not agree with the above techniques, producing a p that falls in-between the $p \approx 0.2$ produced through particle analysis and the $p \approx 0.4$ produced from manual edge measurements, summarized in Table 4.2 at the end of this chapter. Bounds on manual counts are widely spaced,

Bounds on manual post counts are widely spaced.

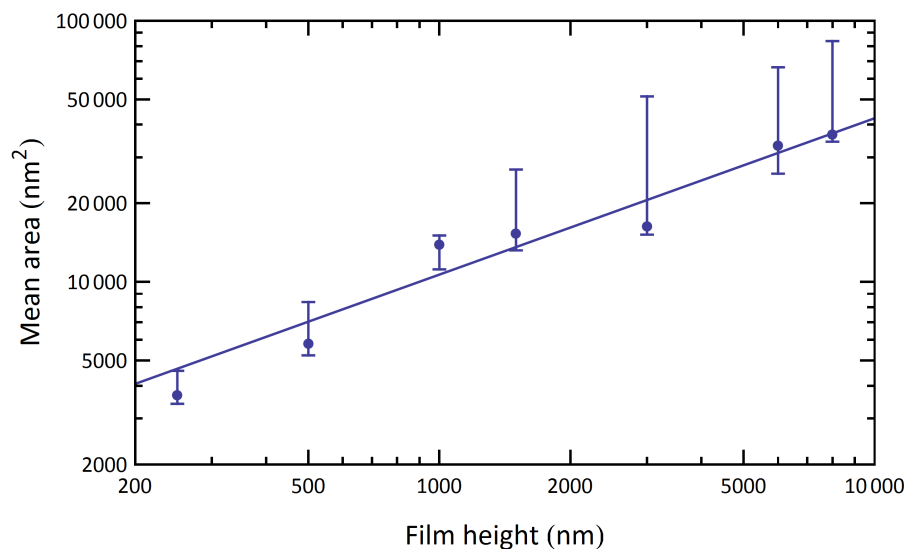


Figure 4.7: Estimates of mean column diameter extracted from the same series of images used in Section 4.2. I produce mean areas by dividing the foreground area fraction by a manual count of the posts contained in each image. To put boundaries on the uncertainty in differentiating posts, each image was counted three times: once making the most conservative assumption as to the extent of individual posts, once making the most liberal, and once taking a best guess. The latter data is fit to Equation 4.7 to calculate a p value of 0.30, and the boundary guesses are used to produce the shown error bars on the mean object area. The extent of the uncertainty, plotted here on a logarithmic scale, highlights the difficulty in correctly grouping objects in the highly branching film.

indicating that results could vary substantially depending on the observer. Thus, though free from the complications of particle analysis, error is still introduced into this method through the inherent difficulty in distinguishing columns and branches.

4.4 SUMMARY OF INITIAL MEASUREMENTS

Table 4.2 summarizes the results of the three techniques used in this chapter, which are neither self-consistent nor consistent with existing literature on TiO_2 growth scaling. Though improvements could be made in all of the above to minimize experimental bias, all are fundamentally subject to error introduced by subjective judgement of column extent. Furthermore, techniques that rely heavily on human measurement are inherently limited in their throughput; unfortunately, the visual complexity of the film makes the tasks poor candidates for computer aided vision.

In addition to the subjectivity of the measurements, a more subtle problem may further complicate analysis. Each of the above tech-

Pitch (nm)	Procedure	p	ω_0 (nm)	Source
10	Cross-section measurements	0.41	93	
1		0.37	90	
0.5		0.37	84	
?	Cross-section measurements	0.59	~ 85	[33]
	Cross-section model prediction	0.49		[33]
5	Manual thresholding	0.18	108	
	Manual thresholding	0.12	90	
	Auto. thresholding	0.22	120	
	Auto. thresholding + watershed	0.17	58	
	Manual post counts	0.30	117	

Table 4.2: Summary of the measurements produced using the three techniques in this chapter: manual measurements from cross-sectional SEMs, automatic particle-detection algorithms applied to top-down SEMs, and manual post counts combined with thresholded foreground areas. Data from [33] is included for comparison purposes; pitch is not reported in this paper. The data exhibits considerable scatter, and it is unclear which is the most accurate. Much of the uncertainty stems from the difficulty in correctly grouping posts and branches.

niques rely on calculating a single metric—mean post diameter or mean area—at a variety of thicknesses, and then fitting these means to the power law (Equation 2.33). This implicitly assumes that the value of p that best describes the film is the one that produces these means. As in the discussion of average diameters in Section 4.3.1, this is not necessarily the case; if film columns have a distribution of p values, columns with higher p will contribute disproportionately to these mean metrics due to the non-linearity of the power law. The actual mean of the column distribution, p_μ , will describe diameters and areas that are lower than the means measured by these techniques. Methods that extract p from individual columns—used in literature by Krause *et al.* [77] and Main *et al.* [73]—thus estimate this p_μ rather than the effective p measured by the above. The extent of the difference between these two values is entirely dependent on the distribution of p within the columns of the film, and is discussed further in Section 5.5.1.

The inconsistencies in the above data thus motivate the search for a technique that minimizes measurement subjectivity, forming the basis of the disassembly technique discussed in the next chapter. By disassembling the GLAD film and analysing each column individually, it also provides insight into the distribution of p within the film’s columns. This in turn can be used to evaluate the equivalence

High p variation may skew average diameter measurements.

of the p produced by the above and the actual p_μ , potentially providing additional explanation as to the inconsistency of literature p measurements.

DISASSEMBLY OF GLAD FILMS

Conventional methods of quantifying GLAD growth scaling are subject to operator bias, cumbersome, or provide limited insight into extinct posts. Literature measurements of p show little consensus or repeatability [33].

This chapter briefly describes the advantages and shortcomings of literature techniques, and then describes a novel alternative: ultrasonically shaking GLAD columns into solution, dispersing them across a bare Si wafer to facilitate machine vision, and algorithmically measuring the broadening profiles of well-separated columns¹. I describe the method in detail below, applying it to TiO_2 $\alpha = 81^\circ$ GLAD films grown at a series of pitches. To evaluate the technique's weaknesses, I examine both the effect of SEM resolution on data quality and the problem of post fragmentation, which raises questions as to the origin of posts shorter than the height of the film. Finally, I quantify the effect of pitch on column broadening, also examining the distribution of p values present within the films.

5.1 INTRODUCTION AND MOTIVATION

As discussed in Section 2.3.5, literature values of p are inconsistent and difficult to repeat. Challenges often stem from limitations in measurement techniques, many of which rely on observer judgement to discern individual posts. Though trivial in many films, the convoluted and branching nature of TiO_2 GLAD makes this process highly subjective. Figure 5.1 displays the different methods used to measure p from GLAD samples:

*Branching films
complicate manual
post measurement.*

- A. TOP-DOWN SEMs allow large-scale measurement of column spacing and diameter at the top of the film. Growing films to different heights under identical conditions permits measurement of changing column diameter with thickness, which can be fit to Equation 2.33 for extraction of p and ω_0 [74, 118]. As investigated in Section 4.2, the process can be automated using relatively simple image recognition algorithms, generating statistically significant sample sizes.

¹ A version of this chapter has been accepted for publication. J.M.A Siewert, J.M. LaForge, M.T. Taschuk, M.J. Brett. "Disassembling glancing angle deposited films for high-throughput, single-post growth scaling measurements," accepted April 15th, 2012 to *Microscopy and Microanalysis* (<http://journals.cambridge.org/action/displayJournal?jid=MAM>)

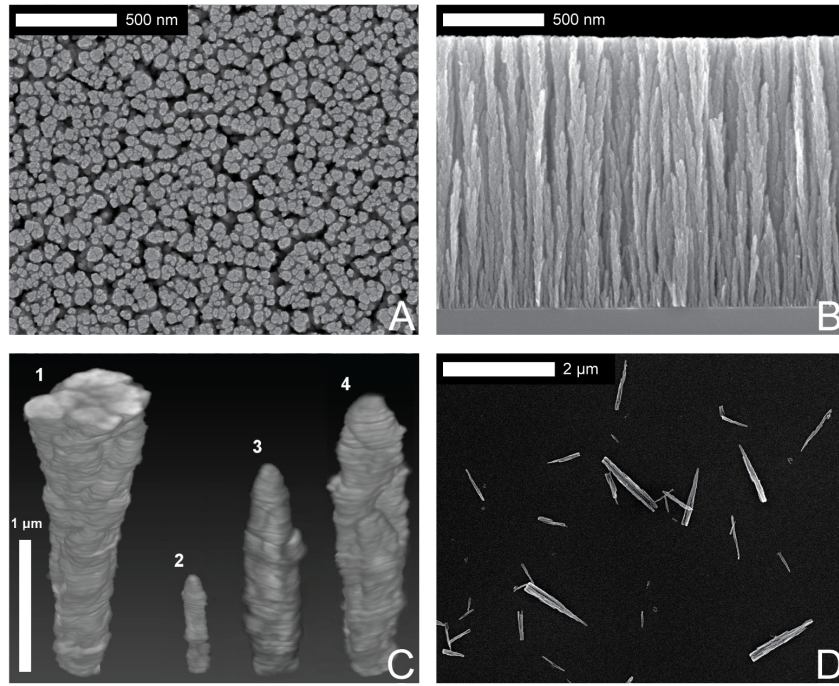


Figure 5.1: Different approaches to measuring GLAD film (TiO_2 , $\alpha = 81^\circ$) growth scaling. Top-down views (A) require multiple depositions of different heights to fully characterize scaling. Branches and individual posts are difficult to distinguish both in top-down views and in cross-sectional views (B). Though focused ion beam tomography (C) provides extremely precise insight into both full-height and extinct post morphologies, it is extremely low-throughput and does not lend itself to large-scale film characterization. The method (D) described here allows automated analysis of individual, isolated posts from a simple SEM image. FIB image (C) is reproduced with permission from [77].

Requiring samples at multiple thicknesses necessitates multiple time-consuming depositions at each parameter set, rendering the technique unsuitable for high-throughput analysis. In highly branching films, such as the titania films grown here, it is often difficult even for human observers to distinguish sufficiently separated branches from individual posts, resulting in potential underestimation of p . Finally, if particle-analysis techniques are used to identify individual posts, results are highly dependent on the thresholding and particle separation algorithms employed. This may further contribute to lack of consensus in literature. A top-down view of a titania GLAD vertical post is shown in Figure 5.1a.

Top-down scaling analysis requires multiple films at each set of parameters.

- B. CROSS-SECTIONAL SEMs, as used in Section 4.1, allow direct measurement of post width as a function of height and have been used extensively in existing literature [33, 71, 79, 119]. The technique is labour-intensive, and GLAD's visual complexity precludes straightforward automation. Measuring the width of all distinct columns at a handful of film heights allows reasonable sample sizes, but can be compromised by the visual similarity of posts and branches in many oxide films (Figure 5.1b). Incorrectly identifying branches as independent posts can suppress or inflate reported p values. The alternative method—choosing individual posts and manually tracing their perimeter—limits sample size, making subtle trends extremely difficult to distinguish from random error.
- C. FOCUSED ION BEAM (FIB) TOMOGRAPHY begins with the infiltration of the GLAD columns with a polymer. The resultant film is imaged in a dual-beam configuration: an electron beam images the surface, while a focused ion beam strips off material in layers. The images of each layer can be tomographically assembled into a full three dimensional model of the original GLAD structure [77]. This technique not only provides full information on the broadening of the post studied, but provides unparalleled insights into branching behaviour and surface morphology. Further, the technique can be applied even to extinct posts beneath the surface of the film, offering insight into the competitive growth processes inherent in GLAD.

Distinguishing branches from columns is highly subjective and difficult to repeat.

FIB analysis provides high detail but low throughput.

Though FIB provides a unique level of detail, it is hindered by complications inherent in polymer infiltration, an extremely low rate of imaging, and a small field of view. These restrict its use to very small numbers of individual columns, precluding conclusions about the aggregate film. Data like that shown in Figure 5.1c remain essential as a useful comparison for alternative methods.

There is a need, then, for a method permitting accurate recording of post width profiles while lending itself to computer automation.

5.2 THE DISASSEMBLY TECHNIQUE

The aim of this method is to efficiently and accurately measure the width profile of GLAD structures, enabling detailed and statistically significant study of their growth-scaling properties. The technique presented here accomplishes this by separating and dispersing posts across the dark background, as shown in Figure 5.1d. The clear separation of foreground and background facilitates automated and image analysis while clearly demarcating individual columns.

Isolating columns makes automation practical.

The technique is similar to previous work by Gilbertson *et al.* [120] on aerosolized nanoparticles produced via GLAD. The aerosol was dispersed across a bare silicon wafer to verify particle separation and to estimate the particle length distribution. No attempt was made to study column broadening, nor to automate analysis of the image—published SEMs possess a highly non-uniform background, suggesting that computerized image-recognition would have been complex under their experimental conditions.

There are four essential components to the disassembly process presented in this chapter, each open to optimization:

1. DISASSEMBLING the GLAD film into its constituent columns and suspending them in a liquid solvent, here using ultrasound. Column clumping and fragmentation are undesirable.
2. DISPERSING the nanoparticle suspension evenly across the substrate, here using a standard spin-coater. Ideally, posts will be as close together as possible without frequent contact. Solvent should evaporate completely to preserve the uniformity and contrast of the Si surface.
3. IMAGING the dispersed columns at resolution sufficient to accurately fit Equation 2.33, while catching as many columns as possible in the field of view.
4. IDENTIFYING columns in the SEMs using machine vision, and extracting and fitting the width profiles of each column to provide broadening data.

The method I employ is still far from optimal, but acts as a proof of concept and produces novel quantitative insights into the growth scaling of TiO₂ vertical post films. This section outlines the initial, rudimentary study of each of the above steps, along with the final, functional set of parameters employed.

There remains room for improvement on this functional implementation.

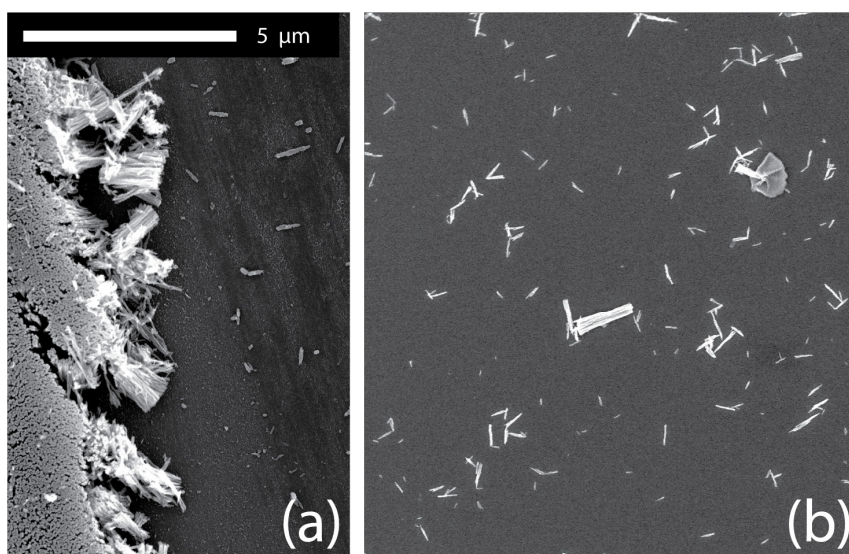


Figure 5.2: Nanocolumns of a 1 nm pitch TiO_2 $\alpha = 81^\circ$ film, given a 48 h hydrophilicity-enhancing UV treatment, scraped into water with a straight-edge razor, and spun onto a bare Si wafer (10 drops). A scraped region of the original substrate is shown in (a), and the resultant dispersion of columns is shown in (b). The razor appears to create undesirable debris and results in poor column separation; many clusters retain their in-film configuration, and separated columns appear to have clumped together during solvent evaporation. Columns are too sparse on the final wafer.

5.2.1 Disassembly considerations

The ultrasonic disassembly of a GLAD film influences both the condition of the columns and their final arrangement on the Si wafer. Ideally, individual nanocolumns will be well-separated, but spaced as closely as possible without multiple columns coming into contact: this simplifies image analysis while minimizing the necessary microscopy. Sonication is also responsible for separating columns not only from the substrate, but also from each other. Insufficient sonication can leave columns clinging together in their original in-film configurations. Too much sonication risks their destruction.

The use of GLAD films' constituent nanostructures is not new. Groups occasionally use GLAD to create designer particles with particular shapes and compositions [121, 122]. GLAD columns have even been grown onto magnetically active catalyst particles, then separated from the substrate to form self-propelled structures whose movement through liquid can be externally controlled [123, 124]. Additionally, GLAD films are commonly studied via transmission electron microscopy (TEM), in which an electron beam is directed through individual, isolated GLAD nanostructures [78, 125–129]. To prepare samples for TEM, they must be strewn across a conductive mesh [130].

Posts should be maximally dense while minimizing contact.

All the above scenarios require dismantling the GLAD film and removing it from the substrate. In many TEM applications, this is accomplished simply by scraping films with a razor, snapping columns off either onto a TEM grid, or into an intermediary liquid solution later pipetted onto the grid. Figure 5.2 shows the application of this technique to the films studied here, scraped into deionized water before being spun onto a bare Si wafer. The method appears to produce detritus from the substrate itself and poorly separates the clusters of columns in the original film. Given the low tolerance for clustering and foreign objects in automated image analysis, this method appears unsuitable. Some razor-based disassemblies also resulted in few posts within the SEM field of view, lengthening the imaging process with a search for isolated nanocolumns.

Razors produce debris that complicated image analysis.

The ultrasonic alternative discussed here immerses the film in liquid and uses soundwaves to physically shake columns free from the substrate. The fact that GLAD columns broaden from a single nucleated seed aids this process, as the column base is generally its narrowest point and thus the site of detachment. Ultrasonic cleaners are widely available and direct the waves through a water bath: “sonicating” films is a simple matter of placing the substrate in a beaker of a desired solvent, and suspending the beaker within the bath. Early ultrasonic trials produced improved results over razor based techniques, but required consideration of both solvent-film interactions and sonication parameters.

GLAD posts appear to snap off near the substrate.

Solvent selection and UV treatments

Trials using de-ionized water as the solvent produced columns in small, widely-spaced clumps. Suspecting poor adhesion between water and the surface of the TiO₂ columns, we applied an ultraviolet treatment to enhance TiO₂ hydrophilicity, as discussed in Section 2.4.2 [100, 102]. Note that films were treated prior to solvent immersion; some solvents, including water, are UV-absorbent [131].

Increasing substrate-solvent interaction encouraged post separation.

Ultraviolet treatment improved results and permitted comparison UV-treated films in water and isopropanol, shown in Figure 5.3. Both presented satisfactory results, and I used the rapidly-drying isopropanol thereafter.

The final parameters saw the films placed 14 cm below an 8 W UV bulb (UVP MRL-58) for 48 h. After treatment, ~ 1 cm² wafer sections were cleaved off and immersed in 8 mL of isopropanol, contained in a clean 50 mL beaker. To prevent nanoparticle contamination from one batch to the next, I cleaned glassware with alternating hydrophilic and hydrophobic solvents:

- SCRUBBED with Citranox, a commercial glassware cleaner, and rinsed with deionised water.

Nanoparticles were visually indistinguishable from one sample to the next; detecting contamination would be difficult.

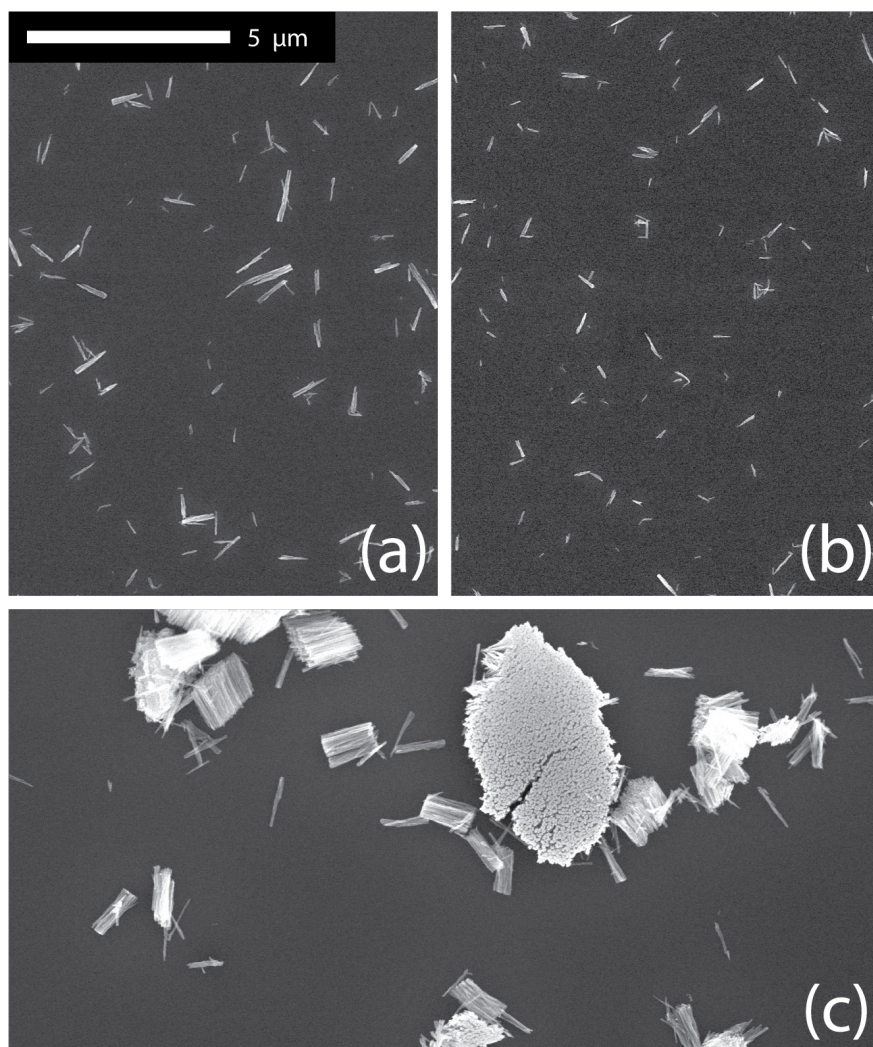


Figure 5.3: Comparison of water (a) and isopropanol (b) solvents used in film disassembly. Both originate from the same 1 nm pitch film, treated with 48 h of UV and immersed in the solvents for a \sim 90 minute sonication. Differences in the distributions are qualitatively minimal, though the water-based disassembly seems to retain more post clusters. Differences are confounded with sonication intensity, which may vary with the location of the solvent beaker in the ultrasonic bath. Both dispersions represent significant improvement over samples not treated with UV (c).

- SONICATED for 3 minutes (at maximum power), filled with acetone.
- RINSED with isopropanol and deionised water
- SONICATED for 3 minutes (at maximum power), filled with deionised water
- RINSED with isopropanol and deionised water
- DRIED with compressed dry nitrogen

Substrate pieces were dropped into solvent film-side up, allowing visual monitoring of disassembly progress.

Ultrasonic cleaner considerations

Ultrasonic cleaners consist of a solvent bath—usually water—surrounded by a number of piezoelectric transducers generating ultrasonic compression waves throughout. With sufficiently powerful waves, the pressure between compression crests will be negative enough to tear microscopic voids in the solvent, known as microcavities. Hundreds of microns in diameter at 20 kHz frequencies [132], these cavities are unstable and reach temperatures as high as 5100° in their interior [133]. When they violently collapse, the implosion produces liquid velocities in excess of 100 ms^{-1} , displacing particles in the vicinity.

Though ultrasound refers to all frequencies above the threshold of human hearing (18 kHz), ultrasonic cleaners typically operate between 20 kHz and 80 kHz; higher frequencies produce smaller microcavities, but require more power to exceed the cavitation threshold [134]. Cavitation is extremely effective at cleaning surfaces regardless of their complexity.

Solvents should be degassed prior to sonication: dissolved gasses will collect in microcavities as they form, preventing their collapse and thus their violent action. Degassing is simply a matter of continuing sonication until bubbles of gas grow large enough to float to the surface. Higher temperatures encourage this process, reducing the capacity of the solvent for dissolved gasses. [132, 134]. Microcavities also form more readily at higher temperatures.

We used a Tru-Sweep 575D benchtop ultrasonic cleaner (Crest Ultrasonics) for all treatments. The device provided both a heating element with a bath temperature readout and a proprietary power scale (1-9) roughly corresponding to 40-100% of maximum output power². Beakers of various sizes were suspended from custom-designed styrofoam mounts that accommodated five simultaneously, with contained solvent below the waterline. Bath temperature consistently rose from room temperature to $\sim 50^{\circ}\text{C}$ over 100 minutes of sonication.

De-gassing is especially important during lengthy sonications.

² Data is taken from materials available on the Crest Ultrasonics website, at <http://www.crest-ultrasonics.com>.

The locations of beakers within the mounts were not controlled on the assumption that ultrasonic energy was roughly equivalent throughout the bath; Tru-Sweep cleaners sweep a range of frequencies to avoid standing waves. Inconsistent de-gassing of the water bath may have caused observed variability in dispersion quality; poor dispersions were either re-dispersed or imaged more extensively.

Though time did not permit investigation into optimal sonication times, samples sonicated for 100 minutes produced satisfactory output and I used this as a standard time for the duration of the experiment. Closer observation of some films revealed a rapid color change from the purple of the TiO_2 to the gray of the underlying silicon, suggesting removal of the film bulk within a minute of sonication onset. A more complete optimization of the disassembly parameters should thus study sonication length over several orders of magnitude, monitoring both its effect on column separation and the fragmentation of columns, discussed in Section 5.3.2 below.

Sonication time is a central parameter to future optimisation.

In an attempt to minimize nanocolumn agglomeration, I kept the ultrasonic cleaner directly beside the spinner for the duration of treatment, pipetting directly out of active sonication. Precise sonication times thus varied up to twenty minutes from sample to sample during batch processing.

5.2.2 Dispersion considerations

I spun each nanoparticle suspension onto a bare polished silicon [100] wafer, selected due to its ready availability, atomic smoothness, and high degree of contrast with nanocolumns under SEM. Unlike solvent selection, spinning parameters had a clear impact on the quality of the resultant column distribution, highlighted with the changing rotation speeds in Figure 5.4.

Imaging wafers were cleaved into approximately $\sim 10 \text{ cm}^2$ sections, then quartered again after spinning was complete—though no edge effects were apparent under the microscope, imaging a corner of the substrate initially at the center of the $\sim 10 \text{ cm}^2$ section eliminated the possibility of surface tension influencing the resulting dispersion.

I spun the wafer sections using a WS-200 series resist spinner (Lau-rell, WS-200-8NPP/RTV). The device had been manually calibrated, and thus actual rotation rates were only approximate, within ± 200 RPM. I transferred each solution to the rotating substrate using a different disposable glass Pasteur pipette, thus eliminating any chance of cross-contamination.

The spinning process offered two main factors for adjustment:

1. THE ROTATION SPEED set during the spinning process. For resist spinning and similar applications, rotation speeds are often set to ramp up, or to briefly spin at a lower speed to allow complete coating. Given the extremely low viscosity of isopropanol,

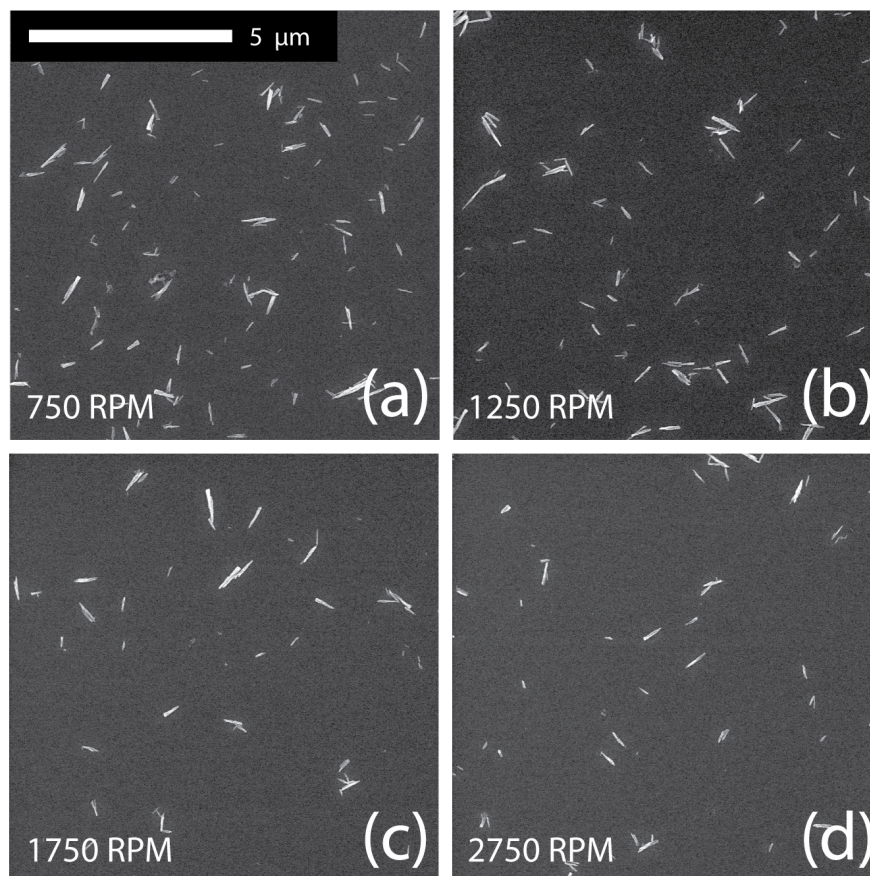


Figure 5.4: Comparison of spinning speeds of 750 RPM (a), 1250 RPM (b), 1750 RPM (c), and 2750 RPM (d). In each case, I gave films a standard UV treatment and sonicated them in isopropanol. I pipetted the solution directly out of sonication and onto the already-spinning wafer, applying 10 droplets with sufficient drying time between each. The above SEMs indicate increased clustering at low speeds (a) with a significant drop-off in post density with increasing rotation speed (c-d). I selected 1250 RPM as the standard rotation rate for the duration of the experiment.

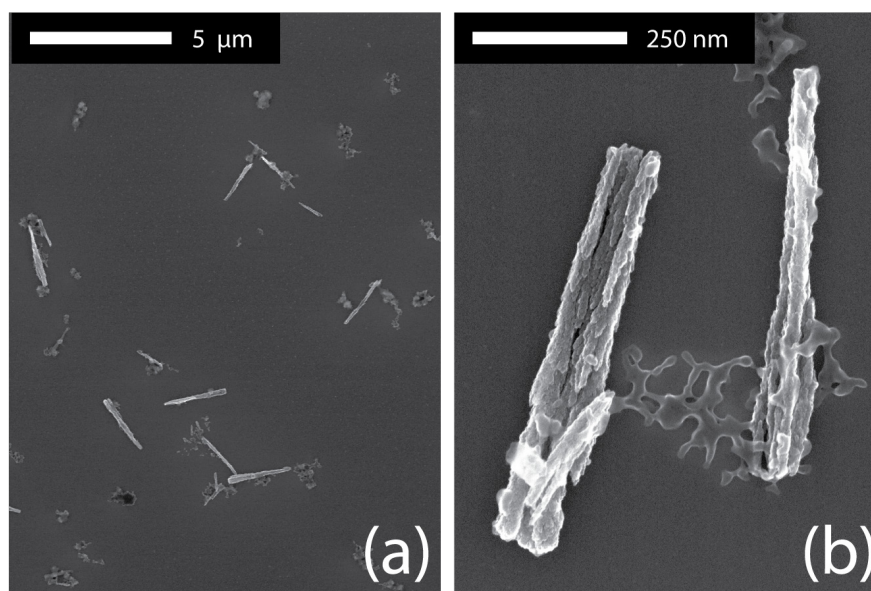


Figure 5.5: Examples of unknown contamination that appeared in some disassemblies. In some cases, contamination is sufficiently widespread to render the image useless for automated processing, forcing the disassembly to be repeated (a).

I deemed this unnecessary and pipetted directly onto wafers spinning at top speed. Generally, higher rotation speeds leave thinner liquid layers on substrate surfaces. This is consistent with Figure 5.4, with higher speeds leaving fewer columns on the wafer, and lower speeds permitting more column clumping. For the remainder of the study, I selected 1250 RPM (Figure 5.4) as the best balance of post density and clustering.

2. THE NUMBER OF DROPLETS pipetted onto the wafer during spinning. A single droplet of IPA evaporates from the spinning surface within seconds, with thin-film interference effects causing several color changes before complete disappearance. Multiple droplets can be pipetted onto the same wafer after drying intervals, increasing post concentration in the final dispersion. Ten applications of one to two drops of solution—the low viscosity made it difficult to produce droplets one at a time—yielded acceptable post densities. These applications were spaced ~ 10 s apart to permit solvent evaporation between treatments.

In several samples, unknown detritus appeared across the wafer, frustrating efforts to automatically identify posts. I initially assumed this to be residue from vacuum tape on the reverse of the substrates, which were entirely immersed in the solvent. This effect was difficult to reproduce even with whole pieces of tape left on the substrates, and the cause of such contamination thus remains an open question.

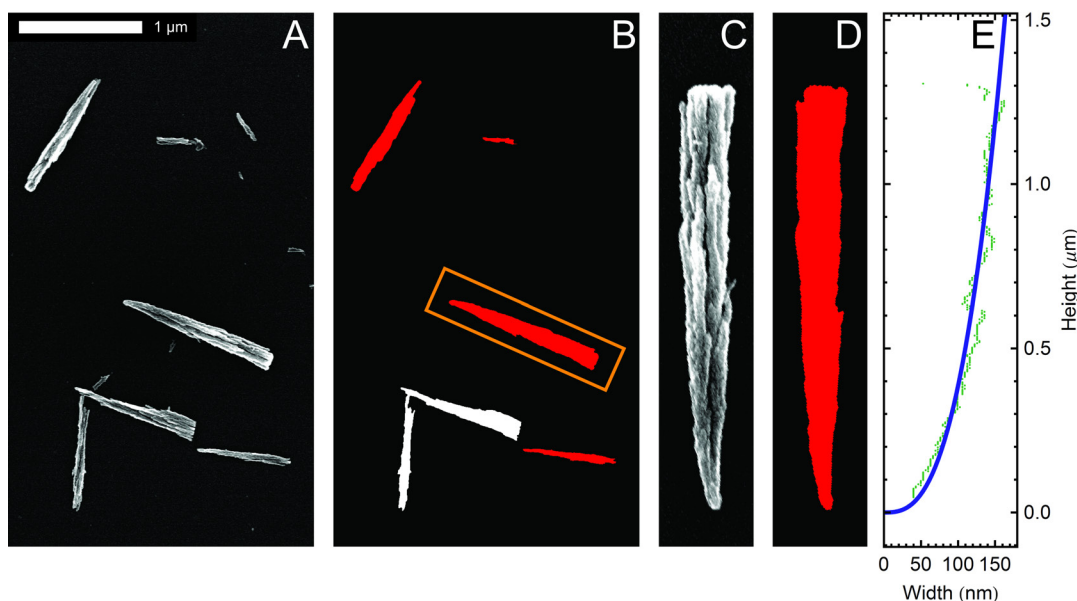


Figure 5.6: Image analysis procedure for sonicated GLAD posts. (A) SEM image of the spin-coated Si wafers. (B) Mathematica scripts are used to automatically segment post candidates, subsequently screened to separate isolated posts (red) from debris and clumped posts (white). For each isolated post candidate (C), Mathematica automatically measures the mask (D) to produce a broadening profile which is subsequently fit to the power scaling law (E) described in Equation 2.33.

5.2.3 Imaging considerations

Only the number of posts contained in each image, the contrast between post edges and the background, and resolution of post edges were priorities during scanning electron microscopy; detail of post interiors was irrelevant. In an attempt to maximize throughput, I imaged adjacent locations on the wafer, re-focusing only when required.

Initial images were taken using an Hitachi S-4800 at a variety of resolutions, using a 15 kV accelerating voltage with a 20 μA beam current. I selected 15 kX as an acceptable compromise between post resolution and the number of posts in each SEM image; standardizing magnification from image to image simplified analysis. At first, the process did not seem to require such a powerful instrument, and we began imaging with a LEO 1430 SEM at 21 kX. Both magnifications were selected from inspection, and many posts fell below the minimum necessary resolution. Future work will be better informed by the resolution testing provided below in Section 5.3.1.

Generally, 4-7 images could be taken before re-focusing.

5.2.4 Image analysis considerations

The above steps produced individual nanocolumns on a dark, uniform background, as shown in Figure 5.6a. We used a combination of human shape identification and Mathematica's image processing routines (8.0.4, Wolfram Research) to identify these columns (Figure 5.6b)³. Each isolated column (Figure 5.6c) produced a single mask (Figure 5.6d), which was in turn fit to Equation 2.33.

As part of this procedure, we applied the following workflow to each SEM image:

1. PRE-PROCESSING to remove noise
2. SEGMENTATION of foreground objects
3. MANUAL SELECTION of post candidates
4. MEASUREMENT of width profile data
5. FITTING of width profile to Equation 2.33
6. FINAL EXAMINATION of fitted profile to remove bad fits

Our routines identified all bright objects on the dark background of the wafer, which included both the isolated posts we wished to measure and a variety of "garbage" objects, including small clusters of touching posts, small post fragments, and a variety of non-post detritus. Though we ultimately wish to eliminate all human input in the analysis process, the algorithm currently requires the operator to manually identify isolated posts from among these other objects. A partial overview of the code involved is provided in Appendix B.2.

Pre-processing

After imaging, we commenced analysis by reducing noise using Mathematica's implementation of the total variation filter, which improved performance of the segmentation algorithm that followed. A non-linear noise removal algorithm, the variation filter analyses brightness gradients around each pixel to reduce Gaussian noise while preserving object edges [135]. Figure 5.7 contrasts its performance with the crude Gaussian blur used for the same purpose in Section 4.2 showing remarkable performance improvement.

The image is smoothed to reduce pixel noise.

Segmentation

We identified post candidates with a more sophisticated version of the watershed transform discussed in Section 4.2.3. Rather than determining flooding locations simply from proximity to background

³ The image analysis algorithms discussed here were designed and produced by Joshua LaForge.

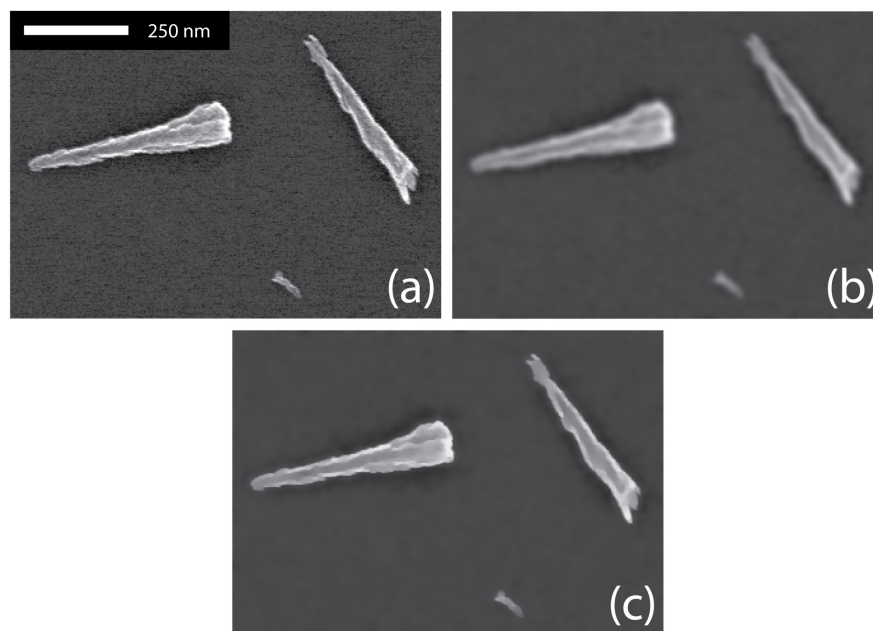


Figure 5.7: A disassembled $\alpha = 81^\circ$ TiO_2 film grown to 5 nm pitch and imaged with an Hitachi S-4800 (a). Though the Gaussian blur used in Section 4.2 does reduce noise in the image (b), the non-linear total variation filter does so while retaining edge sharpness (c).

pixels, we independently created a set of flooding markers [136] for the interior of each post and for the substrate background.

The generation of post interior markers is outlined in Figure 5.8a–c. Starting with the pre-processed image, sequential grayscale opening and closing filters smooth large objects to reduce over-segmentation while eliminating undesired small objects (Figure 5.8a) [137]. As markers can lie anywhere within post objects, edge detail in this step is superfluous. We binarize the result using Mathematica’s default thresholding algorithm, based on an Otsu clustering technique that minimizes intensity variance in both foreground and background regions (Figure 5.8b) [116]. Post objects are dilated to a skeleton (Figure 5.8c), which we prune to leave a single marker—often only a single pixel—inside each remaining object [137].

Creating background markers (Figure 5.8d–f) begins with a filling transform on the pre-processed image, eliminating dark spots within object interiors (Figure 5.8d). Separating out the background is then a two-step procedure: first, the image is binarized with a basic threshold at a low, fixed intensity value. This is used as a crude initial guess for a Chan-Vese binarization routine. Rather than purely relying on pixel intensities, this algorithm iteratively moves the foreground/background boundary to achieve maximum intensity separation while minimizing both the line length and the number of resultant islands [138]. This results in a contiguous background region and

Markers are separately produced for posts and the background.

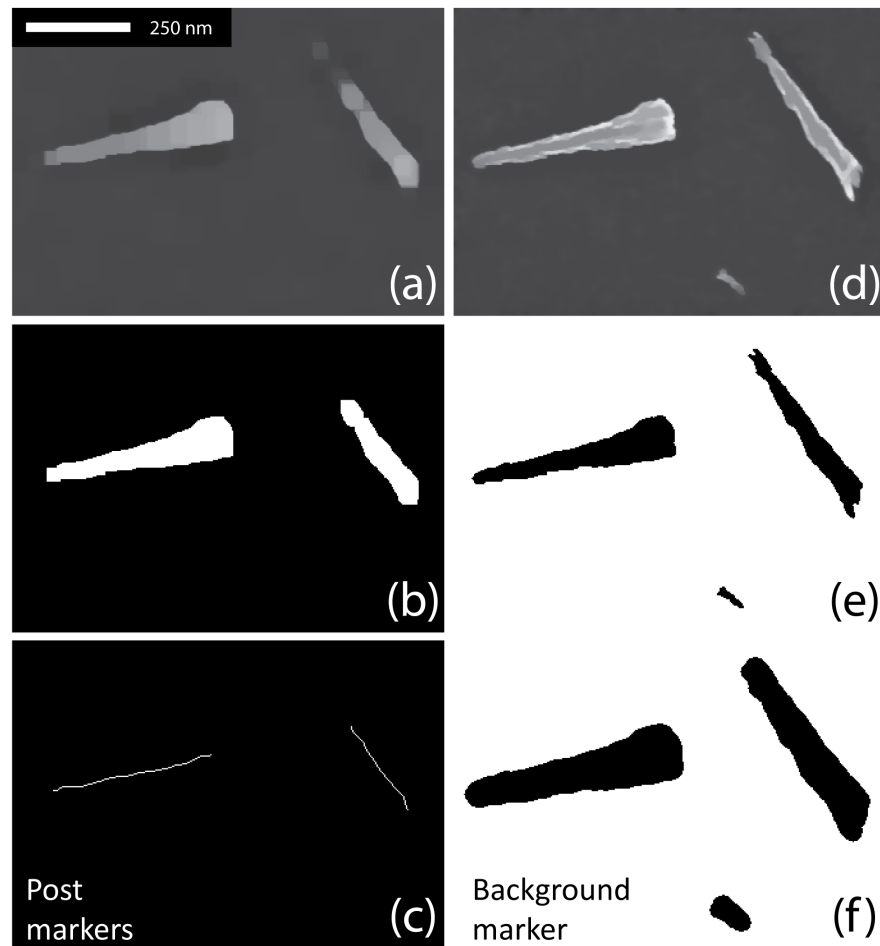


Figure 5.8:

POST INTERIOR MARKERS begin with sequential opening and closing filters on the noise-reduced image, producing the smoothed image (a). Small objects and remaining noise are eliminated. This image is binarized using Mathematica's implementation of Otsu clustering thresholding (b). This is thinned to a skeleton (c), which is pruned to produce a single marker for each post. BACKGROUND MARKERS start with a filling filter (d), which fills in local minima to prevent holes from appearing inside posts. This image is thresholded at a low constant value, selecting much of the substrate background. This background is used as an initial estimate for the more sophisticated Chan-Vese binarization algorithm (e), which divides the regions based morphological considerations rather than a flat threshold value. The result is dilated (f) to ensure that the background marker does not overlap with any post objects.

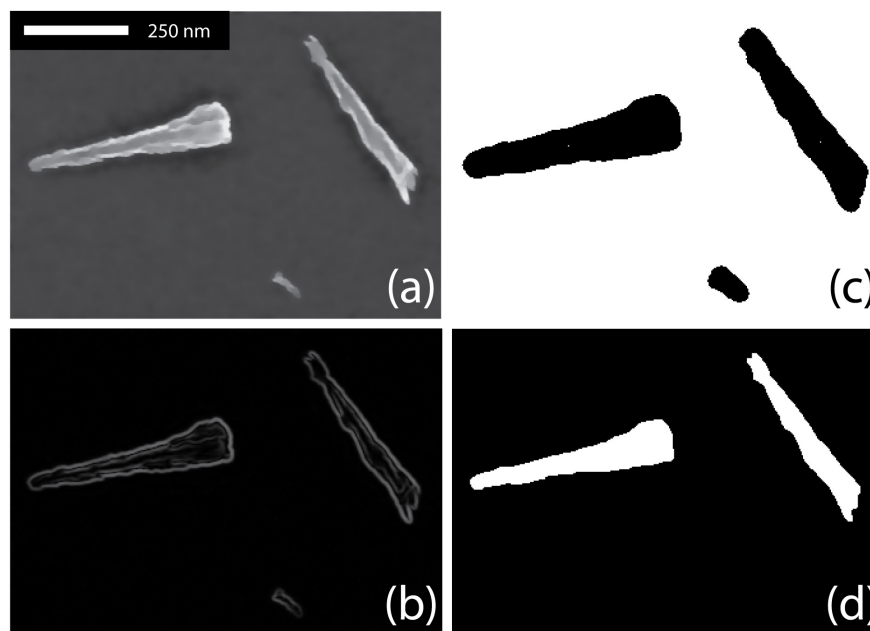


Figure 5.9: The pre-processed image (a) is treated with a gradient filter, which resets intensity values based on intensity gradients present in the initial image. The sharp changes between bright post objects and the dark background produce the bright post outlines visible in (b). Markers (c) at the interior of each post then become the peaks for a watershed filter preformed on these outlines, producing the final segmented image (d). Imagining water filling the image from these marker locations, it is clear that boundary lines will be correctly drawn at the “ridges” formed by the bright outlines.

can overcome background gradients problematic for simpler threshold techniques (Figure 5.8e). To ensure the background marker does not overlap with object edges, we apply dilation (Figure 5.8f).

We combined post interior markers with the background marker to produce an image like that of Figure 5.9c. A gradient filter makes regions of changing intensity bright and constant intensity dark, producing the bright object outlines shown in Figure 5.9b [115]. Using the markers as peak locations, a watershed filter on these outlines finally separates and segments each separate object in the SEM, and the binary image is now ready for manual object selection (Figure 5.9d).

Combined markers determine the watershed filling locations.

Manual selection

Segmented objects were now white on a black background (Figure 5.6b, without red colouration). I manually identified the actual posts in the binary masks, coloring them red them in ImageJ in a one-click macro process that hastened measurement. Initial iterations of this process further divided the objects into nine categories based on their

The method currently requires manual removal of non-post objects.

morphology, but we abandoned this process as subjective and impractical with larger sample sizes.

Eliminated objects included:

- Obvious clusters of multiple posts. Depending on the quality of the sample's disassembly, these could account for a significant portion of identified objects. In some eliminated cases, such as two overlapping posts forming an "X" shape, post data may still be recoverable with a more advanced set of algorithms, providing a source of improved efficiency.
- Objects that were too small to identify as either debris or posts. These seemed to include the smallest post fragments, as well as contaminants with obviously distinct morphologies.
- Obvious fragments of posts, with the break occurring across the width of an object with clear post-like morphology.

Having coloured each acceptably post-like object, I passed the images back into Mathematica for extraction of the objects' width profiles.

Measurement and fitting

Figure 5.6c shows a sample portion of an SEM containing a single object; the corresponding shape identified by Mathematica is shown in Fig. 5.6d. We calculated the object's width profile by first orienting it along its longest axis, then tracking segment width from its thinnest to thickest end, ignoring holes in the object interior. Width profiles were then converted from pixel counts to physical units and fit to Equation 2.33, allowing us to measure the parameters ω_0 and p for each post object (Figure 5.6e).

Width profiles are measured automatically.

5.2.5 *Final treatment parameters*

The final disassembly parameters utilized in this experiment for the disassembly and analysis of a GLAD film are outlined in Appendix A in detail sufficient for reproduction. At present, human input is only required for the manual selection of "good" posts; all other image processing steps are fully automated.

It must be noted that these parameters are suitable for the $\alpha = 81^\circ$ TiO₂ vertical posts studied here, but are not necessarily transferable to other GLAD morphologies. Shown in Figure 5.10 is a helical TiO₂ film at the same α , with helices clinging together in large rafts and maintaining their as-deposited configuration. Though flipped rafts permitted a unique bottom-up view into the film, of potential interest to future studies, the lack of isolated helices indicates that disassembling similarly dense morphologies will at least require a new set of treatment parameters.

Denser morphologies may require more sonication.

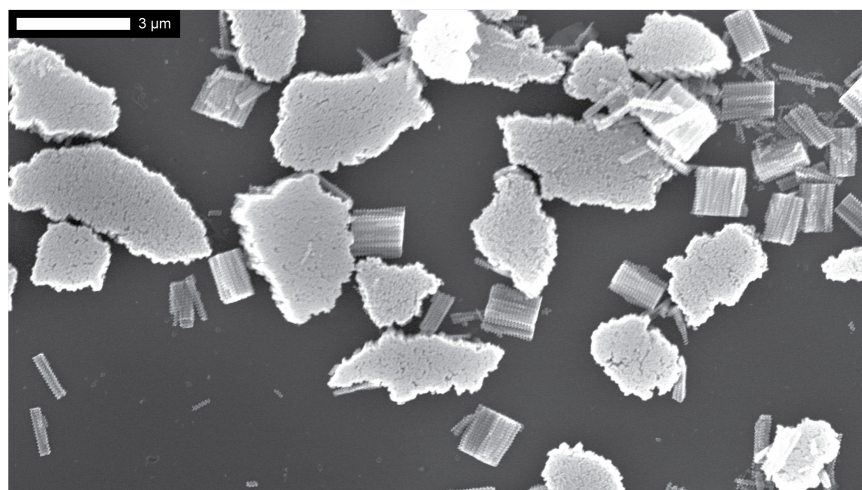


Figure 5.10: Given the same disassembly treatment as the vertical posts in this study, helical morphologies remained clumped together in large rafts that prevented analysis. Extension of the method to similarly dense films will require new disassembly parameters. We deposited the shown film at 100 nm pitch.

5.3 LIMITATIONS ON DATA VALIDITY

From a single GLAD film, the above process isolates large numbers of its constituent columns, measures their width profiles, and extracts the key parameters p and ω_0 . Before using these values to draw conclusions about the film, two factors must be considered: the limiting effects of resolution on fit accuracy, and the potential of column fragmentation affecting object populations.

5.3.1 Resolution limits on width profile fitting

Imaging GLAD posts with finite resolution makes regions of the full fitting parameter space defined by Equation 2.33 impossible to measure accurately due to under-specification of the model—that is, a post described by some p' and ω'_0 has a certain minimum resolution threshold below which fits of the post will yield incorrect values⁴. Thus, not all measured width profiles and fits should be kept for further analysis. This issue is inherent to any technique that relies on sampling or extracting the width profile of individual GLAD columns, including the edge, top-down, and FIB methods described in Figure 5.1 and Chapter 3. In this study, we only retain fitted post parameters that we expect to lie within a 10% tolerance of actual post parameters, shown in Figure 5.11. What follows is a rigorous descrip-

Minimum resolution for reliable fitting depends on post shape.

⁴ This approach to outlining resolution limits was conceived and executed by Joshua LaForge, who also wrote the requisite code in Mathematica. I used the results of this investigation to exclude objects of insufficient resolution from further analysis.

tion of the method used to estimate the regions within this tolerance and to filter measured data accordingly.

Width profiles for a column are characterized by the parameters identified in Equation 2.33: the total film height l , the characteristic column width ω_0 at $1\ \mu\text{m}$, and the scaling parameter p . These parameters are determined from non-linear fitting of the expected profile to quantized data taken from SEM images. Within the full fitting parameter space $S = \{X = (l, \omega_0, p) : l > 0, \omega_0 > 0, p > 0\}$, we estimated the subset $G \subset S$ that could be measured to within 10% of actual post values by simulating the measurement process on idealized post shapes produced directly from Equation 2.33 (Figure 5.11a). We found the 10% tolerance region by rasterizing these post models $x_{\text{model}} \in M \subset S$ at each resolution used in our study (Figure 5.11b). Post models (x_{model}) were produced across a large enough range of parameters that M spanned all of the measured values seen in the unfiltered GLAD post data.

Fitting posts of insufficient resolution produces inaccurate results.

Each rasterized post model was processed identically to actual nanocolumn image data, using the routines described in Section 5.2.4 to extract and fit its width profile and produce a measured post model, x_{measured} . This x_{measured} was then compared to the original x_{model} . If each of the measured parameters was within 10% of the model parameters, the point x_{measured} was marked as “good;” if not, the model was marked as “bad.” Figure 5.11c shows a slice through M for posts $1.3\ \mu\text{m}$ in height, generated at a resolution of $0.152\ \text{nm pixel}^{-1}$, and demonstrates the distribution of good and bad points. Note that while the mapping of M proceeded by generating x_{model} at regular intervals, the good and bad points in 5.11c have no periodic spacing.

The region dominated by good points defines G , the space of measured values that are within at least 10% of the actual values of an ideal post model. In general, a graduated boundary exists between the regions dominated by good and bad points. To segment the region G and define its boundary, a three-dimensional moving window filter (e.g. moving average) compared the ratio of good points to total points within the moving window, centered at regular intervals. This process produced a regular lattice of points $y \in M$, each with a corresponding ratio value. The ratio histogram was segmented using a minimum error algorithm, resulting in a threshold value just less than 1. Points y with a ratio value above the threshold value define the region G , shaded in Figure 5.11c. As seen in Figure 5.11c, the window size used by the moving filter produces a conservative estimate of G , as a considerable number of good points are found outside the shaded region. To filter the actual GLAD post data, the fitting parameters for each measured GLAD post were compared to the points y . If the closest point y was within G ($y \in G$), the fitting

If ideal post measurements were inaccurate, real data was also likely inaccurate.

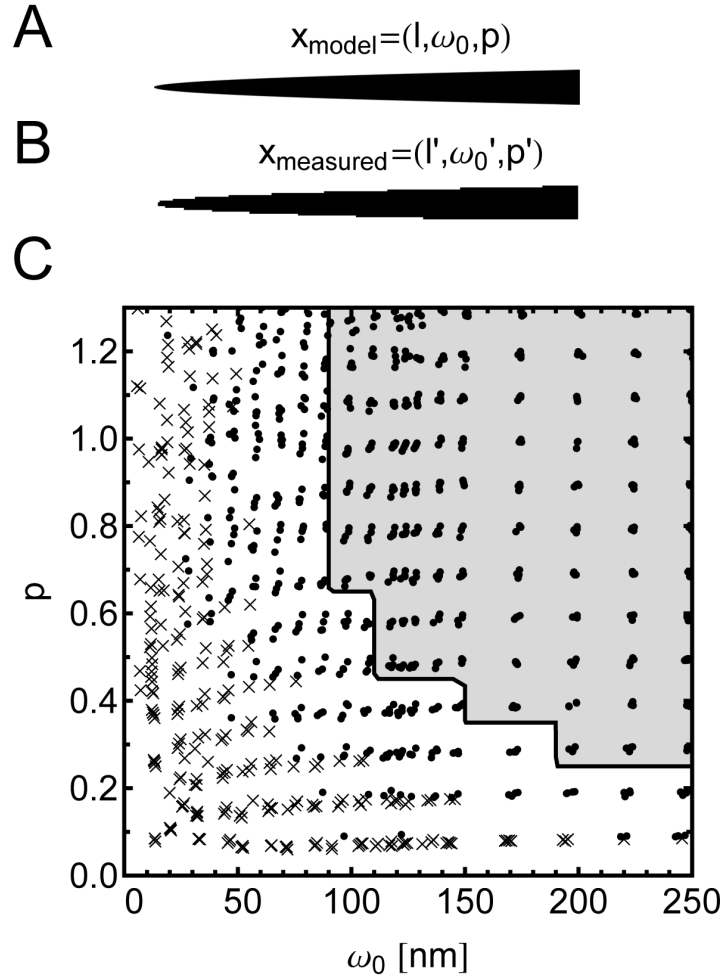


Figure 5.11: Schematic of the error analysis method used to ensure that measured post parameters are within at least 10% of ideal post parameters when ideal post shapes are rasterized and measured. Ideal post models $x_{\text{model}} \in M \subset S$ (A) are rasterized at the SEM resolutions to produce a measured profile. We then fit the power law to this measured profile, extracting a measured p and ω_0 to produce a measured model of the post x_{measured} (B). Comparison of x_{model} and x_{measured} across a range of parameters determines the percent difference of x_{measured} from x_{model} for each parameter. Points of x_{measured} that fall outside a 10% tolerance for any parameter are marked with a cross and those that fall within 10% tolerance for all parameters are marked with a circle in (C), which shows this analysis for a 0.152 nm/pixel resolution and posts with heights between 1.1 μm to 1.5 μm . The shaded region in (C) represents the region $G \subset M \subset S$ where no measured parameters stray outside the 10% tolerance. Only posts with measured parameters contained within G are kept for further analysis.

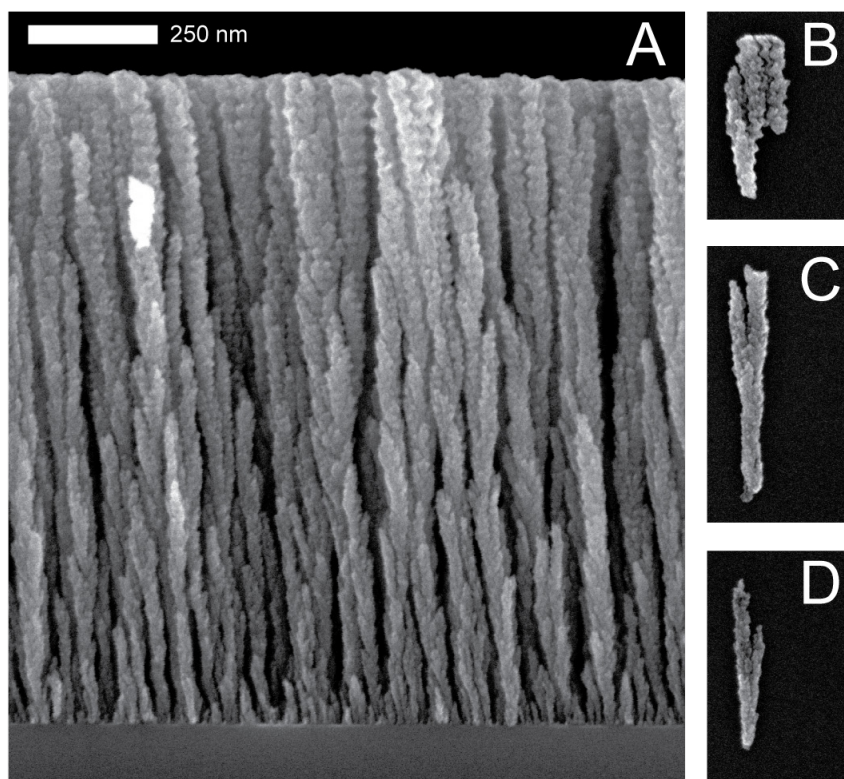


Figure 5.12: Vertical posts with graded pitch were used to determine if posts break during sonication. Film A is deposited at $\alpha = 81^\circ$ to a nominal thickness of 1500 nm, with pitch changing in even increments every 10 nm of growth from 45 nm pitch at the film base to 10 nm pitch at the top of the film. The fragments B-D appeared after treatment of film A, indicating that some post candidates emerge as fragments from the top region of the film.

parameters for that post were kept for further analysis; if not, that post was discarded.

5.3.2 Fragmentation

Perhaps the most obvious hurdle in this disassembly technique is the potential for nanocolumn breakage during sonication. To more conclusively test for fragmentation, I disassembled the unique morphologies described in Section 3.3.1, with graduated pitch along the post length. The full-length posts had markedly different morphologies at their tips, enabling identification of broken posts and determination of fragment origin.

The results shown in Figure 5.12 indicate that posts do break along their length. Treatment of films with increasing and with decreasing pitch produced similar results, producing fragments from both the upper and lower regions of the original film. This suggests that ob-

Some columns did fragment during sonication.

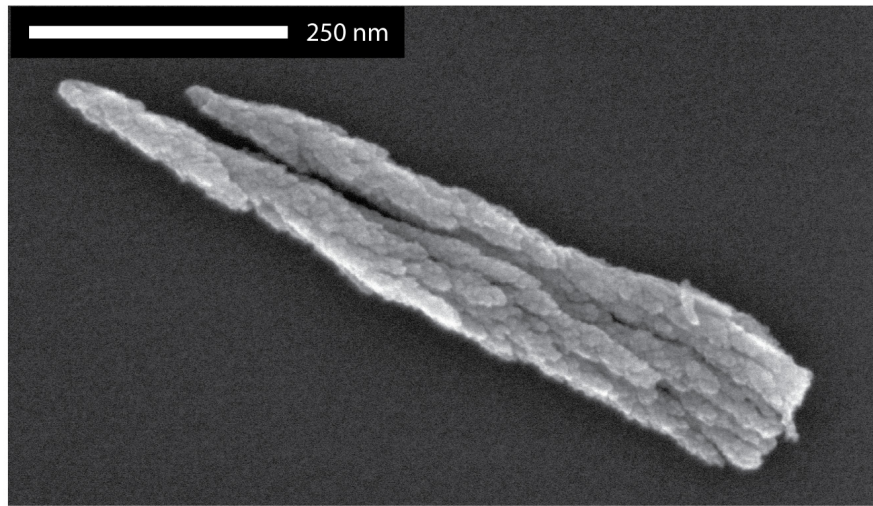


Figure 5.13: Two fragments from a $\alpha = 81^\circ$ TiO_2 film grown to 1 nm pitch that appear to have originated from the film top, still joined in their initial film configuration. Both have tapering bottoms reminiscent of the morphology of individual posts near the substrate, suggesting that fragments may be difficult to identify.

jects isolated from vertical post samples contain fragments of larger posts in addition to complete and extinct posts. Though some such fragments display obvious breaks across their width and can be manually excluded from analysis, many branches seem to recapitulate near-substrate post broadening, as demonstrated in Figure 5.13. Such branches breaking at their root would be more difficult to identify, casting doubt as to the origin of all measured objects shorter than the full film height. To avoid this uncertainty, the analysis below focuses on posts with length near the full film height.

5.4 ANALYSIS

Our technique isolated objects from throughout each processed film, and compiling the ω_0 and p parameters extracted from each object provided insight into overall film characteristics. This is demonstrated in Figure 5.14a with 112 objects from a 1 nm pitch sample, each satisfying the criteria outlined in Section 5.3.1. All examined films possessed a distinct “full-height” cluster of objects, shown boxed in Fig. 5.14a. Mean cluster lengths were between 8 nm and 140 nm below the thickness of the original film, as measured by cross-sectional SEM.

Shorter objects included both the apparent fragments demonstrated in Fig. 5.12a and the extinct posts with tapering profiles demonstrated in Fig. 5.14b-e. Due to the initiation of the extinction process, the broadening profiles of these hand-selected extinct cases only fit a power law profile for a portion of their lengths; initial examination did not find consistent power law behaviour within the “tail” region

Analysing unbroken “full-height” post cluster mitigates fragmentation.

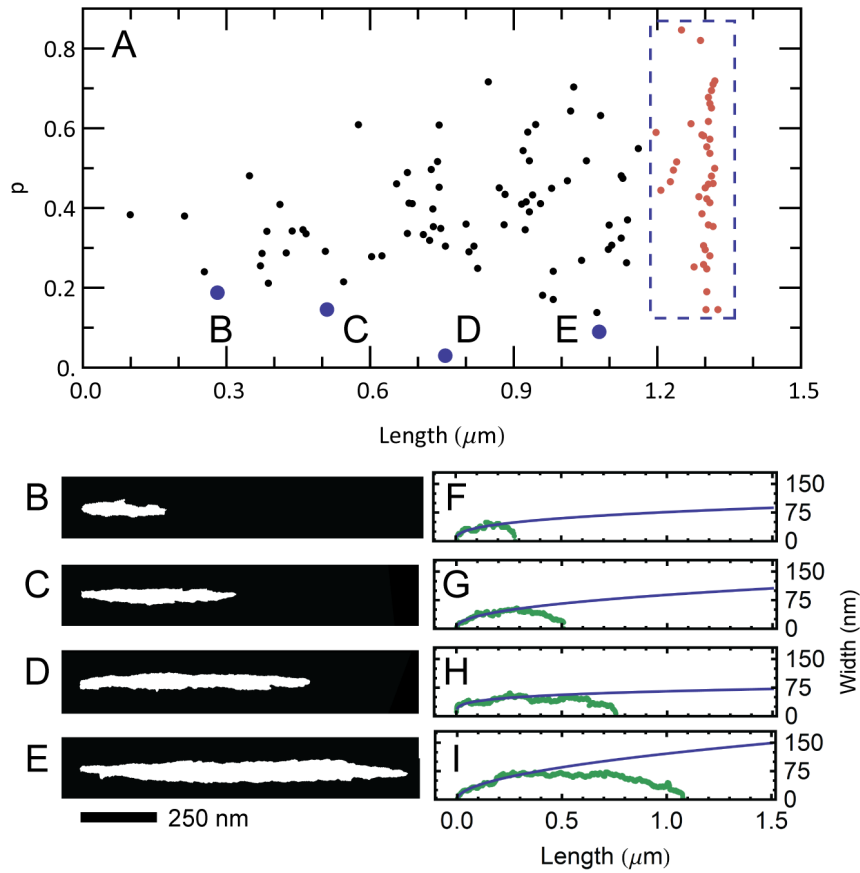


Figure 5.14: We fit the power law along the entire length of each measured object, aggregating the parameters to characterize the film. The above represents a single TiO_2 ($\alpha = 81^\circ$) GLAD film. Note the right-hand cluster (red) of objects, which we take to represent post suffering minimal fragmentation—these are used to calculate pitch-dependent film properties, avoiding errors introduced by fragmentation. We believe that ω_0 and p parameters calculated for objects below this cluster do not accurately reflect their morphologies. Highlighted are four hand-selected examples of tapering posts in this sub-height regime, some of which are also rejected on resolution-limit grounds. These appear to fit a power law for a portion of their length, but then diverge. As a naïve power law fit along their entire length yields parameters that do not describe this initial broadening phase, a more appropriate fitting model appears necessary for rigorous film characterization.

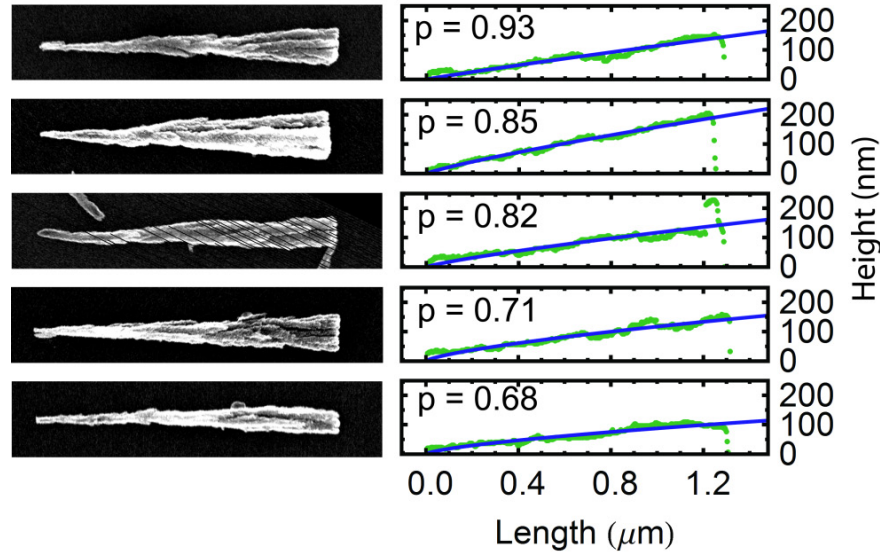


Figure 5.15: Examples of individual posts from a 1 nm pitch TiO_2 ($\alpha = 81^\circ$) film that lie outside the predicted theoretical KPZ limit. Comparison between SEM images and extracted width profiles indicates that these exceptions cannot easily be explained as poor analysis by the extraction algorithms.

produced by extinction. Because of these tapering profiles, fits such as those shown in Fig. 5.6 e-i produced ω_0 and p values that did not accurately characterize the objects' growth-scaling behaviour. Many of these inaccurate fits were excluded based on the criteria outlined in Section 5.3.1, and we inspected each surviving datum by hand to remove the remaining poor fits.

5.4.1 Evaluation of theoretical limits

The method successfully isolated 453 “full height” posts and 10,303 extinct posts and fragments. Of these, we rejected all but 97 “full-height” posts and 177 shorter posts based on the resolution considerations of Section 5.3.1 and a subsequent manual inspection of fit data. Based on the discussion in Section 5.3.2, we restricted further analysis to the “full-height” clusters of objects in films of different pitches, avoiding the influence of fragmentation and extinction. This produced distributions of p , and we discovered posts above the KPZ limit proposed by Karabacak *et al.* at each pitch. Examples of these limit breakers are provided in Figure 5.15 for a 1 nm pitch film, along with their fits and width profiles. The resolution issues discussed in Section 5.3.1 prevented similar testing of the MH limit in a statistically significant manner.

Figure 5.16 shows the arithmetic mean p and mean ω_0 of the objects in full height clusters of different pitches. The ω_0 parameter did

We rejected most of the dataset; future optimization may recover more.

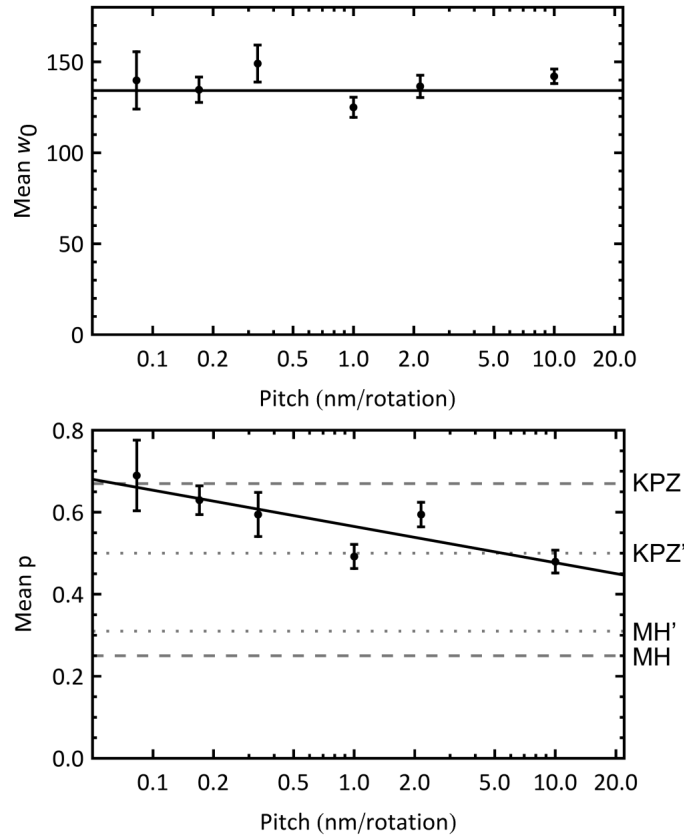


Figure 5.16: The arithmetic mean of p for full-height posts, plotted as a function of deposition pitch for the case of TiO_2 ($\alpha = 81^\circ$) rotating-substrate films. As expected, there is no significant relationship between the material constant w_0 and pitch. The exponent p , however, was found to vary as $p = 0.57 - 0.09 \log_{10} \cdot \text{pitch}$ with a high degree of statistical significance (correlation significance = 0.04). Ninety-five percent confidence intervals are $[0.51, 0.62]$ and $[-0.17, -0.01]$ for the two factors, respectively. Shown are the theoretical upper (KPZ) and lower (MH) limits for a stationary-substrate, along with the rotating-substrate modifications proposed by Karabacak *et al.* (KPZ' and MH') [71].

not depend on pitch (correlation significance is 0.94 [139]) and averaged 138 ± 4 nm (standard error) across all analysed films, with mean ω_0 varying by less than 20 nm across all samples. The p parameter exhibited a significant relationship (correlation significance = 0.04) with pitch in the form

$$p = 0.57 - 0.09 \log_{10} \frac{\text{pitch}}{\text{nm}} \quad (5.1)$$

where pitch is the film growth in nm per substrate rotation. The fitted slope had a standard error of 0.029. Thus, with increasing deposition pitch, films exhibited reduced broadening. Mean p values at pitches lower than 1 nm remained above the modified KPZ maximum proposed by Karabacak *et al.* None of the mean values lay above the unmodified upper KPZ limit—the scaling exponent of ξ_{\perp}^* alone—of $2/3$.

Column broadening depends on deposition pitch.

Both single posts and entire films violate proposed limits.

5.5 DISCUSSION

The method reported in this chapter successfully measured more individual post width profiles than all previous GLAD growth scaling literature, though we used only a portion to uncover the trend in pitch. Measured p distributions (Figure 5.14) indicate that $\alpha = 81^\circ$ titania posts break the KPZ limit proposed by Karabacak *et al.* [71] both individually and in aggregate. Manual inspection of the limit-breakers shown in Figure 5.15 indicates that they cannot be explained by poor fitting or as by-products of the dispersion process. Though not discussed in [71], the highly branching nature of the oxide film may explain this result. Pelliccione *et al.* suggest that the average spacing of GLAD film columns, as it is based on non-local shadowing phenomenon, does not display self-affinity and scales independently of column width scaling [140]. If this is the case, it is conceivable these non-local effects could provide an individual column with enough flux that its growth outpaces the growth of the correlation length, causing separate branches to arise from uncorrelated regions within each post. Though these individual branches may still broaden within the predicted limits, increased branching with height could inflate the p of the overall column. Alternatively, the simple geometric average of ξ_{\perp}^* and ξ_{\parallel}^* used in limits' derivations may fail to accurately capture the underlying growth mechanisms during constant rotation. These results highlight the need for further theoretical consideration of vertical post growth scaling.

Current theory does not fully explain observed growth scaling.

In light of the anomalous scaling discovered by Mukherjee *et al.* [78], the effect of temperature on these results must also be considered. Unpublished thermocouple measurements⁵ suggest that sub-

⁵ These measurements were performed by Graham Hunt in a study on heating and nucleation. A TiO_2 film was grown to 500 nm thickness, with temperature mea-

Table 5.1: Data from Figure 5.16, describing the “full-height” posts used in final analysis of p .

Nominal pitch (nm)	p		Column count
	Mean	St. Dev.	
10.0	0.48	0.11	17
2.15	0.59	0.12	15
1.00	0.49	0.19	41
0.33	0.59	0.19	12
0.17	0.63	0.09	7
0.08	0.69	0.19	5

strate temperatures increase during TiO_2 deposition. Assuming oxides express similar temperature behaviour to the metals studied by Mukherjee *et al.*, it is possible the upper regions of the film approach the critical 0.23 T_m threshold of $\sim 212^\circ\text{C}$. This is further complicated by the under-oxidation of the deposited titania. The observed vapour species in TiO_2 evaporations are, in order of decreasing frequency, TiO , Ti , TiO_2 , and O_2 [99]. Of these, Ti has the lowest melting point, with 0.23 $T_m = 173^\circ\text{C}$. The presence of oxygen is predicted to limit surface diffusion in growing films [7], potentially counteracting increased diffusion caused by temperature. Without extending the methods of Mukherjee *et al.* to the TiO_2 material system and locating a similar discontinuity temperature, it is difficult to confidently estimate the role of temperature in the broadening of these films. As all films were grown under identical temperature conditions to the same height, however, the observed trend in pitch may be unaffected.

The ω_0 parameter has been proposed as a material-dependent constant [33], and this is supported by the results presented here. Though individual posts within each film demonstrated significant scatter, ω_0 did not demonstrate any meaningful pitch dependence. In contrast, the correlation between p and pitch suggests that vertical post film morphology is influenced by the substrate’s rotation rate during deposition, in addition to the adatom energy at the film growth front. Previous theoretical work by Karabacak *et al.* [71] suggests that the p constant of a film is influenced by the relative importance of competing ballistic shadowing and surface diffusion effects. In this study, deposition flux and growth front temperature remain unchanged, and it

High temperature may contribute to high observed pitches.

Understanding pitch dependence provides new control over nanostructure morphology.

surements every 50 nm and an initial substrate temperature of $\sim 50^\circ\text{C}$. Maximum temperature was just under 150°C , though temperature increase had slowed to approximately 3° per 50 nm of film growth at 350 nm. Numerous unknowns, including the degree of contact with the substrate underneath, the relative emissivities of the thermocouple and the substrate, and the influence of the thermocouple shape and heat capacity on heat transfer all make this at best an approximation of the actual growth front temperature.

is unclear that pitch impacts the adatom diffusion. Rather, the radial averaging produced by low pitches may diminish the effect of stochastic shadowing within the film. A more even growth front would thus reduce extinction, in turn suppressing column broadening. Future studies manipulating both pitch and temperature may be better able to decouple these two possible influences on growth scaling.

5.5.1 Comparison of measurement techniques

Two slightly different methods of defining p for GLAD films exist in literature. Cross-sectional and top-down SEM techniques calculate average column width at several heights, then fit these points to the standard power law and extract a value for p . Taschuk *et al.*, for instance, measured column widths at heights of 250 nm, 500 nm, 750 nm, 1000 nm, and 1250 nm above the substrate from cross-sectional SEMs [33]. The analysis described here, along with that of Krause *et al.* [77] and Main *et al.* [73], instead estimates the p exponent for individual columns and averages these to produce p for the overall film⁶.

Average column p is not equivalent to overall film p .

The above research suggests that GLAD films are composed of nanocolumns with a wide distribution of p values. The most populous dataset (1 nm pitch in Table 5.1), for instance, has a standard deviation of ~ 0.2 on a mean p of ~ 0.5 . Given this variability, the two definitions are not necessarily equivalent. Echoing the discussion of area vs. diameter in Section 4.3.1, power law non-linearity allows the widths of columns on the tails of the p distribution to contribute disproportionately to measured width means.

Having ω_0 and p parameters of each measured post in the 1 nm pitch dataset allowed me to roughly gauge the difference between the two approaches. From each measured p and ω_0 pair, I calculated the expected post width at all the heights used by Taschuk *et al.* Averaging these widths across all the posts in the dataset, then fitting them to the power law, I could approximate the study of the same posts using the cross-sectional technique. Figure 5.17 shows the discrepancy between the two analyses: the cross-sectional simulation produces a 7% decrease in p . All other samples, based on smaller datasets, exhibit smaller discrepancies.

Methods return similar values for this sample.

More generally, the equivalence of the methods depends on the distributions of p and ω_0 in the film. The 1 nm pitch data is approximately normal, as demonstrated in Figure 5.18, with all samples passing an Anderson-Darling test of normality at the 0.05 level [142].

⁶ Note that with complete width profile data from numerous columns, as provided by the disassembly technique of this chapter, either method of analysis can be employed. Aligning the tops of columns with an independent cross-sectional measurement of film height could eliminate the uncertainty caused by the distribution of posts lengths within the “full-height” cluster, allowing calculation of the average column width throughout the film.

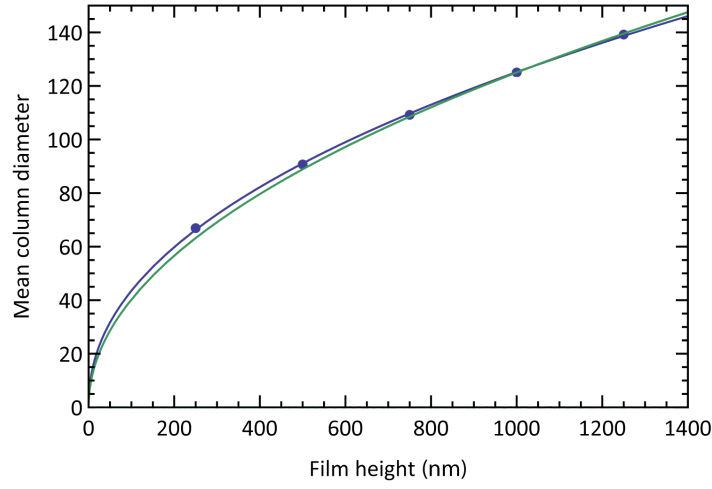


Figure 5.17: Comparison of two methods of analysing p . In this chapter, I measure p and ω_0 for 41 individual “full-height” posts from a 1 nm pitch $\alpha = 81^\circ$ TiO_2 film. Averaging these values produces the net p and ω_0 of the overall film, which describe the curve traced in green. To compare with cross-sectional and top-down methods of analysis, I can also use the p and ω_0 values of each column to approximate that column’s width at any height within the film. Averaging the calculated widths of all 41 columns produces the values shown in blue, evaluated at the heights measured in the work of Taschuk *et al.*. I then fit these average widths to the power law, producing the blue curve. While ω_0 is essentially unchanged, p decreases by 7%, reflecting the inequality of two definitions of p .

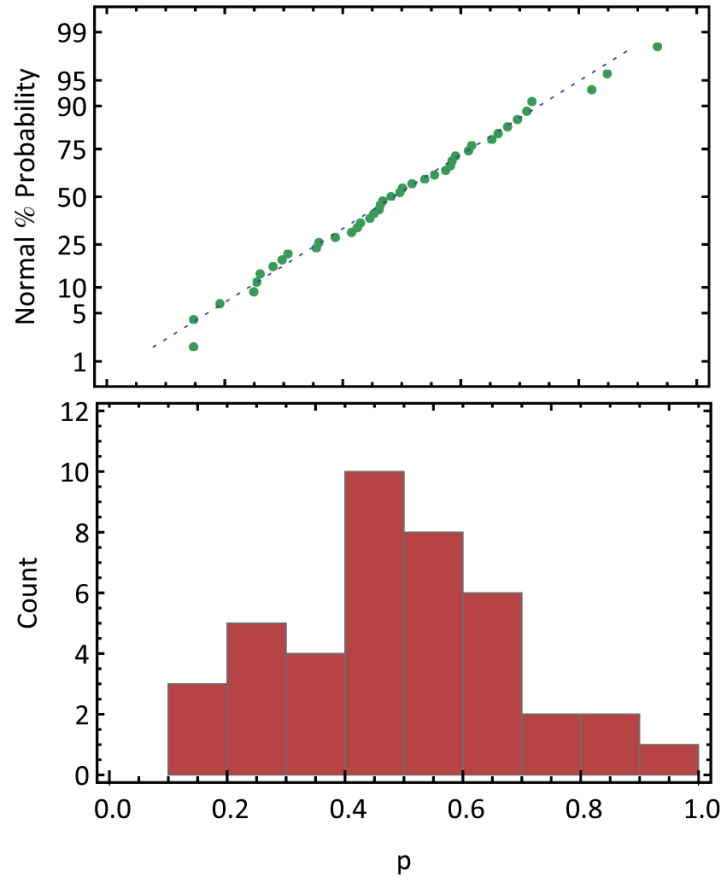


Figure 5.18: A normal probability plot (a) and histogram (b) of the p values recovered from the most populous “full-height” dataset in this thesis—an $\alpha = 81^\circ$ TiO_2 film deposited at 1 nm pitch. In a normal probability plot, the y-axis scaled such that a perfectly Gaussian dataset will produce a straight line. The linearity of the p values on this chart provides an effective qualitative confirmation that the data is approximately normal [141].

More data is required to fully understand the p distribution, however, providing a possible motivation for future work.

5.5.2 Potential improvements

Post fragmentation represents a significant obstacle to analysis, and restricted analysis in this initial trial to a small “full-height” portion of the data. Though the extinct post broadening profiles collected in this work appear consistent with FIB data [77], fragmentation prevents certainty as to the provenance of the shorter posts isolated by our method. While posts breaking across their width (normal to the growth direction) are easily identifiable, branches breaking off at their base may appear morphologically similar to extinct posts. Automated separation of extinct posts from these fragments has proved challenging, in part due to the difficulty of correctly determining the original orientation of a small object within the film. Adjusting sonication parameters may minimize fragmentation to negligible levels. Though time did not permit inclusion in this thesis, fragmentation could be quantified by depositing a dissimilar material on a vertical post film, then disassembling the film and analysing the length distribution of posts whose tips are tagged with the material. Tagged posts dramatically shorter than the film height thus indicate the presence of fragmentation.

Minimizing fragmentation could facilitate study of post extinction.

Resolution limits also significantly reduced the number of samples that could be reliably analysed, though the analysis supplied in Section 5.3.1 applies equally to all techniques that rely on SEM width profiles for measurement of p . The estimate of the 10% tolerance used here is conservative, and this restriction could likely be loosened with minimal inclusion of suspect data. Further studies informed by the resolution limits calculated in this chapter will provide much more reliable insight into GLAD structures.

With these exclusions, the trends reported here rely on sample numbers similar to those produced by existing techniques. Development of empirical scaling laws for column broadening and statistically reliable testing of the KPZ and MH predictions have been hampered by insufficient sample sizes, especially for extinct posts within the film bulk. As the full-height objects analysed here only represent a minor fraction (4.4%) of all those measured, further refinements in the automated characterization of smaller objects could yield significant, high-throughput insight into the morphology of the individual posts making up the entire GLAD film.

5.6 CONCLUDING REMARKS

This chapter presents a new technique for the automated characterization of the growth scaling of GLAD films, isolating individual posts

and measuring their broadening profiles. Initial results indicate that proposed KPZ scaling limit does not apply to individual TiO_2 posts, suggesting that further refinements to vertical post scaling theory are necessary to fully capture post morphologies. Furthermore, though ω_0 displays no significant dependence on deposition pitch, p varies inversely with it. This suppression of column broadening indicates that titania film morphology can be reliably influenced by substrate rotation within the vertical post regime.

Further refinements in sonication and automated image analysis may reduce the impact of fragmentation, permitting large-scale automated analysis of the characteristics of both extinct and full-height posts, and potentially shedding light on subtle growth trends. We expect optimization of sonication and spin-coating parameters to improve both post isolation the method's repeatability. Combining these improvements may yield an increase in sample numbers, permitting detection of subtle growth scaling trends within the data and ultimately leading to an improved understanding of GLAD growth dynamics, and thus improved control over GLAD architecture. Finally, greater control over nanocolumn broadening may allow further optimization of GLAD films, enhancing performance in their ultimate applications.

CONCLUSIONS

This thesis set out to contribute to our understanding of the growth scaling of vertical posts, working to explain the factors contributing to the existing scatter in reported literature values of p . This was accomplished first with a novel disassembly technique for the analysis of GLAD growth scaling that eliminates subjectivity in measurement. Utilizing this technique on heavily branching TiO_2 $\alpha = 81^\circ$ vertical posts, I performed the first quantitative analysis of the effect of deposition pitch on p , uncovering a statistically significant relationship:

$$p = 0.57 - 0.09 \log_{10} \frac{\text{pitch}}{\text{nm}} \quad (6.1)$$

with 95% confidence intervals of [0.51, 0.62] and [-0.17, -0.01] for the two factors, respectively. The theoretically material-dependent constant ω_0 showed no significant relationship with pitch.

6.1 INITIAL GROWTH SCALING MEASUREMENTS

In CHAPTER 4 I extracted p and ω_0 using three separate techniques previously reported in literature, summarized in Table 4.2

- A. **MANUAL WIDTH MEASUREMENTS** taken from cross-sectional SEMs, the most common technique used in GLAD scaling literature. Pitch values did not agree with TiO_2 literature values reported by Taschuk *et al.*, despite taking a greater number of measurements per film to reduce noise.
- B. **AUTOMATED DIAMETER MEASUREMENTS** taken from top-down SEMs. The technique was shown to be heavily dependent on the image analysis process used, and p results were neither self-consistent nor consistent with the other techniques employed.
- C. **MANUAL COUNTS** taken from top-down SEMs. Upper and lower boundaries were estimated for manual counts of posts, highlighting the degree of subjectivity inherent in scaling measurements from top-down images.

Existing techniques are ill-suited to branching films.

Though all three methods could have been further optimized, all suffered from the same drawback: the complex branching and merging morphology of TiO_2 films makes visual segmentation of individual columns extremely difficult, both from top-down and cross-sectional SEMs. This may be a major contributing factor to scatter in scaling measurements in oxide films.

6.2 DISASSEMBLY TECHNIQUE

Spurred by the difficulty in reliably measuring p in TiO_2 films, I proposed a new method for measuring broadening profiles that eliminates the need for subjective visual segregation, physically scattering posts across the substrate. As posts were shown to fragment, only posts with lengths near the full height of the film were used in analysis. Further, posts that did not meet stringent resolution criteria were discarded. The final dataset consisted of the full broadening profiles of 97 full-height posts.

I suspect that optimized versions of this technique will be able to significantly increase the percentage of usable data, as discussed below. The data measured here may be affected by the anomalous temperature scaling identified by Mukherjee *et al.* [78], as substrate temperatures increased during deposition. Further, branches breaking off the sides of full-height columns may have contributed to error in p measurement, though the consistency in ω_0 suggests this effect could not have varied too significantly from sample to sample.

As reported above, the disassembly technique demonstrated decreasing p with increasing pitch.

Method improvements may increase the percentage of usable data.

6.3 FUTURE WORK

The disassembly technique presented here is functional and produces a statistically significant set of data. The parameters described in this thesis represent the method in its infancy; crude optimization aimed at functional rather than optimal. Future optimization has great potential to further extend the method.

An immediate goal is reducing the amount of discarded data. The resolution limits discussed in Section 5.3.1 will provide guidance in avoiding sub-resolution imaging, applicable to all SEM-based measurement techniques. Further steps toward this end would focus on tailoring sonication conditions. Fragmentation can be estimated, albeit crudely, by tagging posts with materials that provide high contrast under SEM, either at column bottoms or column tops. Growing films on a high-contrast seed layer could distinguish extinct posts from other fragments, though it would interfere with the initial nucleation of the film. Depositing high contrast material onto the tops of columns would allow estimation of the fragmentation extent through measurement of the ratio of tagged posts with length less than the full-height cluster. As an added benefit, distinguishing extinct posts from fragments would enable extinction studies, providing width profile data in bulk.

Tagging survivor posts provides a simple method of quantifying fragmentation.

More sophisticated image analysis might improve width-profile accuracy and measurement throughput, allowing data recovery from touching objects. Elimination of all manual steps, be it through a dras-

tic reduction in fragmentation or development of more sophisticated algorithms, remains an important part of increasing throughput. Finally, tailoring of solvents and spin times could improve dispersion quality, leading to more successful measurements per SEM image.

Improved image analysis could increase throughput.

Titania film temperature remains a potential confounding factor; finding the critical temperature for anomalous scaling in TiO_2 would provide a much clearer estimate as to the influence of surface diffusion in the TiO_2 post.

Lastly, extending the technique to new materials and morphologies may require basic adaptation of sonication intensity and solvent type.

6.4 SUMMARY

This thesis has provided new insights into the growth scaling of glancing angle deposited nanorods, which may contribute to improved understanding of GLAD growth dynamics, ultimately contributing to greater control over nanostructure architecture and device performance.

BIBLIOGRAPHY

- [1] Milton Ohring. *The materials science of thin films*. Academic Press, 1992. ISBN 012524990X. (Cited on pages [4](#), [5](#), [6](#), and [33](#).)
- [2] Donald M. Mattox. *Handbook of Physical Vapor Deposition (PVD) Processing*. William Andrew, Burlington, MA, 2 edition, 2010. ISBN 0815520379. (Cited on page [4](#).)
- [3] John E. Mahan. *Physical Vapor Deposition of Thin Films*. Wiley-Interscience, Toronto, Canada, 1st edition, 2000. ISBN 0471330019. (Cited on pages [4](#), [5](#), and [6](#).)
- [4] Stephen A. Campbell. *Fabrication Engineering at the Micro- and Nanoscale*. Oxford University Press, 2008. ISBN 9780195320176. (Cited on page [5](#).)
- [5] M. Faraday. The Bakerian Lecture: Experimental Relations of Gold (and Other Metals) to Light. *Philosophical Transactions of the Royal Society of London*, 147(0):145–181, January 1857. ISSN 0261-0523. doi: 10.1098/rstl.1857.0011. (Cited on page [5](#).)
- [6] Edward B. Graper. Evaporation characteristics of materials from an electron beam gun II. *Journal of Vacuum Science & Technology A: Vacuum, Surfaces, and Films*, 5(4):2718, July 1987. ISSN 07342101. doi: 10.1116/1.574727. (Cited on page [6](#).)
- [7] L. Abelmann and C. Lodder. Oblique evaporation and surface diffusion. *Thin Solid Films*, 305(1-2):1–21, August 1997. ISSN 00406090. doi: 10.1016/S0040-6090(97)00095-3. (Cited on pages [6](#), [23](#), and [87](#).)
- [8] C. Ratsch and J. A. Venables. Nucleation theory and the early stages of thin film growth. *Journal of Vacuum Science & Technology A: Vacuum, Surfaces, and Films*, 21(5):S96, 2003. ISSN 07342101. doi: 10.1116/1.1600454. (Cited on page [6](#).)
- [9] Matthew M. Hawkeye and Michael J. Brett. Glancing angle deposition: Fabrication, properties, and applications of micro- and nanostructured thin films. *Journal of Vacuum Science & Technology A: Vacuum, Surfaces, and Films*, 25(5):1317, 2007. ISSN 07342101. doi: 10.1116/1.2764082. (Cited on pages [6](#), [7](#), [8](#), [9](#), and [11](#).)
- [10] King-Ning Tu, James W. Mayer, and Leonard C. Feldman. *Electronic Thin Film Science for Electrical Engineers and Materials Scientists*. Macmillan Publishing Company, first edition, 1992. (Cited on pages [6](#) and [7](#).)

- [11] M. Harsdorff. Heterogeneous nucleation and growth of thin films. *Thin Solid Films*, 90(1):1–14, April 1982. ISSN 00406090. doi: 10.1016/0040-6090(82)90061-X. (Cited on page 7.)
- [12] B. A. Movchan and A. V. Demchishin. Investigation of the structure and properties of thick vacuum- deposited films of nickel, titanium, tungsten, alumina and zirconium dioxide. *Fizika Metallov I Metallovedenie*, 28(4):653–660, 1969. (Cited on page 7.)
- [13] Peter M. Martin. *Handbook of Deposition Technologies for Films and Coatings: Science, Applications and Technology*. Elsevier, 2009. ISBN 081552031X. (Cited on pages 7 and 8.)
- [14] Akhlesh Lakhtakia and R. Messier. *Sculptured Thin Films: Nanoengineered Morphology And Optics*. SPIE Press, 2005. ISBN 0819456063. (Cited on page 8.)
- [15] John Jeremiah Steele. *Nanostructured thin films for humidity sensing*. PhD thesis, University of Alberta, 2007. (Cited on pages 8, 29, and 39.)
- [16] A. Kundt. Ueber Doppelbrechung des Lichtes in Metallschichten, welche durch Zerstäuben einer Kathode hergestellt sind. *Annalen der Physik und Chemie*, 263(1):59–71, 1886. ISSN 00033804. doi: 10.1002/andp.18862630103. (Cited on page 8.)
- [17] Felix Kaempf. Größe und Ursache der Doppelbrechung in Kundtschen Spiegeln und Erzeugung von Doppelbrechung in Metallspiegeln durch Zug. *Annalen der Physik*, 321(2):308–333, 1905. ISSN 00033804. doi: 10.1002/andp.19053210206.
- [18] Carl Bergholm. Über die Halbschattenmethode Braces um Phasendifferenzen zu messen. *Annalen der Physik*, 349(15):1053–1066, 1914. ISSN 00033804. doi: 10.1002/andp.19143491505. (Cited on page 8.)
- [19] H. König and G. Helwig. Über die Struktur schräg aufgedampfter Schichten und ihr Einfluß auf die Entwicklung submikroskopischer Oberflächenrauigkeiten. *Optik*, 6(111), 1950. (Cited on page 8.)
- [20] Michael J. Taschuk, Matthew M. Hawkeye, and Michael J. Brett. Glancing Angle Deposition. In Peter M. Martin, editor, *Handbook of Deposition Technologies for Films and Coatings*. Elsevier, Oxford, UK, third edition, 2010. (Cited on pages 9, 11, 12, 13, and 20.)
- [21] Niels O. Young and Jakym Kowal. Optically Active Fluorite Films. *Nature*, 183(4654):104–105, January 1959. ISSN 0028-0836. doi: 10.1038/183104a0. (Cited on page 8.)

- [22] J. M. Nieuwenhuizen and H. B. Haanstra. Microfractography of thin films. *Philips Technical Review*, 27(87), 1966. (Cited on page 8.)
- [23] Tomoyoshi Motohiro and Y. Taga. Thin film retardation plate by oblique deposition. *Applied Optics*, 28(13):2466, July 1989. ISSN 0003-6935. doi: 10.1364/AO.28.002466. (Cited on page 8.)
- [24] Paul Meakin, P. Ramanlal, L. Sander, and R. Ball. Ballistic deposition on surfaces. *Physical Review A*, 34(6):5091–5103, December 1986. ISSN 0556-2791. doi: 10.1103/PhysRevA.34.5091.
- [25] R.N. Tait, T. Smy, and M.J. Brett. Modelling and characterization of columnar growth in evaporated films. *Thin Solid Films*, 226(2):196–201, April 1993. ISSN 00406090. doi: 10.1016/0040-6090(93)90378-3. (Cited on pages 8 and 13.)
- [26] K. Robbie, L. J. Friedrich, S. K. Dew, T. Smy, and M. J. Brett. Fabrication of thin films with highly porous microstructures. *Journal of Vacuum Science & Technology A: Vacuum, Surfaces, and Films*, 13(3):1032, May 1995. ISSN 07342101. doi: 10.1116/1.579579. (Cited on page 8.)
- [27] K. Robbie, M. J. Brett, and A. Lakhtakia. Chiral sculptured thin films. *Nature*, 384(6610):616–616, December 1996. ISSN 0028-0836. doi: 10.1038/384616a0.
- [28] K. Robbie and M. J. Brett. Sculptured thin films and glancing angle deposition: Growth mechanics and applications. *Journal of Vacuum Science & Technology A: Vacuum, Surfaces, and Films*, 15(3):1460, May 1997. ISSN 07342101. doi: 10.1116/1.580562. (Cited on page 8.)
- [29] John J. Steele and Michael J. Brett. Nanostructure engineering in porous columnar thin films: recent advances. *Journal of Materials Science: Materials in Electronics*, 18(4):367–379, October 2006. ISSN 0957-4522. doi: 10.1007/s10854-006-9049-8. (Cited on page 9.)
- [30] Andy C. van Popta, Jeremy C. Sit, and Michael J. Brett. Optical properties of porous helical thin films and the effects of post-deposition annealing. In *Proceedings of SPIE 5464*, volume 5464, pages 198–208. SPIE, 2004. doi: 10.1117/12.545923. (Cited on page 10.)
- [31] P. C. P. Hrudely, K. L. Westra, and M. J. Brett. Highly Ordered Organic Alq₃ Chiral Luminescent Thin Films Fabricated by Glancing-Angle Deposition. *Advanced Materials*, 18(2):224–228, January 2006. ISSN 0935-9648. doi: 10.1002/adma.200501714. (Cited on page 9.)

- [32] Martin Brinkmann, Fabio Biscarini, Carlo Taliani, Iolinda Aiello, and Mauro Ghedini. Growth of mesoscopic correlated droplet patterns by high-vacuum sublimation. *Physical Review B*, 61(24):R16339–R16342, June 2000. ISSN 0163-1829. doi: 10.1103/PhysRevB.61.R16339. (Cited on page 9.)
- [33] M. T. Taschuk, K. M. Krause, J. J. Steele, M. A. Summers, and M. J. Brett. Growth scaling of metal oxide columnar thin films deposited by glancing angle depositions. *Journal of Vacuum Science and Technology B: Microelectronics and Nanometer Structures*, 27(5):2106, 2009. ISSN 10711023. doi: 10.1116/1.3196782. (Cited on pages 11, 24, 25, 26, 27, 29, 45, 47, 48, 59, 61, 63, 87, and 88.)
- [34] M.O. Jensen and M.J. Brett. Porosity engineering in glancing angle deposition thin films. *Applied Physics A*, 80(4):763–768, June 2004. ISSN 0947-8396. doi: 10.1007/s00339-004-2878-5. (Cited on pages 12 and 13.)
- [35] Mark Alan Summers. *Periodic Thin Films by Glancing Angle Deposition*. PhD thesis, University of Alberta, 2009. (Cited on pages 13 and 14.)
- [36] Douglas Gish. *Morphology control and localized surface plasmon resonance in glancing angle deposited films*. PhD thesis, University of Alberta, 2010. (Cited on pages 13 and 14.)
- [37] K. Robbie, C. Shafai, and M.J. Brett. Thin films with nanometer-scale pillar microstructure. *Journal of Materials Research*, 14(07):3158–3163, July 1999. ISSN 2044-5326. (Cited on page 14.)
- [38] Christian Patzig and Bernd Rauschenbach. Temperature effect on the glancing angle deposition of Si sculptured thin films. *Journal of Vacuum Science Technology A Vacuum Surfaces and Films*, 26(4):881, 2008. ISSN 07342101. doi: 10.1116/1.2834684. (Cited on page 14.)
- [39] D. Vick, M. J. Brett, and K. Westra. Porous thin films for the characterization of atomic force microscope tip morphology. *Thin Solid Films*, 408(1-2):79–86, April 2002. ISSN 00406090. doi: 10.1016/S0040-6090(02)00142-6. (Cited on page 15.)
- [40] William Jay Kiether. *Application of Sculptured Thin Film Technology to Metal Oxide Gas Sensors*. PhD thesis, NC State University, 2007. (Cited on page 15.)
- [41] Michael T. Taschuk, J. J. Steele, Andy C. van Popta, and Michael J. Brett. Photocatalytic regeneration of interdigitated capacitor relative humidity sensors fabricated by glancing angle deposition. *Sensors and Actuators B: Chemical*, 134(2):666–671, September 2008. ISSN 09254005. doi: 10.1016/j.snb.2008.06.009. (Cited on pages 27 and 29.)

- [42] John J. Steele, Michael T. Taschuk, and Michael J. Brett. Nanostructured Metal Oxide Thin Films for Humidity Sensors. *IEEE Sensors Journal*, 8(8):1422–1429, August 2008. ISSN 1530-437X. doi: 10.1109/JSEN.2008.920715. (Cited on pages 15, 28, and 29.)
- [43] Arman Bonakdarpour, M.D. Fleischauer, M.J. Brett, and J.R. Dahn. Columnar support structures for oxygen reduction electrocatalysts prepared by glancing angle deposition. *Applied Catalysis A: General*, 349(1-2):110–115, October 2008. ISSN 0926860X. doi: 10.1016/j.apcata.2008.07.015. (Cited on page 15.)
- [44] R. Figueroa, Tersio G. S. Cruz, and A. Gorenstein. WO₃ pillar-type and helical-type thin film structures to be used in microbatteries. *Journal of Power Sources*, 172(1):422–427, October 2007. ISSN 03787753. doi: 10.1016/j.jpowsour.2007.05.080. (Cited on page 15.)
- [45] M. D. Fleischauer. Columnar Thin Films for Three-Dimensional Microbatteries. *Journal of the Electrochemical Society*, 2009. (Cited on page 15.)
- [46] David A. Rider, Ryan T. Tucker, Brian J. Worfolk, Kathleen M. Krause, Abeed Lalany, Michael J. Brett, Jillian M. Buriak, and Kenneth D. Harris. Indium tin oxide nanopillar electrodes in polymer/fullerene solar cells. *Nanotechnology*, 22(8):085706, February 2011. ISSN 1361-6528. doi: 10.1088/0957-4484/22/8/085706. (Cited on page 15.)
- [47] M. J. Colgan and M. J. Brett. Field emission from carbon and silicon films with pillar microstructure. *Thin Solid Films*, 389(1-2):1–4, June 2001. ISSN 00406090. doi: 10.1016/S0040-6090(01)00892-6. (Cited on page 15.)
- [48] Louis W. Bezuidenhout, Neda Nazemifard, Abebaw B. Jemere, D. Jed Harrison, and Michael J. Brett. Microchannels filled with diverse micro- and nanostructures fabricated by glancing angle deposition. *Lab on a chip*, 11(9):1671–8, May 2011. ISSN 1473-0189. doi: 10.1039/colco0721h. (Cited on page 15.)
- [49] S. R. Jim, M. T. Taschuk, G. E. Morlock, L. W. Bezuidenhout, W. Schwack, and M. J. Brett. Engineered anisotropic microstructures for ultrathin-layer chromatography. *Analytical chemistry*, 82(12):5349–56, June 2010. ISSN 1520-6882. doi: 10.1021/ac101004b. (Cited on page 15.)
- [50] K. D. Harris, D. Vick, M. J. Brett, and K. Robbie. Improved Microstructures for Thermal Barrier Coatings Produced by Glancing Angle Deposition. *MRS Proceedings*, 555(-1), January 1998. (Cited on page 15.)

- [51] Kate Kaminska and Kevin Robbie. Birefringent omnidirectional reflector. *Applied Optics*, 43(7):1570, March 2004. ISSN 0003-6935. doi: 10.1364/AO.43.001570. (Cited on page 15.)
- [52] Zhifeng Huang, Kenneth D. Harris, and Michael J. Brett. Morphology Control of Nanotube Arrays. *Advanced Materials*, 21(29):2983–2987, August 2009. ISSN 09359648. doi: 10.1002/adma.200900269. (Cited on page 15.)
- [53] A. L. Barabási and H. E. Stanley. *Fractal concepts in surface growth*, volume 83. Cambridge University Press, 1995. ISBN 0521483182. doi: 10.1007/BF02179563. (Cited on pages 15, 16, 17, 19, and 20.)
- [54] Paul Meakin and Joachim Krug. Three-dimensional ballistic deposition at oblique incidence. *Physical Review A*, 46(6):3390–3399, September 1992. ISSN 1050-2947. doi: 10.1103/PhysRevA.46.3390. (Cited on pages 15, 21, and 22.)
- [55] Benoit B. Mandelbrot. *The Fractal Geometry of Nature*. W. H. Freeman and Company, San Francisco, 1983. (Cited on page 15.)
- [56] Harry Eugene Stanley. *Introduction to Phase Transitions and Critical Phenomena*. Oxford University Press, New York, 1971. (Cited on page 16.)
- [57] Benoit B. Mandelbrot. Self-Affine Fractals and Fractal Dimension. *Physica Scripta*, 32(4):257–260, October 1985. ISSN 0031-8949. doi: 10.1088/0031-8949/32/4/001. (Cited on page 16.)
- [58] F. Family. Scaling of rough surfaces: effects of surface diffusion. *Journal of Physics A: Mathematical and General*, 19(8):L441–L446, June 1986. ISSN 0305-4470. doi: 10.1088/0305-4470/19/8/006. (Cited on page 16.)
- [59] F. Family and T. Vicsek. Scaling of the active zone in the Eden process on percolation networks and the ballistic deposition model. *Journal of Physics A: Mathematical and General*, 18(2):L75–L81, February 1985. ISSN 0305-4470. doi: 10.1088/0305-4470/18/2/005. (Cited on page 16.)
- [60] S. F. Edwards and D. R. Wilkinson. The Surface Statistics of a Granular Aggregate. *Proceedings of the Royal Society A: Mathematical, Physical and Engineering Sciences*, 381(1780):17–31, May 1982. ISSN 1364-5021. doi: 10.1098/rspa.1982.0056. (Cited on page 19.)
- [61] Mehran Kardar, Giorgio Parisi, and Yi-Cheng Zhang. Dynamic Scaling of Growing Interfaces. *Physical Review Letters*, 56(9):889–892, March 1986. ISSN 0031-9007. doi: 10.1103/PhysRevLett.56.889. (Cited on page 19.)

- [62] K. Wilson and J. Kogut. The renormalization group and the ϵ expansion. *Physics Reports*, 12(2):75–199, August 1974. ISSN 03701573. doi: 10.1016/0370-1573(74)90023-4. (Cited on page 19.)
- [63] B. Delamotte. A hint of renormalization. page 17, December 2002. (Cited on page 19.)
- [64] Murray Eden. A two-dimensional growth process. In Jerzy Neyman, editor, *Proceedings of the Fourth Berkeley Symposium on Mathematical Statistics and Probability, Volume 4*, pages 223–239. University of California Press, 1961. (Cited on page 19.)
- [65] Jin Kim and S. Das Sarma. Discrete models for conserved growth equations. *Physical Review Letters*, 72(18):2903–2906, May 1994. ISSN 0031-9007. doi: 10.1103/PhysRevLett.72.2903. (Cited on pages 19 and 20.)
- [66] J. Villain. Continuum models of crystal growth from atomic beams with and without desorption. 1991. (Cited on page 20.)
- [67] V. K. Horvath, F. Family, and T. Vicsek. Dynamic scaling of the interface in two-phase viscous flows in porous media. *Journal of Physics A: Mathematical and General*, 24(1):L25–L29, January 1991. ISSN 0305-4470. doi: 10.1088/0305-4470/24/1/006. (Cited on page 21.)
- [68] Paul Meakin and Joachim Krug. Columnar microstructure in three-dimensional ballistic deposition. *Europhysics Letters (EPL)*, 11(1):7–12, 1990. (Cited on page 22.)
- [69] Douglas W. Vick. Self-shadowing and surface diffusion effects in obliquely deposited thin films. *Thin Solid Films*, 339(1-2):88–94, February 1999. ISSN 00406090. doi: 10.1016/S0040-6090(98)01154-7. (Cited on page 23.)
- [70] T. Smy, D. Walkey, K. D. Harris, and M. J. Brett. Thin film microstructure and thermal transport simulation using 3D-films. *Thin Solid Films*, 391(1):88–100, July 2001. ISSN 00406090. doi: 10.1016/S0040-6090(01)00974-9. (Cited on page 23.)
- [71] T. Karabacak, J. Singh, Y.-P. Zhao, G.-C. Wang, and T.-M. Lu. Scaling during shadowing growth of isolated nanocolumns. *Physical Review B*, 68(12), September 2003. ISSN 0163-1829. doi: 10.1103/PhysRevB.68.125408. (Cited on pages 23, 24, 63, 85, 86, and 87.)
- [72] T. Karabacak, G.-C. Wang, and T.-M. Lu. Physical self-assembly and the nucleation of three-dimensional nanostructures by

- oblique angle deposition. *Journal of Vacuum Science & Technology A: Vacuum, Surfaces, and Films*, 22(4):1778, July 2004. ISSN 07342101. doi: 10.1116/1.1743178. (Cited on page 24.)
- [73] E. Main. Continuum model for nanocolumn growth during oblique angle deposition. *Journal of Applied Physics*, 95(8):4346, 2004. ISSN 00218979. doi: 10.1063/1.1687033. (Cited on pages 24, 59, and 88.)
- [74] Kate Kaminska, Aram Amassian, Ludvik Martinu, and Kevin Robbie. Growth of vacuum evaporated ultraporous silicon studied with spectroscopic ellipsometry and scanning electron microscopy. *Journal of Applied Physics*, 97(1):013511, December 2005. ISSN 00218979. doi: 10.1063/1.1823029. (Cited on pages 24, 45, 51, 54, and 61.)
- [75] C. M. Zhou and D. Gall. Development of two-level porosity during glancing angle deposition. *Journal of Applied Physics*, 103(1):014307, January 2008. ISSN 00218979. doi: 10.1063/1.2828174. (Cited on page 27.)
- [76] Murat Cetinkaya, Niranjan Malvadkar, and Melik C. Demirel. Power-law scaling of structured poly(p-xylylene) films deposited by oblique angle. *Journal of Polymer Science Part B: Polymer Physics*, 46(6):640–648, March 2008. ISSN 08876266. doi: 10.1002/polb.21399. (Cited on page 24.)
- [77] Kathleen M. Krause, Douglas W. Vick, Marek Malac, and Michael J. Brett. Taking a Little off the Top: Nanorod Array Morphology and Growth Studied by Focused Ion Beam Tomography. *Langmuir : the ACS journal of surfaces and colloids*, 26(22):17558–67, November 2010. ISSN 1520-5827. doi: 10.1021/la103070x. (Cited on pages 24, 27, 29, 59, 62, 63, 88, and 91.)
- [78] S. Mukherjee and D. Gall. Power law scaling during physical vapor deposition under extreme shadowing conditions. *Journal of Applied Physics*, 107(8):084301, 2010. ISSN 00218979. doi: 10.1063/1.3385389. (Cited on pages 26, 65, 86, and 94.)
- [79] S. Mukherjee and D. Gall. Anomalous scaling during glancing angle deposition. *Applied Physics Letters*, 95(17):173106, October 2009. ISSN 00036951. doi: 10.1063/1.3257377. (Cited on pages 26 and 63.)
- [80] S. Mukherjee, C. M. Zhou, and D. Gall. Temperature-induced chaos during nanorod growth by physical vapor deposition. *Journal of Applied Physics*, 105(9):094318, May 2009. ISSN 00218979. doi: 10.1063/1.3116720. (Cited on pages 26 and 28.)

- [81] B. Dick, M. J. Brett, and T. Smy. Investigation of substrate rotation at glancing incidence on thin-film morphology. *Journal of Vacuum Science & Technology B: Microelectronics and Nanometer Structures*, 21(6):2569, November 2003. ISSN 0734211X. doi: 10.1116/1.1627334. (Cited on pages 26, 33, and 35.)
- [82] Gunter Buxbaum. *Industrial Inorganic Pigments*. John Wiley & Sons, 2 edition, 1998. ISBN 3527612106. (Cited on page 27.)
- [83] Kathleen Krause. *Characterization and modification of obliquely deposited nanostructures*. PhD thesis, University of Alberta, 2011. (Cited on page 39.)
- [84] Lance G. Phillips and David M. Barbano. The Influence of Fat Substitutes Based on Protein and Titanium Dioxide on the Sensory Properties of Lowfat Milks. *Journal of Dairy Science*, 80(11):2726–2731, November 1997. ISSN 00220302. doi: 10.3168/jds.S0022-0302(97)76234-9. (Cited on page 27.)
- [85] A. Jaroenworarluck, W. Sunsaneeyametha, N. Kosachan, and R. Stevens. Characteristics of silica-coated TiO₂ and its UV absorption for sunscreen cosmetic applications. *Surface and Interface Analysis*, 38(4):473–477, April 2006. ISSN 0142-2421. doi: 10.1002/sia.2313. (Cited on page 27.)
- [86] Donald Maxwell Brunette. *Titanium in Medicine: Material Science, Surface Science, Engineering, Biological Responses, and Medical Applications*. Springer, 2001. ISBN 3540669361. (Cited on page 27.)
- [87] Jing-Xiao Liu, Da-Zhi Yang, Fei Shi, and Ying-Ji Cai. Sol-gel deposited TiO₂ film on NiTi surgical alloy for biocompatibility improvement. *Thin Solid Films*, 429(1-2):225–230, April 2003. ISSN 00406090. doi: 10.1016/S0040-6090(03)00146-9. (Cited on page 27.)
- [88] Roberta Carbone, Ida Marangi, Andrea Zanardi, Luca Giorgetti, Elisabetta Chierici, Giuseppe Berlanda, Alessandro Podestà, Francesca Fiorentini, Gero Bongiorno, Paolo Piseri, Pier Giuseppe Pelicci, and Paolo Milani. Biocompatibility of cluster-assembled nanostructured TiO₂ with primary and cancer cells. *Biomaterials*, 27(17):3221–9, June 2006. ISSN 0142-9612. doi: 10.1016/j.biomaterials.2006.01.056. (Cited on page 27.)
- [89] Akira Fujishima, Tata N. Rao, and Donald A. Tryk. Titanium dioxide photocatalysis. *Journal of Photochemistry and Photobiology C: Photochemistry Reviews*, 1(1):1–21, June 2000. ISSN 13895567. doi: 10.1016/S1389-5567(00)00002-2. (Cited on pages 27 and 28.)

- [90] G. X. Shen, Y. C. Chen, and C. J. Lin. Corrosion protection of 316 L stainless steel by a TiO₂ nanoparticle coating prepared by sol-gel method. *Thin Solid Films*, 489(1-2):130–136, October 2005. ISSN 00406090. doi: 10.1016/j.tsf.2005.05.016.
- [91] Kristopher Page, Robert G. Palgrave, Ivan P. Parkin, Michael Wilson, Shelley L. P. Savin, and Alan V. Chadwick. Titania and silver-titania composite films on glass?potent antimicrobial coatings. *Journal of Materials Chemistry*, 17(1):95, 2007. ISSN 0959-9428. doi: 10.1039/b611740f. (Cited on page 27.)
- [92] K. Bange, C. R. Ottermann, O. Anderson, U. Jeschkowski, M. Laube, and R. Feile. Investigations of TiO₂ films deposited by different techniques. *Thin Solid Films*, 197(1-2):279–285, March 1991. ISSN 00406090. doi: 10.1016/0040-6090(91)90238-S. (Cited on page 28.)
- [93] S. Schiller, G. Beister, W. Sieber, G. Schirmer, and E. Hacker. Influence of deposition parameters on the optical and structural properties of TiO₂ films produced by reactive d.c. plasmatron sputtering. *Thin Solid Films*, 83(2):239–245, September 1981. ISSN 00406090. doi: 10.1016/0040-6090(81)90673-8. (Cited on page 28.)
- [94] M. J. Colgan, B. Djurfors, D.G. Ivey, and M. J. Brett. Effects of annealing on titanium dioxide structured films. *Thin Solid Films*, 466(1-2):92–96, November 2004. ISSN 00406090. doi: 10.1016/j.tsf.2004.02.019. (Cited on page 28.)
- [95] Jochen Winkler. *Titanium dioxide*. Vincentz Network GmbH & Co. KG, Hannover, Germany, 2003. ISBN 3878701489. (Cited on page 28.)
- [96] Hans K. Pulker. *Coatings on Glass*. Elsevier, 1999. ISBN 0444501037. (Cited on page 28.)
- [97] P. Lobl, M. Huppertz, and D. Mergel. Nucleation and growth in TiO₂ films prepared by sputtering and evaporation. *Thin Solid Films*, 251(1):72–79, October 1994. ISSN 00406090. doi: 10.1016/0040-6090(94)90843-5. (Cited on page 28.)
- [98] Andy C. van Popta, June Cheng, Jeremy C. Sit, and Michael J. Brett. Birefringence enhancement in annealed TiO₂ thin films. *Journal of Applied Physics*, 102(1):013517, 2007. ISSN 00218979. doi: 10.1063/1.2752132. (Cited on page 28.)
- [99] Leon I. Maissel and Reinhard Glang. *Handbook of Thin Film Technology*. McGraw-Hill, 1970. (Cited on pages 28 and 87.)
- [100] Tykhon Zubkov, Dirk Stahl, Tracy L Thompson, Dimitar Panayotov, Oliver Diwald, and John T Yates. Ultraviolet light-induced

- hydrophilicity effect on $\text{TiO}_2(110)(1 \times 1)$. Dominant role of the photooxidation of adsorbed hydrocarbons causing wetting by water droplets. *The journal of physical chemistry. B*, 109(32): 15454–62, August 2005. ISSN 1520-6106. doi: 10.1021/jp058101c. (Cited on pages 28 and 66.)
- [101] Hans W. Lehmann and K. Frick. Optimizing deposition parameters of electron beam evaporated TiO_2 films. *Applied Optics*, 27(23):4920, December 1988. ISSN 0003-6935. doi: 10.1364/AO.27.004920. (Cited on pages 28 and 31.)
- [102] D. Smetaniuk, M. T. Taschuk, and M. J. Brett. Photocatalytic Titanium Dioxide Nanostructures for Self-Regenerating Relative Humidity Sensors. *IEEE Sensors Journal*, (99):1–1, 2010. ISSN 1530-437X. doi: 10.1109/JSEN.2010.2095416. (Cited on pages 29 and 66.)
- [103] Daniel Patrick Smetaniuk. *Ultraviolet stabilization and performance enhancement of nanostructured humidity sensors*. PhD thesis, University of Alberta, 2012. (Cited on page 29.)
- [104] Hsiao-Yun Yang, Ming-Fu Lee, Chia-Hua Huang, Yu-Shi Lo, Yi-Jia Chen, and Ming-Show Wong. Glancing angle deposited titania films for dye-sensitized solar cells. *Thin Solid Films*, 518(5): 1590–1594, December 2009. ISSN 00406090. doi: 10.1016/j.tsf.2009.09.026. (Cited on page 29.)
- [105] Nathan J. Gerein, Michael D. Fleischauer, and Michael J. Brett. Effect of TiO_2 film porosity and thermal processing on TiO_2 -P3HT hybrid materials and photovoltaic device performance. *Solar Energy Materials and Solar Cells*, 94(12):2343–2350, December 2010. ISSN 09270248. doi: 10.1016/j.solmat.2010.08.010.
- [106] Ming-Show Wong, Ming-Fu Lee, Ching-Lun Chen, and Chia-Hua Huang. Vapor deposited sculptured nano-porous titania films by glancing angle deposition for efficiency enhancement in dye-sensitized solar cells. *Thin Solid Films*, 519(5):1717–1722, December 2010. ISSN 00406090. doi: 10.1016/j.tsf.2010.06.047.
- [107] G.K. Kiema, M.J. Colgan, and M.J. Brett. Dye sensitized solar cells incorporating obliquely deposited titanium oxide layers. *Solar Energy Materials and Solar Cells*, 85(3):321–331, January 2005. ISSN 09270248. doi: 10.1016/j.solmat.2004.05.001. (Cited on page 29.)
- [108] Matthew Martin Hawkeye. *Engineering optical nanomaterials using glancing angle deposition*. PhD thesis, University of Alberta, 2011. (Cited on pages 29 and 39.)

- [109] Yumei Zhu and Hongfei Jiao. Rugate filter with multi-channel grown by glancing angle deposition. *Optik - International Journal for Light and Electron Optics*, November 2011. ISSN 00304026. doi: 10.1016/j.ijleo.2011.09.012. (Cited on page 29.)
- [110] Kathleen M. Krause and Michael J. Brett. Spatially Graded Nanostructured Chiral Films as Tunable Circular Polarizers. *Advanced Functional Materials*, 18(20):3111–3118, October 2008. ISSN 1616301X. doi: 10.1002/adfm.200800685. (Cited on page 29.)
- [111] Kathleen M. Krause, Matthias Thommes, and Michael J. Brett. Pore analysis of obliquely deposited nanostructures by krypton gas adsorption at 87K. *Microporous and Mesoporous Materials*, 143(1):166–173, August 2011. ISSN 13871811. doi: 10.1016/j.micromeso.2011.02.023. (Cited on page 29.)
- [112] D. Vick, K. K. Krause, and M. J. Brett. Focused Ion Beam Tomography of Porous Titania Thin Films. *Microscopy and Microanalysis*, 15(S2):372–373, July 2009. ISSN 1435-8115. (Cited on page 29.)
- [113] Nicholas G. Wakefield and Jeremy C. Sit. On the uniformity of films fabricated by glancing angle deposition. *Journal of Applied Physics*, 109(8):084332, 2011. ISSN 00218979. doi: 10.1063/1.3559748. (Cited on pages 33, 35, and 43.)
- [114] C. Humble. Caveats regarding the use of control charts. *Infection control and hospital epidemiology : the official journal of the Society of Hospital Epidemiologists of America*, 19(11):865–8, November 1998. ISSN 0899-823X. (Cited on page 42.)
- [115] John C. Russ. *The Image Processing Handbook*. CRC Press, 5th edition, 2007. ISBN 0849372542. (Cited on pages 50, 51, 54, 57, and 76.)
- [116] Mehmet Sezgin and Bülent Sankur. Survey over image thresholding techniques and quantitative performance evaluation. *Journal of Electronic imaging*, 13(1):146–165, 2004. (Cited on pages 51 and 74.)
- [117] S. Ridler and T. W. Calvard. Picture Thresholding Using an Iterative Selection Method. *Ieee Transactions On Systems Man And Cybernetics*, 8(Aug):630–632, 1978. (Cited on page 51.)
- [118] Joshua LaForge, Grayson Ingram, Michael T. Taschuk, and Michael J. Brett. Flux engineering to control in-plane crystal and morphological orientation. *Crystal Growth & Design*, page 120528132039002, May 2012. ISSN 1528-7483. doi: 10.1021/cg300469s. (Cited on page 61.)

- [119] Cristina Buzea, Gisia Beydaghyan, Chelsea Elliott, and Kevin Robbie. Control of power law scaling in the growth of silicon nanocolumn pseudo-regular arrays deposited by glancing angle deposition. *Nanotechnology*, 16(10):1986–92, October 2005. ISSN 0957-4484. doi: 10.1088/0957-4484/16/10/002. (Cited on page 63.)
- [120] K. Gilbertson, W. Finlay, C. Lange, M. Brett, D. Vick, and Y. Cheng. Generation of fibrous aerosols from thin films. *Journal of Aerosol Science*, 36(7):933–937, July 2005. ISSN 00218502. doi: 10.1016/j.jaerosci.2004.10.010. (Cited on page 64.)
- [121] K. Gilbertson, W. Finlay, C. Lange, M. Brett, and D. Vick. Nanofabrication of High Aspect Ratio Aerosol Particles for Deposition Studies in a Model Human Airway. In *2004 International Conference on MEMS, NANO and Smart Systems (ICMENS'04)*, pages 268–270. IEEE. ISBN 0-7695-2189-4. doi: 10.1109/ICMENS.2004.1508958. (Cited on page 65.)
- [122] Thuy T. Chastek, Steven D. Hudson, and Vincent A. Hackley. Preparation and characterization of patchy particles. *Langmuir : the ACS journal of surfaces and colloids*, 24(24):13897–903, December 2008. ISSN 0743-7463. doi: 10.1021/la8017375. (Cited on page 65.)
- [123] Yuping He, Jinsong Wu, and Yiping Zhao. Designing catalytic nanomotors by dynamic shadowing growth. *Nano letters*, 7(5): 1369–75, May 2007. ISSN 1530-6984. doi: 10.1021/nl070461j. (Cited on page 65.)
- [124] J. G. Gibbs and Y.-P. Zhao. Design and characterization of rotational multicomponent catalytic nanomotors. *Small (Weinheim an der Bergstrasse, Germany)*, 5(20):2304–8, October 2009. ISSN 1613-6829. doi: 10.1002/smll.200900686. (Cited on page 65.)
- [125] A. L. Beaudry, R. T. Tucker, J. M. LaForge, M. T. Taschuk, and M. J. Brett. Indium tin oxide nanowhisker morphology control by vapour-liquid-solid glancing angle deposition. *Nanotechnology*, 23(10):105608, March 2012. ISSN 1361-6528. doi: 10.1088/0957-4484/23/10/105608. (Cited on page 65.)
- [126] Salih U. Bayca, Mehmet F. Cansizoglu, Alexandru S. Biris, Fumiya Watanabe, and Tansel Karabacak. Enhanced oxidation resistance of magnesium nanorods grown by glancing angle deposition. *International Journal of Hydrogen Energy*, 36(10):5998–6004, May 2011. ISSN 03603199. doi: 10.1016/j.ijhydene.2011.01.152.
- [127] Y.-P. Zhao, D.-X. Ye, G.-C. Wang, and T.-M. Lu. Designing nanostructures by glancing angle deposition. *Proc. SPIE*, 5219, 2003.

- [128] Yuping He, Junxue Fu, Yang Zhang, Yiping Zhao, Lijiao Zhang, Ailin Xia, and Jianwang Cai. Multilayered Si/Ni nanosprings and their magnetic properties. *Small (Weinheim an der Bergstrasse, Germany)*, 3(1):153–60, January 2007. ISSN 1613-6829. doi: 10.1002/smll.200600375.
- [129] Motofumi Suzuki, Kenji Hamachi, Hideki Hara, Kaoru Nakajima, Kenji Kimura, Chia-Wei Hsu, and Li-Jen Chou. Vapor-liquid-solid growth of Ge nanowhiskers enhanced by high-temperature glancing angle deposition. *Applied Physics Letters*, 99(22):223107, 2011. ISSN 00036951. doi: 10.1063/1.3664777. (Cited on page 65.)
- [130] Jeanne Ayache, Luc Beaunier, Jacqueline Boumendil, Gabrielle Ehret, and Danièle Laub. *Sample Preparation Handbook for Transmission Electron Microscopy: Methodology* (Google eBook). Springer, 2010. ISBN 0387981810. (Cited on page 65.)
- [131] T. I. Quickenden and J. A. Irvin. The ultraviolet absorption spectrum of liquid water. *The Journal of Chemical Physics*, 72(8):4416, 1980. ISSN 00219606. doi: 10.1063/1.439733. (Cited on page 66.)
- [132] B. Y. Sami Awad. Ultrasonic Cavitations and Precision Cleaning. *Precision Cleaning*, November 1996. (Cited on page 68.)
- [133] G. W. Gale and A. A. Busnaina. Removal of particulate contaminants using ultrasonics and megasonics: a review. *Particulate Science and Technology*, 13(3-4):197–211, July 1995. ISSN 0272-6351. doi: 10.1080/02726359508906678. (Cited on page 68.)
- [134] F. J. Fuchs. Ultrasonic cleaning: Fundamental theory and application. In *Precision Cleaning*, Rosemont, IL, 1995. (Cited on page 68.)
- [135] Leonid I. Rudin, Stanley Osher, and Emad Fatemi. Nonlinear total variation based noise removal algorithms. *Physica D: Nonlinear Phenomena*, 60(1-4):259–268, November 1992. ISSN 01672789. doi: 10.1016/0167-2789(92)90242-F. URL [http://dx.doi.org/10.1016/0167-2789\(92\)90242-F](http://dx.doi.org/10.1016/0167-2789(92)90242-F). (Cited on page 73.)
- [136] Alina N. Moga and Moncef Gabbouj. Parallel Marker-Based Image Segmentation with Watershed Transformation. *Journal of Parallel and Distributed Computing*, 51(1):27–45, May 1998. ISSN 07437315. doi: 10.1006/jpdc.1998.1448. (Cited on page 74.)
- [137] Frank Y. Shih. *Image Processing and Mathematical Morphology*. CRC Press, first edition, 2009. (Cited on page 74.)
- [138] Tony Chan and Luminita Vese. An Active Contour Model without Edges. In Mads Nielsen, Peter Johansen, Ole Fogh

Olsen, and Joachim Weickert, editors, *Scale-Space Theories in Computer Vision*, volume 1682 of *Lecture Notes in Computer Science*. Springer Berlin Heidelberg, Berlin, Heidelberg, 1999. ISBN 978-3-540-66498-7. doi: 10.1007/3-540-48236-9. (Cited on page 74.)

- [139] John R. Taylor. *An Introduction to Error Analysis*. University Science Books, second edition, 1997. (Cited on page 86.)
- [140] M. Pelliccione, T. Karabacak, and T.-M. Lu. Breakdown of Dynamic Scaling in Surface Growth under Shadowing. *Physical Review Letters*, 96(14), April 2006. ISSN 0031-9007. doi: 10.1103/PhysRevLett.96.146105. URL <http://prl.aps.org/abstract/PRL/v96/i14/e146105>. (Cited on page 86.)
- [141] Douglas C. Montgomery. *Design and Analysis of Experiments*. Wiley Inc., seventh edition, 2009. (Cited on page 90.)
- [142] Berna Yazici and Senay Yolacan. A comparison of various tests of normality. *Journal of Statistical Computation and Simulation*, 77(2):175–183, February 2007. ISSN 0094-9655. doi: 10.1080/10629360600678310. (Cited on page 88.)

APPENDIX: PROCEDURES

The below is the final, step-by-step procedure used for the disassembly of the GLAD films in Chapter 5. The below is not optimized; there are likely considerable improvements to be found in a more thorough study of the effects of various parameters, which include the sonication time and intensity, the concentration of isopropanol used, the spin speed, and the number of droplets applied.

A.1 DISASSEMBLY PROCEDURE

The equipment used includes a Tru-Sweep 575D benchtop ultrasonic cleaner (Crest Ultrasonics) and a WS-200 series resist spinner (Lau-rell, WS-200-8NPP/RTV), alongside an assortment of beakers and pipettes.

1. CLEAN 50 mL immersion beakers, one per sample
 - a) Scrub with Citranox and deionised water (DI)
 - b) Rinse with DI
 - c) Sonicate for 3 minutes in acetone (Power: 9)
 - d) Rinse with IPA and DI
 - e) Sonicate for 3 min in DI (Power: 9)
 - f) Rinse with DI and isopropanol IPA
 - g) Dry with basic N₂
2. CLEAN 2X medium process beakers
 - a) Scrub with citranox and DI
 - b) Rinse with DI and IPA
 - c) Dry with pressurized N₂
3. CLEAN spinning wafers
 - Use three tweezers, switch off to prevent tweezer-defects)
 - Sonicate a quarter wafer for every three eventual spins (Power: 9)
 - a) Invert a 50 mL beaker in a 500 mL beaker filled with acetone, propping wafers upright with polished side facing outward
 - b) Sonicate for three minutes—tweezer tips can be inserted in central beaker for cleaning

- c) Rinse with IPA
- d) Rinse with DI and IPA
- e) Dry with pressurized N₂
4. FILL beakers with 8 mL IPA via pipette
 - a) Pour stock IPA into first beaker
 - b) Clean out pipette with three fills of IPA, emptying into second beaker
5. MOVE sonic cleaner beside spinner
6. SONICATE samples for 80-90 minutes (Power: 9)
 - Use clean-room wipes to cover exposed liquid and prevent splashing/contamination
 - Record temperature before and after
7. SPIN samples @ 1250 RPM out of sonication—requires one disposable pipette per spin
 - Cover all but current beaker with clean-room wipes

APPENDIX: CODE

B.1 ROTATION STAGE EQUIVALENT GAMMA CALCULATIONS

The rotation stage used in this thesis has four individual sample mounts—one root shaft connected to the phi motor, and three additional stages with various gearing ratios. When the root shaft is rotated to a certain gamma, the other stages are spun a different amount. The below takes ratios from the rotation stage blueprint and searches through available root shaft rotations to find the angles at which the stage gammas are optimally separated.

In Section 2.2.3, I define gamma as the angle of substrate rotation from the effective growth direction during each half-period. Note that gamma is only defined from 0° to 90° . A rotation of 95° , for instance, is equivalent to a rotation of 85° , except during the transient period of actual rotation.

The below takes this into account, assigning each stage an effective gamma for each angle of root shaft rotation—I analyse rotations from 0° to degrees with a resolution of steps.

```

1 ratios = { 1, 3, 6, 12}; (* Physical gearing ratios of the
   stage *)
degrees = 360; (* Degrees over which analysis is performed *)
3 step = 0.01; (* Step size, in degrees, of analysis *)

5 gammas = Transpose[ Table[
   Abs[90*Mod[Quotient[root*ratios, 90], 2] - Mod[root*
   ratios, 90]],
7   {root, 0, degrees, step}
   ] ] // N;
9 (* gammas is now a list with a column for each root degree,
   and a row \
   for each stage. *)

11 (* Sort by angle, rather than stage number. *)
13 sgammas = gammas;
15 For[i = 1, i <= Dimensions[sgammas][[2]], i++,
   sgammas[[All, i]] =
   Sort[ gammas[[All, i]], Greater ]
17 ];

19 {ListLinePlot[gammas,
   Frame -> True,
21   FrameLabel -> {"Driveshaft Rotation (degrees)",
   "Effective Gamma (degrees)"},
   DataRange -> {0, degrees}},
23 ListLinePlot[sgammas,
25   Frame -> True,
```



```

27 FrameLabel -> {"Driveshaft Rotation (degrees)",
  "Effective Gamma (degrees)"},
  DataRange -> {0, degrees}}

```

B.1.1.1 Equivalent Gamma Optimization

Ideally, I want the space (in degrees) between each adjacent equivalent gamma to be equal. Furthermore, as $\gamma = 0^\circ$ and 90° are not interesting cases, I want this same space to be present between the lowest equivalent γ and 0° , as well as between the highest equivalent γ and 90° . Thus the ideal spacing is given by 90° over one more than the number of stages.

```

idealDiff = 90/5;
2 Dimensions[sgammas];
error[x_] := (
4   Module[{cols, spac, diff},
      cols = Append[Prepend[x, 90], 0]; (* Sandwiches x with
      {90,...,0} *)
6
      diff = Map[Subtract @@ # &, Partition[cols, 2, 1]];
8      diff = diff - idealDiff;
      diff = diff^2;
10     Total[diff]]
  )
12 totError = error /@ Transpose[sgammas];

```

Here I square error—the deviation at each stage from the ideal spacing—and examine several of the minimum values. It doesn't look like I need to look past 90° to find the optimum values, based on the above. Below is a quick function that finds the minimum between the degrees {a,b} entered, and outputs the root shaft rotation and the total error at that location.

```

minerr[x_] :=
2   Module[{start, stop, min},
      start = Round[x[[1]]/step];
4      stop = Round[x[[2]]/step];
      min = Min[totError[[start ;; stop]]];
6      {(Position[totError[[start ;; stop]], min][[1, 1]] + start)*
      step,
      min}
8   ]
10 mins = minerr /@ {{4, 7}, {10, 12}, {17.5, 20}, {24, 26}}

```

I now have the minimums in this format, and want to plot the values, possibly superimposed with the error plot above. `ListPlot` in *Mathematica* can handle multiple datasets, but if scatter-plot functionality is required, it needs to be in the form:

`ListPlot` [{{{ax₁, ay₁},{ax₂, ay₂},...},{bx₁, by₁},{bx₂, by₂},...}]

for the two datasets a and b, each with a number of coordinate pairs. This is accomplished by pulling together a 2xN list of the values, then transposing them to produce the desired coordinate pairs.

```
Transpose[{mins[[All, 1]],
  2      gammas[[#, Round[mins[[All, 1]]/step] ]]}] & /@ Range[4]
```

Figure export

The below function generates axis ticks, which in *Mathematica* are given as ordered triplets of the form (Location of tick on axis, Text label of tick, Tick length in printer's points).

The function takes:

- spacing - between major ticks, in the units of the plot
- subdivisions - how many parts that each major tick length is divided into
- majorTickLength - actual printed length on the page of the major ticks. Units unknown.
- {min, max} - the range over which you want the ticks to run, in the units of the plot. `nullTicker` is essentially the same, but outputs no label on the ticks (i.e.: for the top axis of the plot)

```
ticker[spacing_, subdivisions_, majorTickLength_, {min_, max_}
  ] :=
2 Module[
  {minorLength, subSpacing, roundMin, roundMax, majorTicks,
4   minorTicks, ticks},
  minorLength = majorTickLength/2; (*
6   Sets minor tick length as fraction of major length. *)
  subSpacing = spacing/subdivisions; (* Interval between minor
   ticks *)
8
  roundMin = Ceiling[min, subSpacing]; (*
10  Rounds boundary tick locations to fit tick spacings *)
  roundMax = Floor[max, subSpacing];
12  (* Styles label text,
   and generates ordered triplets at each i from min to max,
14  with appropriate spacing *)
  majorTicks =
16  Table[{i, i~Style~{"Calibri", 9}, {majorTickLength, 0}}, {i
    ,
```

```

    Ceiling[min, spacing], Floor[max, spacing], spacing]];
18  minorTicks =
    Table[{i, , {minorLength, 0}}, {i, Ceiling[min, subSpacing
    ],
20    Floor[max, subSpacing], subSpacing}];
    ticks = majorTicks~Join~minorTicks
22  ]
  nullTicker[spacing_, subdivisions_, majorTickLength_, {min_,
    max_}] :=
24  Module[
    {minorLength, subSpacing, roundMin, roundMax, majorTicks,
26    minorTicks, ticks},
    minorLength = majorTickLength/2; (*
28    Sets minor tick length as fraction of major length. *)
    subSpacing = spacing/subdivisions; (* Interval between minor
    ticks *)

30    roundMin = Ceiling[min, subSpacing]; (*
32    Rounds boundary tick locations to fit tick spacings *)
    roundMax = Floor[max, subSpacing];
34    (* Styles label text,
    and generates ordered triplets at each i from min to max,
36    with appropriate spacing *)
    majorTicks =
38    Table[{i, , {majorTickLength, 0}}, {i, Ceiling[min, spacing
    ],
    Floor[max, spacing], spacing}];
    minorTicks =
40    Table[{i, , {minorLength, 0}}, {i, Ceiling[min, subSpacing
    ],
42    Floor[max, subSpacing], subSpacing}];
    ticks = majorTicks~Join~minorTicks
44  ]

```

This modification is for the right side, where the labels are not the same as the tick locations. All inputs, save PLOTmin and PLOTmax, are in the units of the right axis, rather than the left axis.

```

rightTicker[spacing_, subdivisions_,
2  majorTickLength_, {plotMin_, plotMax_}, {min_, max_}] :=
    Module[
    {minorLength, subSpacing, roundMin, roundMax, majorTicks,
4    minorTicks, ticks, ratio},
    ratio = (plotMax - plotMin)/(max - min);
6    minorLength = majorTickLength/2; (*
    Sets minor tick length as fraction of major length. *)
8    subSpacing = spacing/subdivisions; (* Interval between minor
    ticks *)

10    roundMin = Ceiling[plotMin, subSpacing]; (*
    Rounds boundary tick locations to fit tick spacings *)
12    roundMax = Floor[plotMax, subSpacing];
    (* Styles label text,
14    and generates ordered triplets at each i from min to max,

```

```

with appropriate spacing *)
16 majorTicks =
    Table[{ratio*i, i~Style~{"Calibri", 9}, {majorTickLength,
18         o}}, {i,
        Ceiling[min, spacing], Floor[max, spacing], spacing}];
minorTicks =
20 Table[{ratio*i, , {minorLength, o}}, {i, Ceiling[min,
        subSpacing],
        Floor[max, subSpacing], subSpacing}];
22 ticks = majorTicks~Join~minorTicks
    ]

```

The actual plot is called, and the above function used to adjust the ticks on all four frames.

```

1 resolution = 300; (* In DPI. *)
physicalPlotWidth =
3 4; (* In inches. Columns in thesis are 4 inches wide. *)
leftRange = {0, 90}; (* Left Y axis minimum and maximum *)
5 rightRange = {0, 3000}; (* Right Y axis minimum and maximum *)
bottomRange = {0, 35}; (* X minimum and maximum *)
7 tickLength = 0.008;
productionImage = Show[
9  (** SELECTED GAMMAS PLOT **)
    ListPlot[Transpose[{
11         mins[[All, 1]],
        gammas[[#, Round[mins[[All, 1]]/step] ]]]
13     ] & /@ Range[4],
15  (* Basic plot parameters *)
    PlotRange -> {{0, 35}, {0, 90}},
17  PlotStyle -> PointSize[0.01],
    BaseStyle -> {FontSize -> 11},
19  ImageSize -> 72*physicalPlotWidth, (* Actually pixels,
        based on Mathematica's assumption of 72 ppi screen
        resolution *)
21  LabelStyle -> {FontFamily -> "Calibri"}, (*
        Remember to keep this consistent with the "ticker" function
        ! *)
23  (* Frame labeling *)
    Frame -> True,
25  FrameLabel -> {"Effective Gamma (degrees)",
        "Squared Error (arb. units)", {"Driveshaft Rotation (
        degrees)",
27         Null}},
    FrameTicksStyle -> AbsoluteThickness[1],
29  FrameStyle -> AbsoluteThickness[1],
    FrameTicks ->
31  { {ticker[20, 4, tickLength, leftRange],
        rightTicker[700, 7, tickLength, leftRange, {0, 3000}]
        },
33  {ticker[5, 5, tickLength, bottomRange],
        nullTicker[5, 5, tickLength, bottomRange]} }
35 ],

```

```

37  (** ERROR PLOT **)
ListLinePlot[totError[[1 ;; Round[60/step]]*90/3000,
  DataRange -> {0, 60}, Frame -> True,
39  PlotStyle -> {Thickness[0.004]}],
(** STAGE LINES PLOT **)
41 ListLinePlot[gammas,
  Frame -> True,
43  DataRange -> {0, degrees},
  PlotStyle -> {{Thickness[0.004], Opacity[0.5]}}]
45 ]

47 date = DateString@{"Year", "Month", "Day"};
nameStem =
49 FileNameJoin@{NotebookDirectory[], (date <>
  "-rotation-stage-phi-sweep-raw.png")};
51 Export[nameStem, productionImage, ImageResolution ->
  resolution];

```

Similar commands are used for remaining plots in these appendices, and will not be repeated.

B.2 DISASSEMBLY IMAGE ANALYSIS

The actual implementation of the automated image analysis involves multiple files and packages, and is thus unsuitable for insertion into this appendix. Below is a minimum working example that performs the major steps of the routines. Values in the code need to be manually tuned depending on the SEM used for imaging; those given here are calibrated for the Hitachi S-4800 used for approximately half the total imaging.

I assume the image being processed is stored in the variable `rawImage`. I pre-process this image with a total variation filter, producing `tvfImage`. I then create separate markers for the post and background, combine them to produce `allMarkers`, and apply them to threshold the original image. Further detail is provided in Section 5.2.4.

```

1 tvfImage = TotalVariationFilter@rawImage;
  (* Generate post markers *)
3 postMarkers = Pruning@Thinning@Binarize@SeqOpenClose@tvfImage;
  (* Generate background markers *)
5 backgroundMarker = Erosion[ChanVeseBinarize[
  FillingTransform@tvfImage, cvbMarker, TargetColor -> Black
  ], DiskMatrix[6]];
allMarkers = ImageAdd[postMarkers, backgroundMarker];
7 (* Gradient filter makes edges bright for watershed *)
Image[WatershedComponents[GradientFilter[tvfImage, 2],
  allMarkers], "Bit"] // ColorNegate;
9 finalImage = MorphologicalTransform[%, "Bridge"] //
  FillingTransform

```

Output is a binary mask, with posts white on a black background. I manually select posts in ImageJ, painting acceptable candidates red. Output is returned to Mathematica for extraction and fitting of width profiles. An example of a power law fit—this one used for the cross-sectional data in Section 4.1—is shown below, along with code to extract the value of p :

```

1 powerLawFit[data_] := NonlinearModelFit[data, wo h^p, {wo, p},
    h];
    model = powerLawFit[rawData]
3 p /. #["BestFitParameters"] & /@ model

```

In the full implementation, we stored data for each post in the following standard format:

```

1 (*{Image Name, Segment # , Length (um), wo, p, Sample Name}
   (*{ 1           2           3           4   5           6   })

```

where “Segment number” represents the object number of the particular post within the original image. To select the “full-height” clusters from all the posts in a film, I used the following function:

```

splitterv2[std6rowData_, filmHeight_] :=
2 Module[{plot, tolerancePercent, sampleName, sortedData,
    selectedData, belowData, aboveData, unselData, startIndex,
    endIndex, pRange, lengthRange},
    sampleName = std6rowData[[6, 1]];
4    tolerancePercent = 8; (* Selects values within 8% of the
        center — value tested until it was visually correct *)
    pRange = {0, 1.2};
6    lengthRange = {0, 1.5};
    sortedData = (Transpose@std6rowData)~Sort~(#1[[3]] < #2[[3]]
        &);
8    selectedData = Select[sortedData, Abs[#[[3]] - filmHeight] <
        filmHeight*(tolerancePercent)/100 &];
    startIndex = First@First@Position[sortedData,
        First@selectedData];
10    endIndex = First@First@Position[sortedData,
        Last@selectedData];

12    belowData = sortedData[[1 ;; startIndex - 1]];
    aboveData = sortedData[[endIndex + 1 ;; Length@sortedData]];
14    unselData = belowData~Join~aboveData;

16    selectedData[[All, 6]] = sampleName;
    belowData[[All, 6]] = sampleName;
18
    (* Recall that data has the form {{#, #, Length, wo, p, #}} *)
20    plot =

```

```

22 {
    ListPlot[{Transpose@{unselData[[All, 3]], unselData[[All,
        5]]}],
    Frame -> True, FrameLabel -> {"Length (\[Mu]m)", "p"},
24 PlotLabel -> sampleName, BaseStyle -> {FontSize -> 24},
    PlotRange -> {lengthRange, pRange},
26 LabelStyle -> {FontFamily -> "Calibri"},
    PlotStyle -> {ColorData[1, 2], PointSize[0.01]},
28 ImageSize -> Scaled[0.3],
    GridLines -> {{}, {{0.25, {Thick, Red}}, {0.31, Thick},
        {0.5, Thick}, {0.66, {Thick, Red}}}},
30 ListPlot[
    Transpose@{selectedData[[All, 3]], selectedData[[All,
        5]]},
32 PlotStyle -> {ColorData[1, 1], PointSize[0.01]}] (*,
    (*Plots line at full film height*)
34 Graphics@Line[{{filmHeight, 0}, {filmHeight, pRange[[2]]}}] *)
    ];
36 {selectedData, belowData, plot}
38 (*Quick Test to make sure no posts are discarded*)
    (*Length@{belowData, selectedData, aboveData, (belowData~
        Join~ selectedData~Join~aboveData), sortedData} *)
40 ]

```

This was called with a manual estimate of the center of the region:

```

1 {d20110129b1sel10prct, d20110129b1sub10prct,
    d20110129b1plot10prct} = splitterV2[standardData, 1.3];

```

B.3 METHOD COMPARISON

The below code produced the method comparison in Figure 5.1, beginning with a list of ω_0 , p pairs output for the film.

```

1 methodCompare[{fitwo_, fitp_}] :=
    Module[{widths, model, micronModel, discreteP, discreteWo,
        disassembP, disassembWo},
3 widths =
    Plus @@ MapThread[fitWidth[#1, #2] &, {fitwo, fitp}] /
        Length@fitp;
5 model = powerLawFit[Transpose@{taschukHeights*1000, widths}];
    micronModel = powerLawFit[Transpose@{taschukHeights, widths}];
7 discreteP = p /. model["BestFitParameters"];
    discreteWo = wo /. micronModel["BestFitParameters"];
9 disassembP = Mean[fitp];
    disassembWo = Mean[fitwo];

```



```

11  {{disassembP, disassembWo}, {discreteP, discreteWo}, model,
    widths}}
13  comparisonData =
    methodCompare[[rawData]] // Transpose];
15  {{ "Sample Name", "Disassembled p", "'Discrete' p", "Percent
    Change" }} ~ Join ~ Transpose@{clusterNames, comparisonData[[
    All, 1, 1]],
    comparisonData[[All, 2, 1]], (comparisonData[[All, 1, 1]]
    - comparisonData[[All, 2, 1]])/
17  comparisonData[[All, 2, 1]]*100} // TableForm

```

APPENDIX: THE FRIDGE

The thesis is the grad student's holy grail, the olive wreath upon his brow, the great work for which he endures the drudgery of his degree. But this crowning achievement is also his greatest curse, a project so crushing in scope that it unleashes all those demons peculiar to academia—worst of all, the grotesque and drooling spectre that is procrastination.

This is the story of one innocent Saturday afternoon, mid-winter, when the author encountered such a demon. This is the story of the consequences of one foolish distraction, and the disaster it nearly wrought. And this is the story of why the fridge—the one that even now might be cooling your sandwich, dear grad student—is a lie.

THE PRELUDE

Before we begin, one fact must be clearly and distinctly understood: I am addicted to the cool and refreshing taste of Coca-Cola Zero.

This is not to say that I love it: unable to stomach coffee's bitterness, I'd turned to the liquid as a palatable source of caffeine in those long pre-exam nights. It's a smoother version of Diet Coke, with the full, ponderous might of Coca-Cola's advertising division targeting it at young adult males. Successfully, apparently.

Perhaps it was a defect of my character, or perhaps just the nature of chemical addiction, but I found myself consuming much more of this carcinogenic refreshment than any man ought. I craved it. I hungered for it. I needed it. But excessive application had an unexpected consequence: I found growing within me a deep hatred of its taste, even as I purchased more and more to satisfy my yearning. I began to loathe the very object of my desire. What once was invigorating and delightful began slowly to become the object of dread.

Happily, it was not long before I stumbled upon a seemingly innocuous solution, one that promised long-term relief. Ice cubes. Adding a handful, hearing that sizzling fizz, their peaceful clacking against the glass, tasting the crisp, incomparable coolness—I'm not sure precisely what it was, but the addition of ice returned the burden into a delight.

It quickly became a problem of logistics.

As a grad student, I spent an inordinate amount of time in the lab, and that was where the need was most sorely felt. Transporting ice from home was impractical—a conclusion reached, sadly, through trial and error. The only alternative was making the ice in-lab. But, not outfitted with the the gargantuan antique of the students three

floors above me, the only available option was the 3.2 cubic feet of refrigeration supplied by the lab's dutiful mini-fridge.

It was an unassuming appliance, glossy white, staunchly standing atop a beige table in the lab's lunch area. The interior was similarly nondescript, and largely what you'd expect to find in a den of graduate students: Tupperware-clad sandwiches resting on wire shelves, a lunch bag or two. Condiments from some long-forgotten lab picnic huddled in a corner with a bottle of vinaigrette. A little rack in the door restraining some pop cans, ready at any moment for some weary researcher to free them from their wire cage. The freezer was a few inches of space at the very top, a flimsy plastic door swinging up to reveal a tiny, ice-encrusted cavern. Its disuse was evidenced by the sheer thickness of the ice—two inches at least on the bottom, an inch on the top, with only an inch of clearance in between. Just enough. This would have to do.

For anything to come of it, though, I first needed ice cube trays. I could try to find some at home, of course, and bring them in in next week—but this fateful Saturday morning, that seemed a future far too distant. I needed ice now. And, the faintest scrap of memory was drifting through my mind—hadn't I seen an ice-cube tray in the lab, sometime years past? A little white one? Mightn't it still be around, somewhere? Could it not, perhaps, still be in the freezer, swallowed up in the glacial advance of the freezer's ice? Could I—oh, what a thought!—could I liberate it, and taste the fruits of my labours this very afternoon?

And it was with this question that I felt my old, familiar demon jolt awake. Procrastination, who'd been silent in fitful slumber, sensed but the faintest scent of opportunity. Thesis writing is no engrossing pursuit, and how desperately I leapt at any distraction, any other problem that could take momentary precedence! I wish I could say I fought him, as he woke, that I ignored his seductive words, his alluring whispers tempting me to investigate the tray, to liberate it from its icy jail. But I did not. I resolved to find the tray. To make ice. And that made all the difference.

THE PROBLEM

The lab is a busy place—as grad students are free to set their own hours, one never knows when they'll be in the lab. They often flock, moth-like, to the incessant glow of the lab's fluorescents in the blackest night. But this Saturday afternoon, I was alone. There was no one to see me search unsuccessfully for a chisel, finally settling on a screwdriver and a hammer as my weapons against the crust of ice. Defrosting the machine was impractical—how would I keep everything cold in the meantime? And how would I contain the inevitable runoff?

And so, freezer flap propped open against my forearm, I began my assault. And, oh! What an assault it was! The point of the screwdriver driving deep into the heart of the ice, wedging, prying, twisting! Each deft stroke of the hammer weakening it, shattering it! Imagine my ecstasy, as vast chunks of ice began to fly free, clattering and skittering across the plastic table below. It was but the work of the moment to confirm my suspicions, and but a moment more to wrench a tiny ice-cube tray free from its frosty prison. Victory was mine: any doubts as to the questionable wisdom of hammering a screwdriver into a fridge had quickly vanished.

But it was here, at the height of my triumph, at the height of my hubris, that I reached too far. Progress swift and satisfying, and I resolved to remove all of the ice that had grown onto the freezer's walls—Icarus, flying too close to the sun. Diligently hammering, I found a section that proved particularly resilient. The screwdriver had bored a hole too close to the freezer edge, and I was hammering along the plastic surface, wedging ice up and off.

It was slow going, but gradually successful.

Until I heard a sound.

A despicable, gurgling sound. Gas bubbling weakly through water.

And, as I wrenched the tool loose, a thin tendril of mist began to leisurely curl its way down from the hole my screwdriver left, trailing down off the edge of the freezer and vanishing into space. The familiar tang of freon hit my nostrils, and I knew in an instant that the worst had happened: I'd punctured the freezer's freon lines. I'd broken the fridge.

My mind frantically scrambled for a solution. Could I plug the hole? Undo the damage? Fix it all? I ran to the sink, and brought back some water, pouring it over the hole—perhaps I could freeze it over, containing the rest of the freon. It seemed to work, and the hissing and bubbling receded. But I knew it was at best a band-aid, and I needed a more permanent solution. I'd have to purchase a replacement fridge—the thought of telling our post-doc filled me with dread. I could so pristinely picture my explanation, and his incredulity—a hammer? A screwdriver? To get ice out of the freezer? All this after already earning his ire and rolled eyes, almost evaporating a flashlight with a focussed beam of electrons. Oh, what well-deserved shame awaited me! What mockery! I would replace the fridge, of course, but it was the derision I dreaded the most!

But did they have to know? Did my lab-mates have to find out? If I was going to replace the fridge anyway, could I somehow do it in secret? Fix the problem with none having been the wiser? I felt my resolve harden, my will crystallize into iron.

I'd broken the mini-fridge in a fit of colossal stupidity. I needed to fix the problem. And, above all—

—no one could ever know.

THE PLAN

The lab is not empty on the weekends. But it is spared the weekday's foot traffic, when the lunch area bustles with starving students. It was conceivable that my crime could go unnoticed, at least until Monday morning. With coolant leaking, though, even the most Herculean efforts of the tiny fridge would be unable to keep contents cold—the vinaigrette could survive, perhaps, but the assortment of leftovers and yoghurt would surely perish. If I was to fix this problem, I needed to act quickly.

Minutes later, model number copied a sticker on the fridge's rear, I was learning that it was no longer actively manufactured. Some department stores had a newer version. It looked... similar, perhaps similar enough to fool a distracted grad student: making some calls, I found one well-stocked shop open until ten. The classifieds were less promising—the only lead was a seller just describing the make and the size. They matched, but the model number wasn't given. And he wouldn't answer my calls—I had no time to wait for a response. With the remaining ice in the freezer already starting to drip, I had no time.

And so I began assembling a team. I would have to buy the new fridge, and hope for the best, and I'd need help making the switch. Explaining my plight, and waiting for their incredulous laughter to die down, I secured the help of two friends—we'll call the first Amélie, and the second Ivan, to protect the innocent. We planned to meet after dark.

We dressed in black.

And then, a stroke of luck—the mysterious seller called me back, and would be willing to part with his fridge that very night! He claimed it was in good working order, but didn't know the model number: I'd have to see it in person. But he couldn't meet me until eleven thirty, well after dark. He wanted to rendezvous in a back alley. A back alley in a dangerous neighbourhood. In the middle of the dark winter night. All my suspicious were aroused, but too much was at stake to consider anything but action. The plans were made—assembling my team at nine thirty, purchasing the brand-new fridge as insurance, and then risking late-night rendezvous with a menacing stranger at eleven thirty.

For the first time since I smelled the fateful freon, I began to hope.

THE PREPARATION

Darkness fell. Three figures, darkly clothed, found themselves briskly striding across the blinding tiles of Canadian Tire towards a gleaming Danby mini-fridge, propped on a box near the barbecues. The fridge that could fix everything.

As I drew near, my spirits rose. It *was* similar. Same size, same shape, same color—even the same little Danby badge in the center. It lacked the decorative plastic top of its ruined compatriot, but this might go unnoticed. I stepped close, opening the painfully white door, and my heart sank.

They'd updated the door's interior.

In place of the familiar beverage rack were plastic fingers, reaching out of the door, grasping cans individually. No one could miss such a difference. Questions would be asked. The truth would out.

This fridge would not do—all my hope now rested in the hands of a mysterious stranger, waiting in a dark alley on a cold midwinter night.

The hour arrived with alarming quickness. I breathlessly steered through ever more decrepit streets, drawing closer to an address just blocks south of a frozen train yard. The urban decay of our surroundings was iced with a thin layer of snow. I steered into the alley, dimly illuminated with orange streetlamps, and there, in front of a dilapidated white garage, sat a featureless white car, exhaust lazily drifting into the clear winter night. The violent glow of brake lights painted the snow a desperate red.

Tires crunching across the ground, I rolled to a stop across the alley and got out to meet our contact, Ivan at my side. Out from the car emerged a massive man, moustached. Pleasantries exchanged, he turned and pulled open the garage door, beckoning us into the dark interior. Into the dark.

We strode in cautiously, alert, adrenaline coursing through our veins, and—and there it was. A white Danby fridge, eerily familiar in the shadows of the garage, plugged into the unfinished wall to demonstrate its functionality. I opened it haltingly, filled with dread, and—and it was identical to its broken cousin, down to every last detail. The beverage rack. The temperature control. The freezer that had started the entire adventure.

The exterior, though—this was less promising. It too lacked the decorative plastic top, and its brand read "Diplomat" instead of "Danby." What's more, the door's plastic trim had yellowed, presumably left in the sun by some careless former owner.

But there was no time; I had no choice. Hands exposed to the biting cold, I passed the towering Frenchman three green bills, and we hoisted the freezing metal into the bed of my truck. We drove away from the silent alley, and towards the University, hope once again rising. For the first time, our plan was beginning to fall into place.

It was still too early—it was still too likely that some grad student was still in the lab, bearing witness to our exchange. We stopped on the way, conversing, waiting, until we felt it late enough to be safe. And then, when we could wait no more, we continued the journey, backing the truck up to the glass doors of the lab. It was time.

THE EXECUTION

The lab building is secure at night; entry requires a card swipe through the exterior doors, then a second into the lab hallway. A key gives entry into the lab area, and a second key into the lab proper. The lab is a cavernous room, filled with row upon row of benches and shelves, stacked with a dizzying array of equipment. Two doors, each set with a glass window, provide entry. The doors face one another in opposite walls, across the entire length of the room. The fridge stands near the north door—striding through it and six feet into the lab, a right turn brings you around around a shelf into the lunch area, and turning back towards the door faces you toward the fridge.

We approached from the north, to minimize the distance and our chance of exposure. I briskly swiped my way into the lab, with my companions waiting outside; I had to ensure the coast was clear. I crept silently through the darkened halls, and through the locked doors of the lab area. Silence reigned. It was deserted, but my eye caught something slightly out of place—was that a jacket, hanging beside Jaron's desk? It was not beyond the pale of possibility; one of the lab's most diligent, he could be expected in the lab at any time. But he himself was not there, not by his desk, nor in the lab. The venture could proceed; again, there was little choice.

And so I crept back to my accomplices. Ivan and I carried in the new fridge, Amélie swiping open the doors in the fluorescent light of the hallways. We glided into the lab, urgently whispering. The broken fridge was already dripping, a small pool forming on the floor when I opened the door. We didn't dare turn on the lab's lights, working by the hallway's dim glow that filtered through the windows.

We moved in perfect sync, sliding the old fridge off the table and standing the replacement in its place. A quick snapshot recorded the positions of its contents, and we began to move over the ingredients. Armed with paper towel, I set about cleaning the worst of the interior. In mere minutes, it was done: the vinaigrette in its new home, and the new fridge emitting familiar hum. It was done.

I still had to sop up the water, but we first needed to escort the old fridge from the premises. Each grabbing an edge, we walked it around the shelf. My heart began to pound as I backed through the lab door, fridge in between us—we were succeeding! Finally, victory, as incredible as it seemed, was within grasp! Everything had fallen into place.

But once again, I heard a sound. And once again, it filled me with dread.

I heard keys.

I looked up, across the lab. I was thunderstruck; how could this happen? At this very moment, just as we were escaping? So wreathed in a grim inevitability? There, framed in the door's window, was a

silhouette. Fighting with his keys, about to enter the darkened lab, about to see us fridge in hand, was Jaron van Djiken.

I hadn't a moment to lose. The entire venture rested on a razor's edge; we were seconds away from exposure. I gave a hushed shout, urging speed, and pulled back with all haste. Three quick strides took us into the hall and around the corner, and—and just as we were out of sight, I saw the lights turn on. Without pause, we moved through the door, down the hall, out into the night. The broken fridge was in the truck before I could explain to my shaken companions how close we had come to disaster. How close was our brush with failure.

Taking a moment to get my breath, I slowly realized that the night was not over; we'd left a pool of water, and the rearrangements and cleaning were not quite complete. And we'd left a trail of drops, down from the middle of the lab, through the hallway, and out the north doors. If Jaron noticed it, all was again lost. I had to find out how much he knew. I had to tie up these loose ends. I had to return to the lab.

I crept in gingerly—perhaps Jaron had simply passed through on his way out, and had seen nothing. But as I approached, I saw that the lab was still lit: Jaron was still inside. I walked in—the only way to avert disaster was to face it head on.

I greeted him, hunched over the microscopy bench on the lab's east wall.

I asked him what he was doing here, at this late hour. He asked me the same.

"Oh. Today I finally decided clean out all of the ice up in the freezer. We can now make ice!" I forced enthusiasm into my voice.

He laughed. "Anything to avoid writing your thesis, mm?"

One thing was perfectly clear. Somehow, he didn't know.

The secret was still safe. I cleaned up the drop trail with my foot. We chatted, briefly, about theses, about LaTeX, about our stratagies. He went back to work, and I hastily cleaned the pool of water, finished the brunt of the cleaning, and bid him goodnight, summoning all my will to keep my tone measured and my pace calm.

The swap was complete. The plastic on the new fridge door was yellowed, but I was confident that no student, wandering past, would notice the difference.

And what if they did? What would they assume from such a small difference—that they misremembered? That they'd missed the slow yellowing over time? That a small team of desperate conspirators had quietly snuck into the lab in the dark of night, replacing the aged mini-fridge with a near-identical copy, save for some slight discolouration?

It would strain the belief of even the most imaginative labmate. Because that would be crazy.

I still had to change the nameplate on the front of fridge, but that could wait until tomorrow—it was unlikely that any others would venture near the fridge on a Sunday morning, and I could scarcely risk another encounter with Jaron, one that would raise questions for which I had no willing answers. As to the yellowing, I would begin my research—surely there was some chemical means of rectifying the discolouration. The war was far from over, but somehow, against all odds, the night's battles had been won.

THE FINALE

The light of morning brought new clarity. By early afternoon, research into a chemical cure gave way to a more practical solution: if the fridges were the same model, could I not simply disassemble the broken fridge, and use its door on its replacement? Could I not unscrew the decorative top, and reattach it to the functional model? And the racks, all the interior components—could I not bring them too to the lab, and ensure no visible differences remained evident?

The door came off with ease, designed to be mounted for opening in either direction. The decorative top piece posed more of a problem—held down with screws, the ruined fridge had screwholes tapped into its metal top, holes not present in the replacement model. I would either have to drill my own holes, and risk puncturing essential components a second time, or come up with an alternative. My eyes darted to the caulking gun on my garage shelf. There was a solution.

The old fridge cannibalized, I prepared it for transit to its final resting place at the Eco Station. The chunks of ice I'd initially fought to remove were nearly melted now, falling lifeless from the freezer compartment.

A Pyrrhic victory, but one that satisfied me regardless.

As dusk fell, I reassembled the team, carrying a dark satchel with the tools I required—a screwdriver, two full caulking guns, a knife to break their seals. We drove to the University in silence, focused on the mission at hand: purposely striding into the lab, swiping through the card readers, and through both the lab's locks. The floor was deserted; we could work in peace.

There was no coat by Jaron's desk. We made sure of that.

And so we set to work, quickly replacing the door, which snapped into place with satisfying ease. In a moment, "Diplomat" was replaced with the familiar "Danby," and the yellowed plastic was no more. Flipping over the plastic top, I carefully beaded the caulking across each of its plastic ribs, the pungent odour of the silicone filling the lab. Settling it into place, I sealed the front edge with an extra pass, the crude line demonstrating my inexperience. Two strips of duct tape ensured that the piece would hold until the caulking set, as we finished

cleaning the interior and ensured that the balsamic vinaigrette was huddled just as before. Freon was harmless—I'd checked its MSDS sheet to make sure—but I wanted to take no chances, washing the abandoned items with a care disproportionate to their status. Stepping back, we felt a slight glow of pride: it was perfect.

Every detail was the same. The fridge internals were identical. Now, thanks to our handiwork, the exterior was completely indistinguishable, save for a thin line of caulking under the lip of the plastic top, a line easily missed by the keenest observer. Only an innocuous strip of duct tape and a lingering odour of silicone gave witness to our presence. With one final glance, we melted off into the winter night.

THE AFTERMATH

The next day's light ushered in the start of a new week, and the first real test of our labours. Had we missed any detail? Was there anything to notice? I worked at my desk through the morning, listening, watching. The caulking had set, and the top was firmly attached; I removed the duct tape while the lab was briefly deserted. Lunch came, students moving their food in and out of the fridge without care, and without noticing any change.

I encountered Jon in the lunch area, as I often did, jostling for use of the better microwave. He stopped my heart: "Man, it smells awful in here." I froze. The fridge still reeked, if only faintly, of last night's silicone. Could everything be undone, at this late hour?

A beat passed. "It's those solvents they're using for the chromatography. They're always doing this." He answered his own question, drifting away to eat his lunch.

The secret was safe. The only possible evidence had been dismissed. Somehow—you, gentle reader, can surely understand—the possibility of a counterfeit fridge did not even occur to him.

I microwaved my food, triumphant. Ice cubes were solidifying in the pristine freezer.

The fridge was a lie.

But this story had finally reached its happy conclusion.

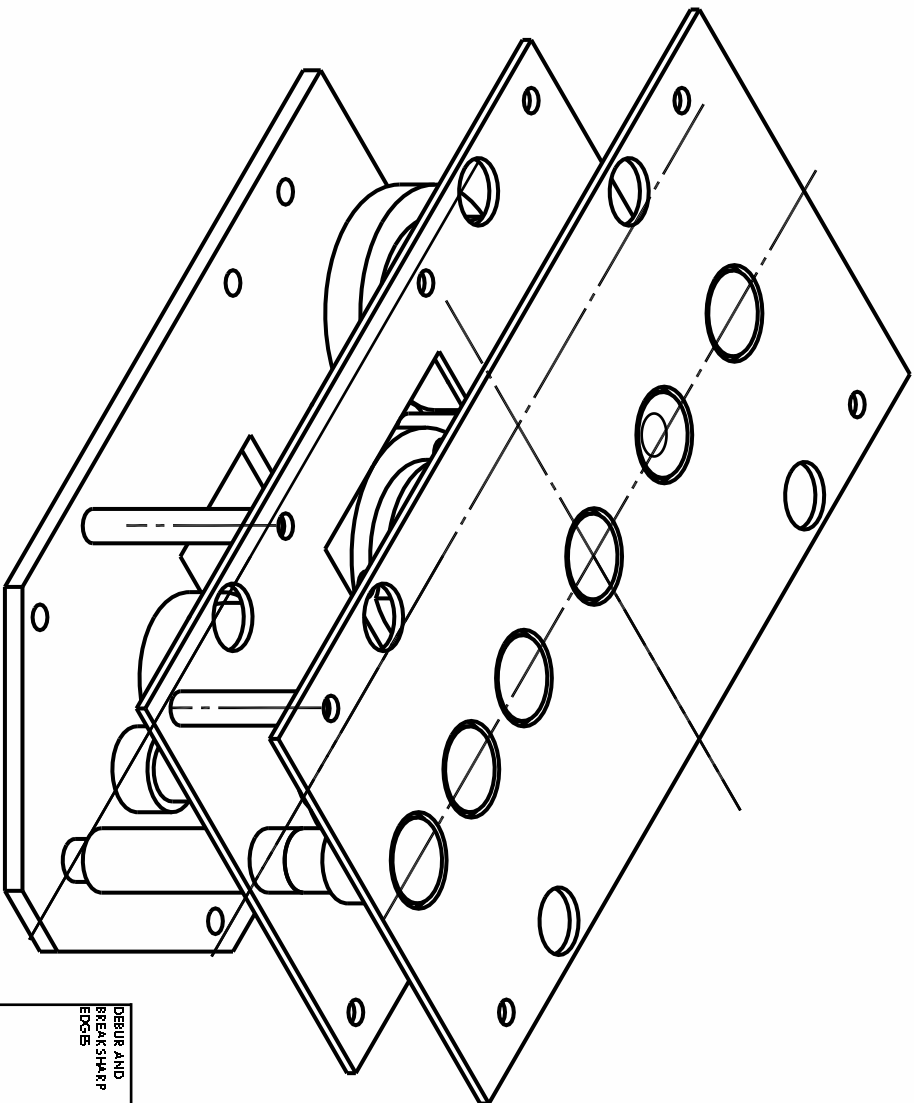
APPENDIX: SCHEMATICS

C.1 INITIAL ROTATION STAGE SCHEMATICS

The rotation stage used in this thesis underwent several revisions in the course of its development. Most notably, when the considerations of Section 3.2.1 indicated shafts should lie in the axis of α rotation, the originally designed stage needed to be bisected. The existing deposition chamber gearing occupied space on one side of the central drive shaft, and complete gearing redesign would be required to fit shafts above it. Instead, the simplest course of action was to cleave the stage in two, leaving only the four stages discussed in the body of the thesis.

The stage is designed to fit in the “Soundwave” deposition system of the ENL research group.

The original stage schematics that follow were produced by Dr. M. T. Taschuk, who designed the rotation stage and its gearing. Following this is a schematic I produced for the standoff holes in the bottom plate; their excessive number is perhaps indicative of the shoddy machinist skills of the author.



DEBUR AND
BREAK SHARP
EDGES

DO NOT SCALE DRAWING

REVISION

TITLE: **Assembled Rotation Stage**

MATERIAL:

DWG NO.

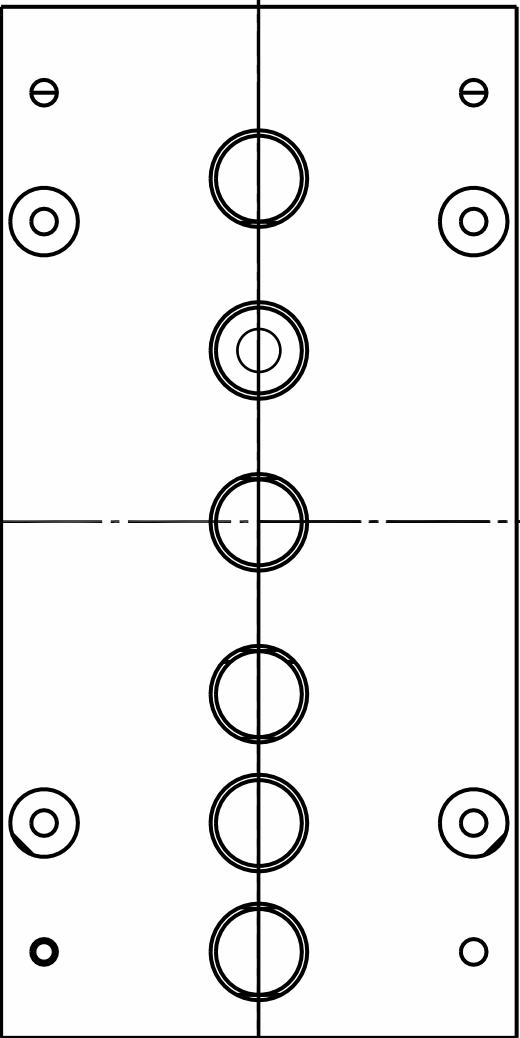
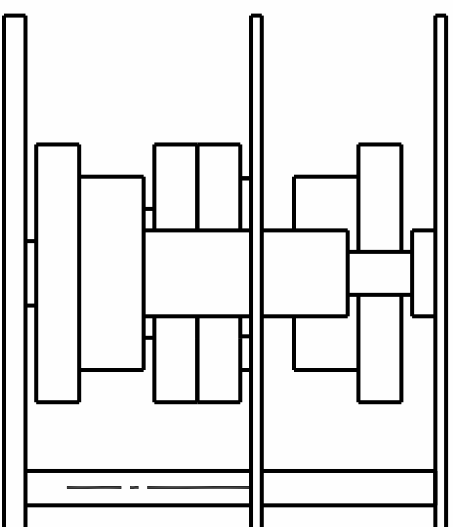
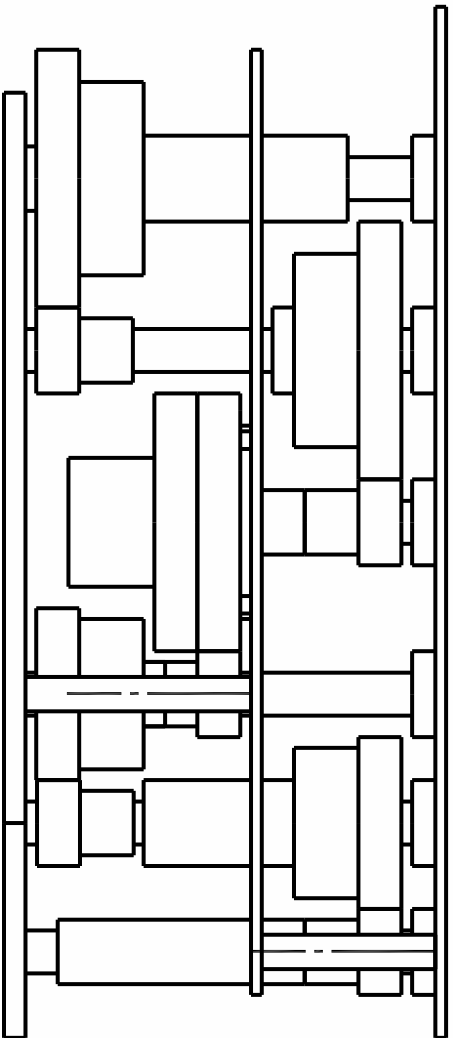
20101122-rotation-stage

A4

QUANTITY:

SCALE: 1:2

SHEET 1 OF 1



DO NOT SCALE DRAWING

REVISION

TITLE
Assembled Rotation Stage

MATERIAL:

DWG NO.

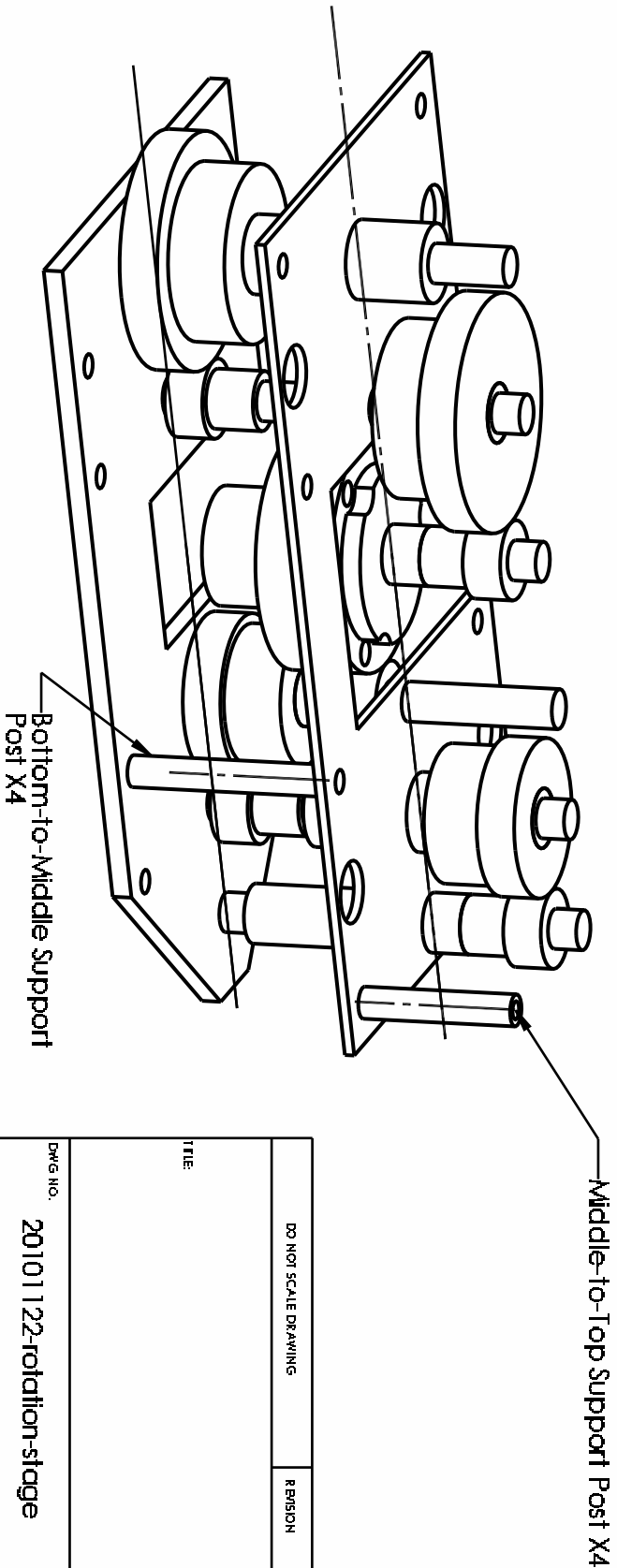
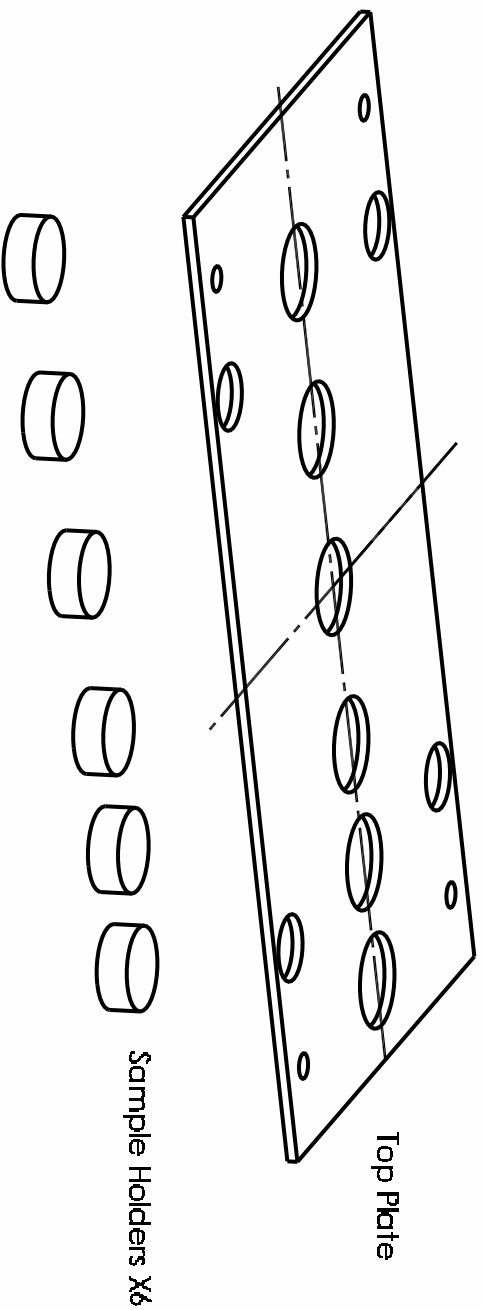
20101122-rotation-stage

A4

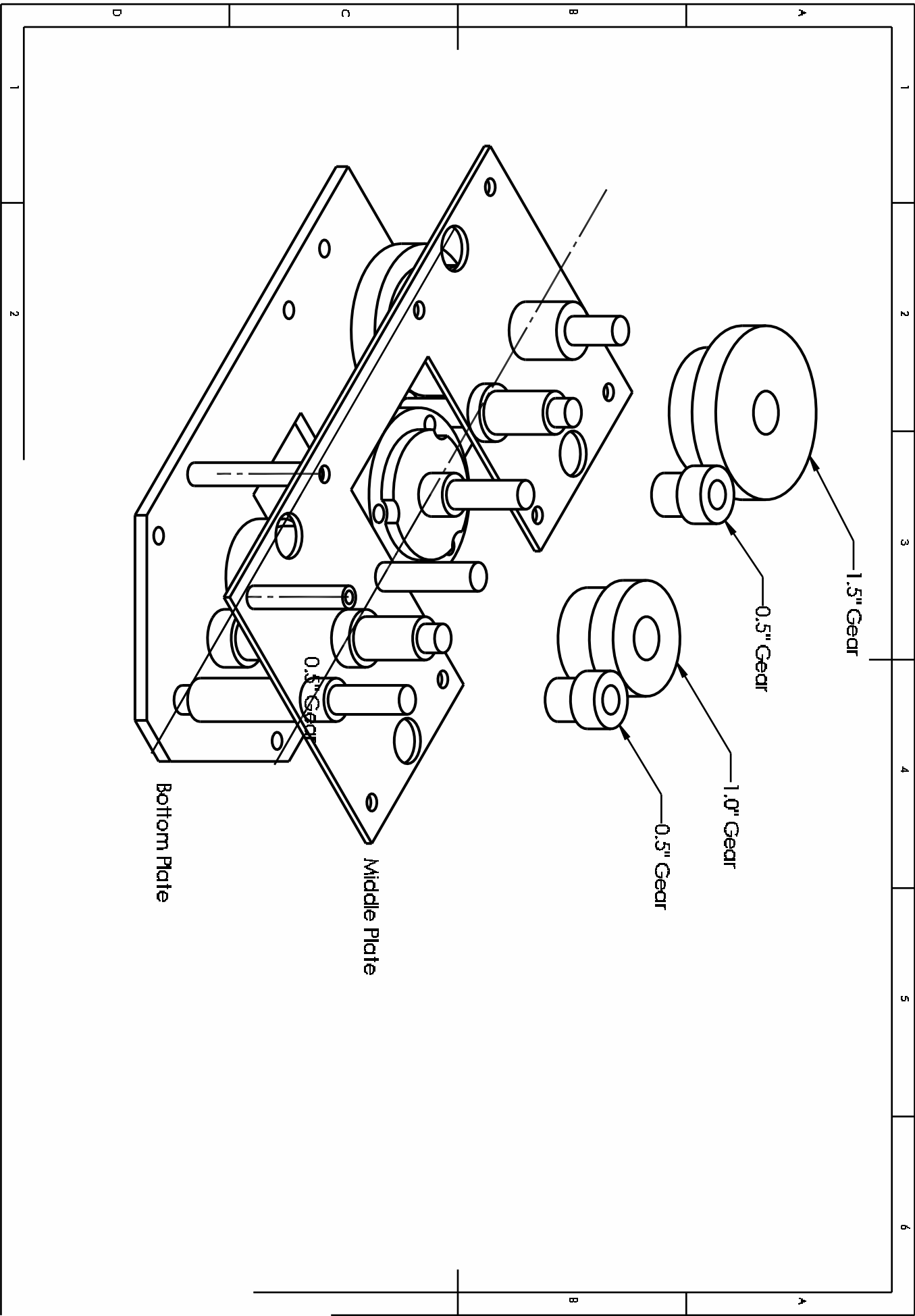
QUANTITY:

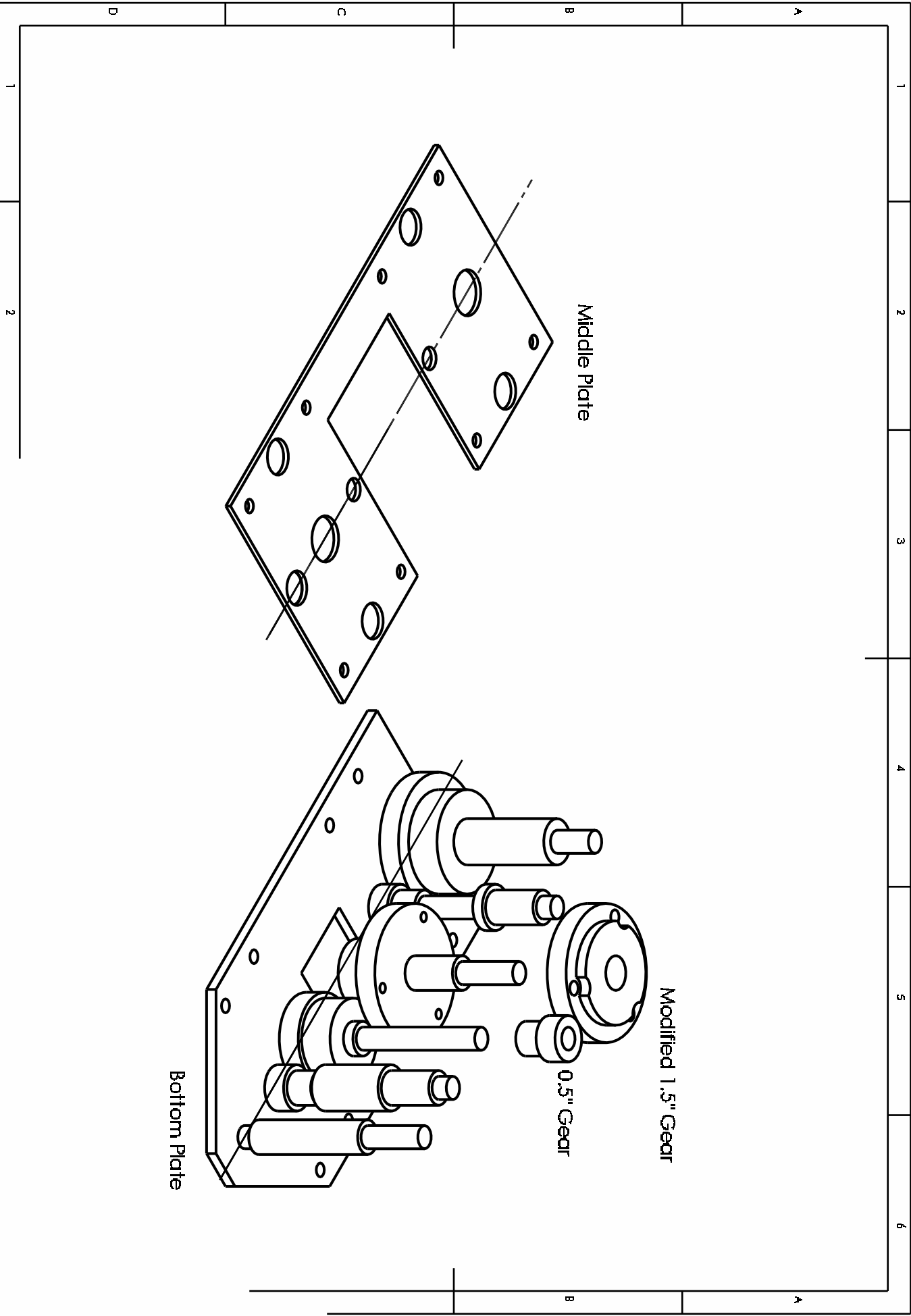
SCALE: 1:2

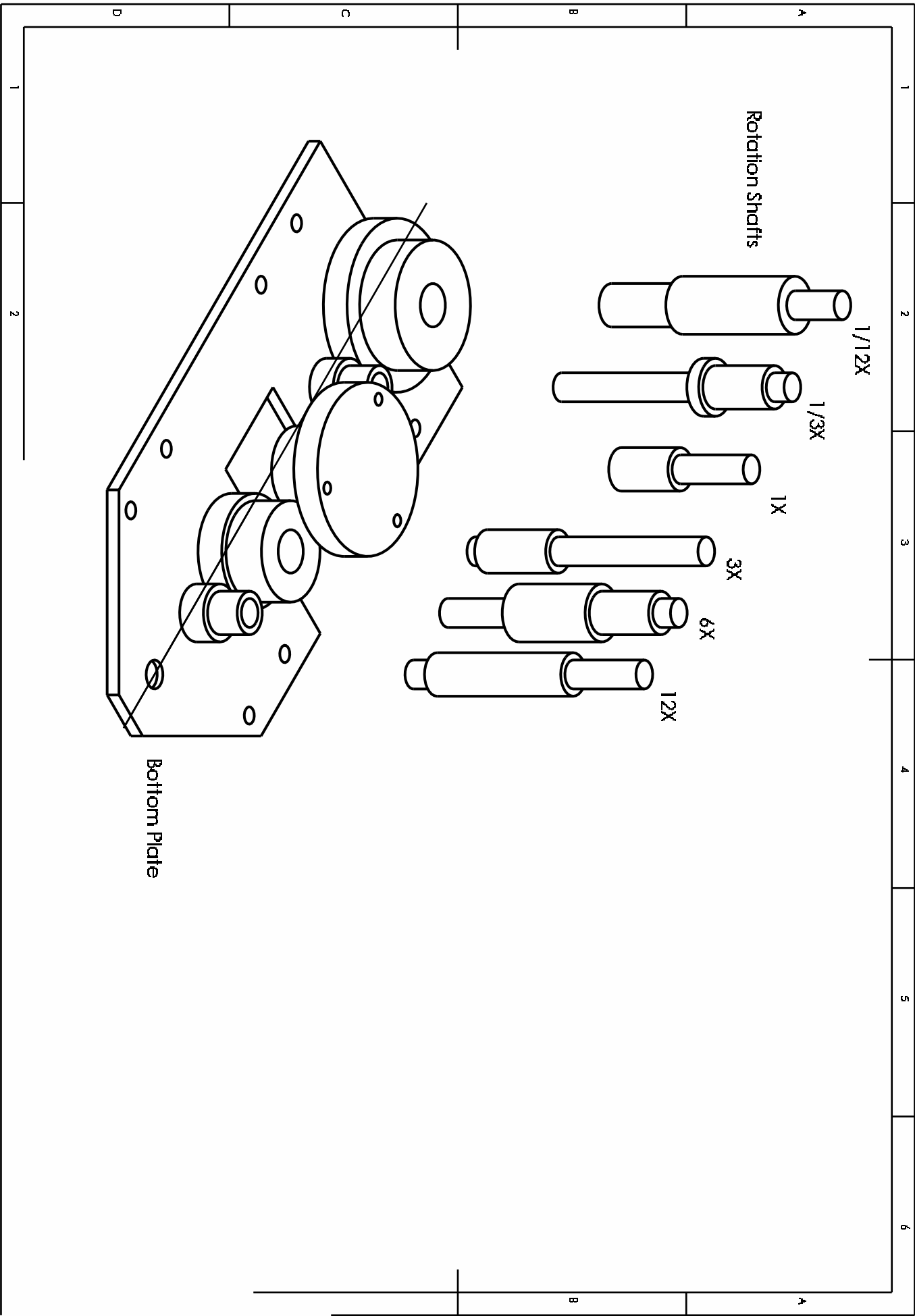
SHEET 201 7

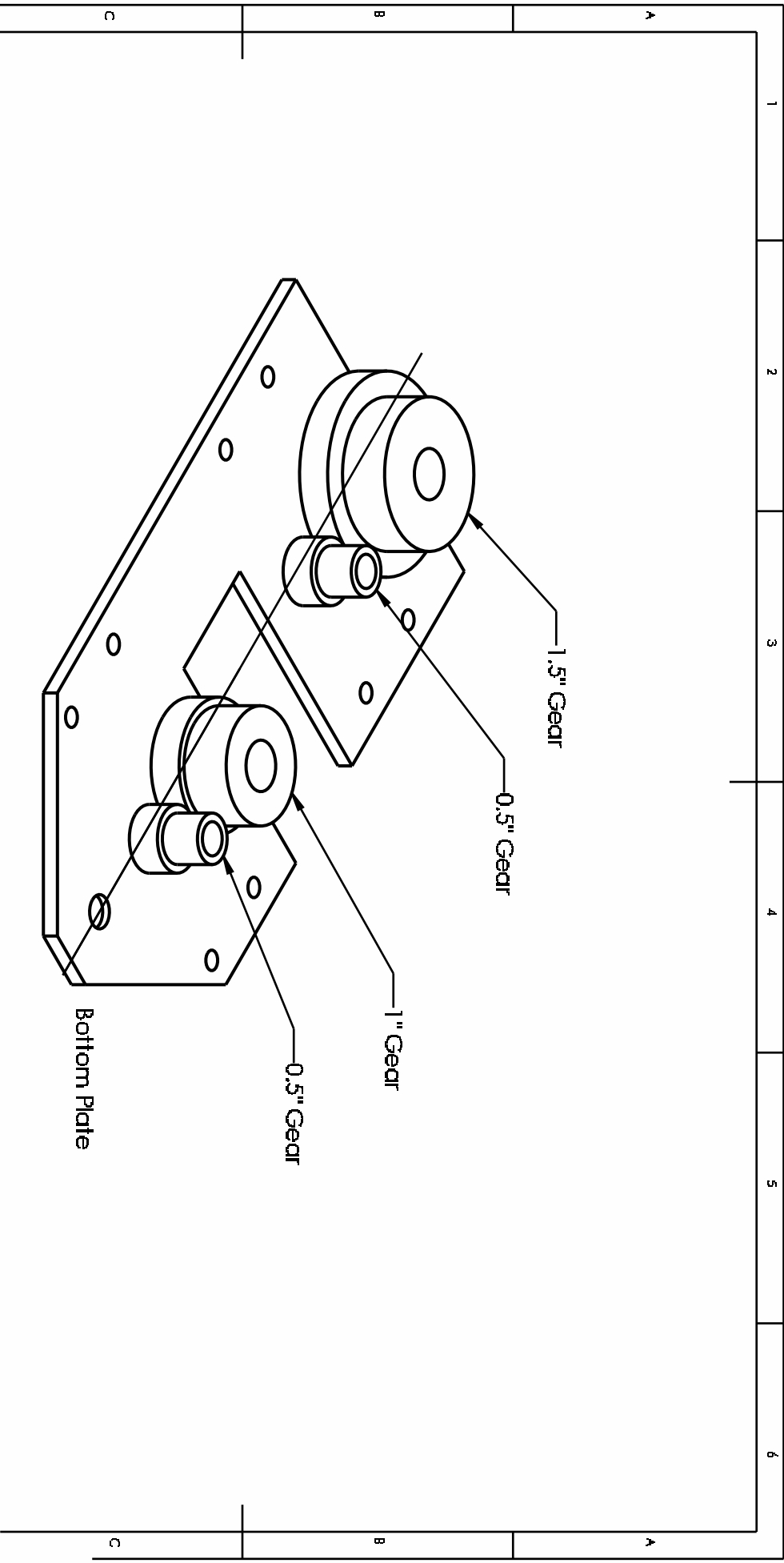


1		2	3	4	5	6
A		B		C		D
1		2	QUANTITY:		SCALE: 1:2	
DWG NO.		20101122-rotation-stage		SHEET 3 OF 7		A4
DO NOT SCALE DRAWING		REVISION		TITLE:		

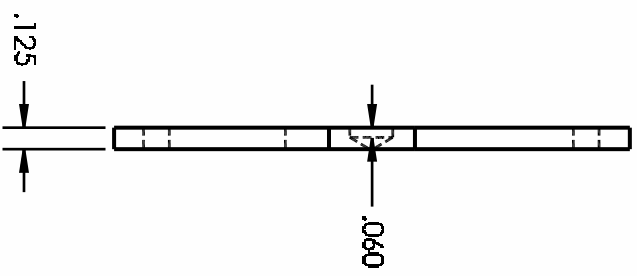
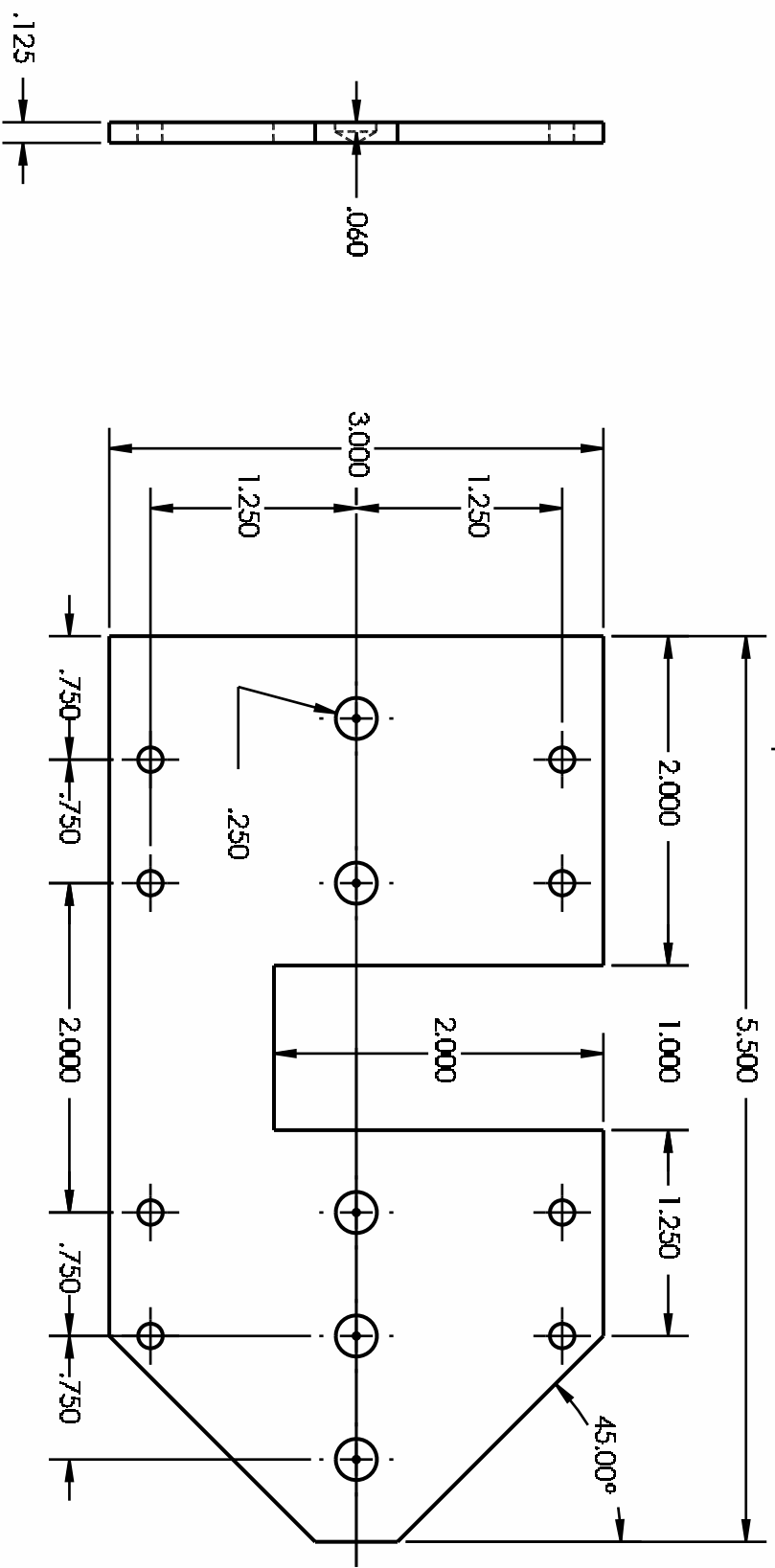






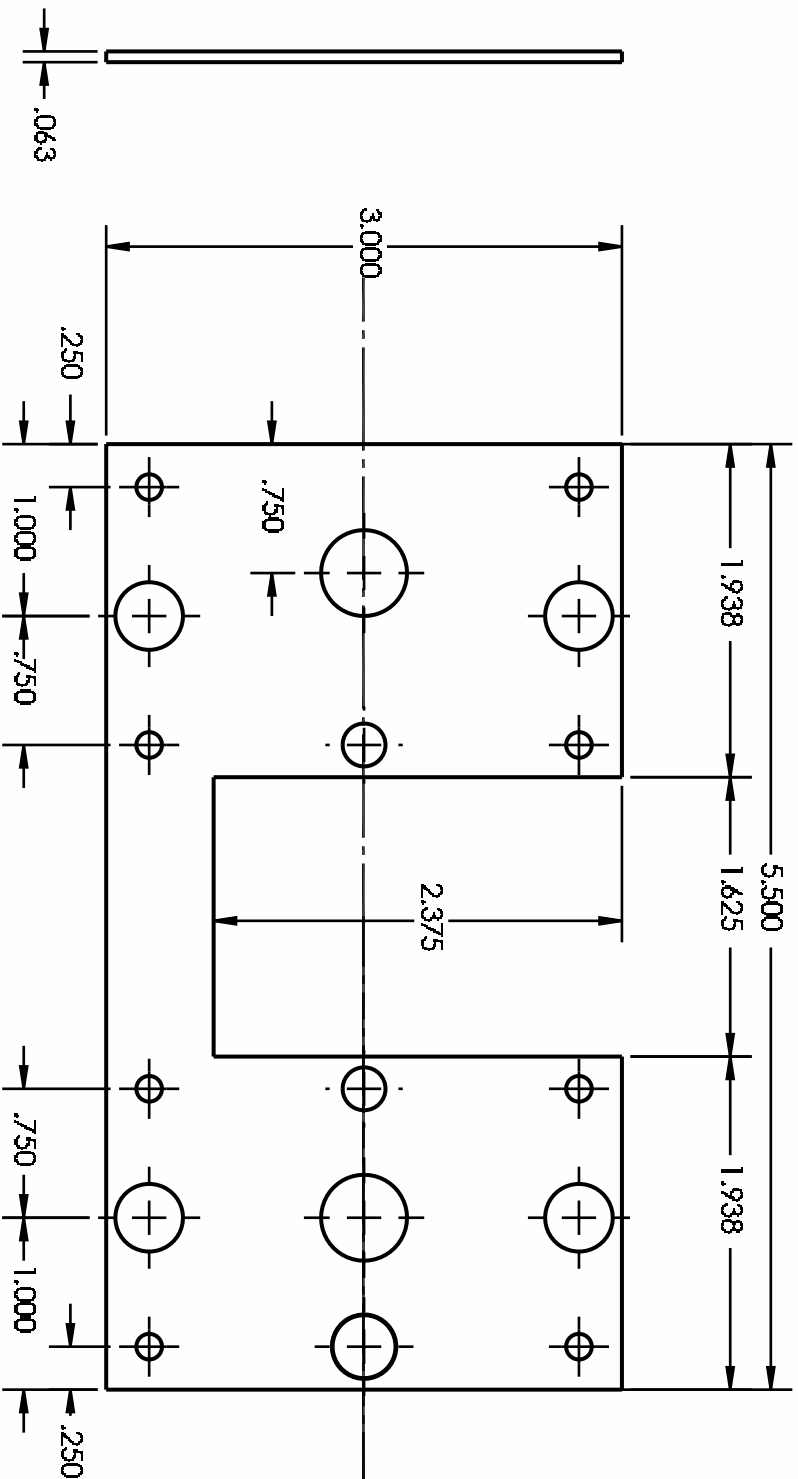


	1	2	3	4																																																																																
A																																																																																				
B																																																																																				
C																																																																																				
D																																																																																				
E																																																																																				
F	<table><tr><td colspan="2">UNLESS OTHERWISE SPECIFIED: DIMENSIONS ARE IN MILLIMETERS SURFACE FINISH: TOLERANCES: LINEAR: ANGULAR:</td><td colspan="2">FINISH:</td><td colspan="2">DEBUR AND BREAK SHARP EDGES</td><td colspan="2">DO NOT SCALE DRAWING</td><td colspan="2">REVISION</td></tr><tr><td colspan="2">DRAWN</td><td colspan="2">NAME</td><td colspan="2">SIGNATURE</td><td colspan="2">DATE</td><td colspan="2">TITLE: Modified 1.5" gear</td></tr><tr><td colspan="2">CHK'D</td><td colspan="2"></td><td colspan="2"></td><td colspan="2"></td><td colspan="2"></td></tr><tr><td colspan="2">APP'VD</td><td colspan="2"></td><td colspan="2"></td><td colspan="2"></td><td colspan="2"></td></tr><tr><td colspan="2">MFG</td><td colspan="2"></td><td colspan="2"></td><td colspan="2"></td><td colspan="2"></td></tr><tr><td colspan="2">QA</td><td colspan="2"></td><td colspan="2"></td><td colspan="2">MATERIAL: Stainless Steel</td><td colspan="2">DWG NO. 20101122-special-one-and-a-half-inch-gear</td></tr><tr><td colspan="2"></td><td colspan="2"></td><td colspan="2"></td><td colspan="2"></td><td colspan="2">A4</td></tr><tr><td colspan="2"></td><td colspan="2"></td><td colspan="2"></td><td colspan="2">QTY: 1</td><td colspan="2">SHEET 1 OF 1</td></tr></table>				UNLESS OTHERWISE SPECIFIED: DIMENSIONS ARE IN MILLIMETERS SURFACE FINISH: TOLERANCES: LINEAR: ANGULAR:		FINISH:		DEBUR AND BREAK SHARP EDGES		DO NOT SCALE DRAWING		REVISION		DRAWN		NAME		SIGNATURE		DATE		TITLE: Modified 1.5" gear		CHK'D										APP'VD										MFG										QA						MATERIAL: Stainless Steel		DWG NO. 20101122-special-one-and-a-half-inch-gear										A4								QTY: 1		SHEET 1 OF 1	
UNLESS OTHERWISE SPECIFIED: DIMENSIONS ARE IN MILLIMETERS SURFACE FINISH: TOLERANCES: LINEAR: ANGULAR:		FINISH:		DEBUR AND BREAK SHARP EDGES		DO NOT SCALE DRAWING		REVISION																																																																												
DRAWN		NAME		SIGNATURE		DATE		TITLE: Modified 1.5" gear																																																																												
CHK'D																																																																																				
APP'VD																																																																																				
MFG																																																																																				
QA						MATERIAL: Stainless Steel		DWG NO. 20101122-special-one-and-a-half-inch-gear																																																																												
								A4																																																																												
						QTY: 1		SHEET 1 OF 1																																																																												



UNLESS OTHERWISE SPECIFIED:			FINISH		DEBUR AND BREAK SHARP EDGES		DO NOT SCALE DRAWING		REVISION	
DIMENSIONS ARE IN MILLIMETERS										
SURFACE FINISH										
TOLERANCES:										
LINEAR:										
ANGULAR:										

NAME	SIGNATURE	DATE	TITLE		DWG NO.		A4	
DRAWN			Bottom Plate; Alignment for rotation shafts, and clearance holes for support pins.		20101122-bottom-plate			
CHECKED								
APPROVED								
WKS								
Q.A.								
			MATERIAL:					
			Stainless Steel					
			QUANTITY:		1			



UNLESS OTHERWISE SPECIFIED:
DIMENSIONS ARE IN MILLIMETERS
SURFACE FINISH
TOLERANCES:
LINEAR:
ANGULAR:

DEBUR AND
BREAK SHARP
EDGES

DO NOT SCALE DRAWING

REVISION

TITLE:

Middle Plate; support of shafts and
holes for support pins

NAME	SIGNATURE	DATE
DRAWN		
CHECK'D		
APPRO'D		
WKS		
Q.A.		

MATERIAL:

Stainless Steel

DWG NO.

20101122-middle-plate

A4

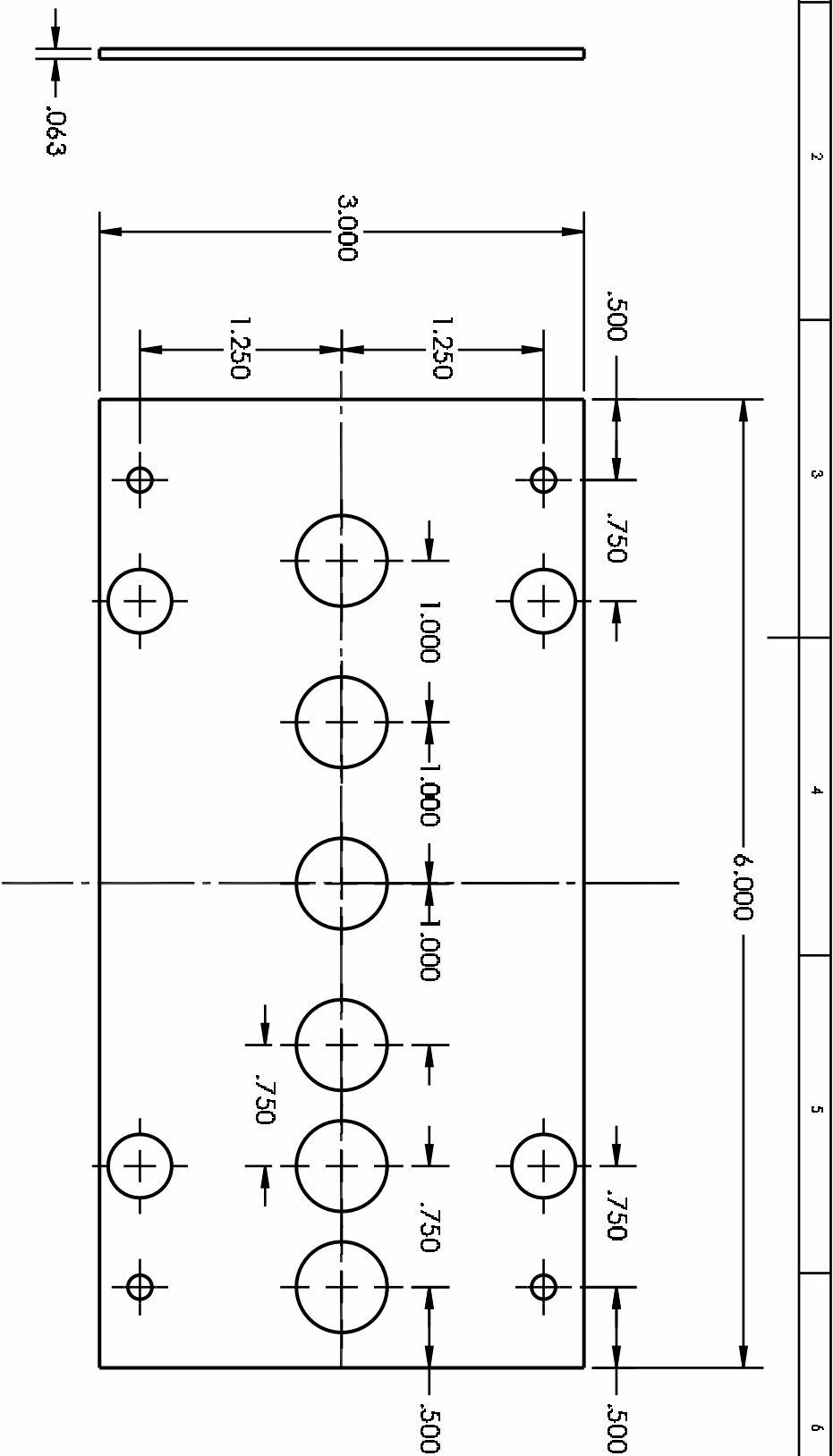
1

2

QUANTITY: 1

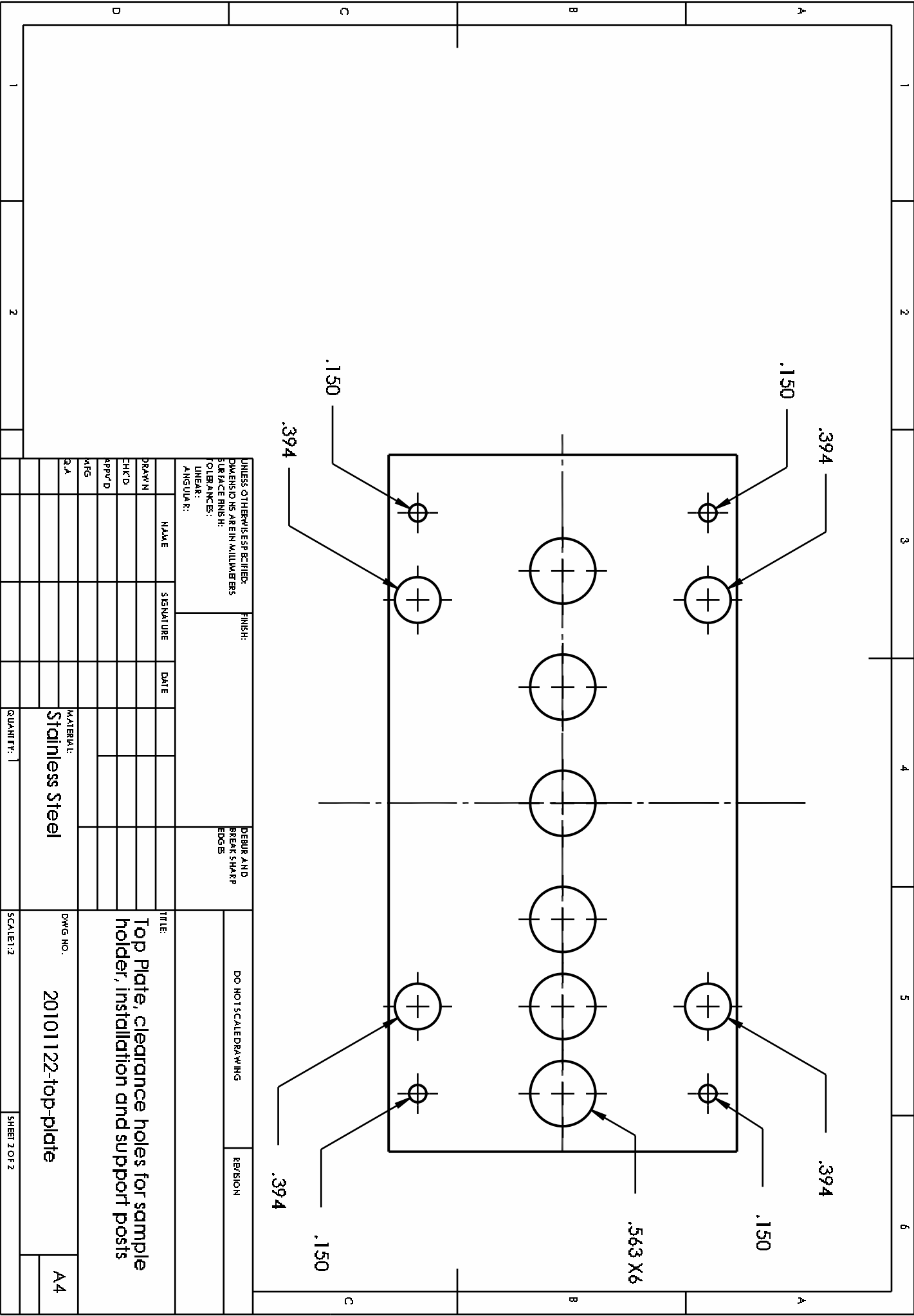
SCALE: 1:2

SHEET 1 OF 2



UNLESS OTHERWISE SPECIFIED: DIMENSIONS ARE IN MILLIMETERS			FINISH:		DEBUR AND BREAK SHARP EDGES	
SURFACE FINISH:						
TOLERANCES:						
LINEAR:						
ANGULAR:						
DRAWN	NAME	SIGNATURE	DATE			TITLE
CHK'D						Top Plate, clearance holes for sample holder, installation and support posts
APP'D						
MFG						
Q.A.						
			MATERIAL:			DWG NO.
			Stainless Steel			20101122-top-plate
			QUANTITY: 1			SCALE: 1:2
						SHEET 1 OF 2

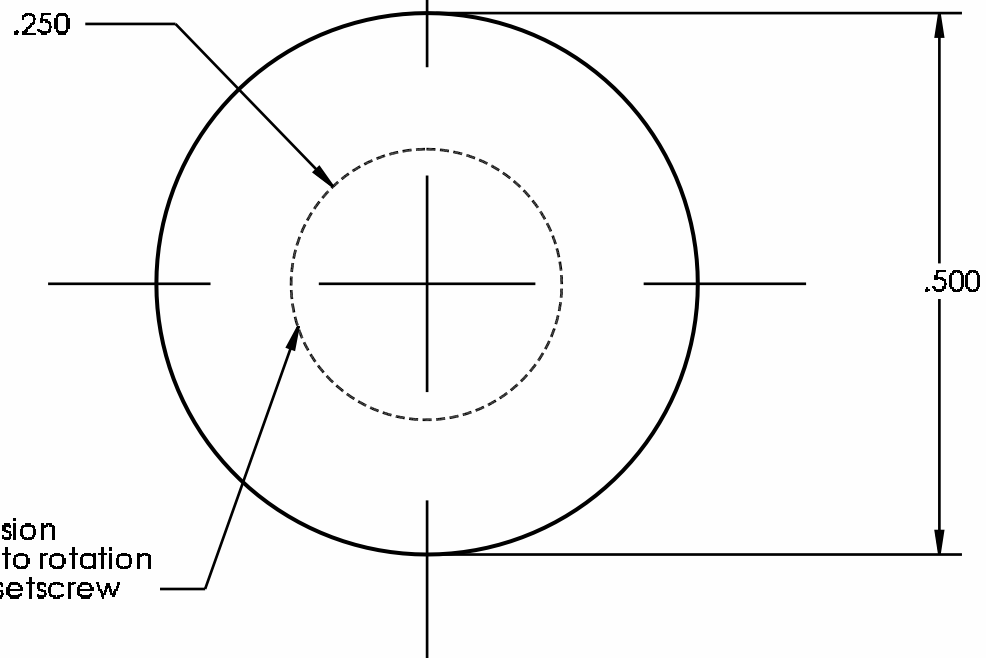
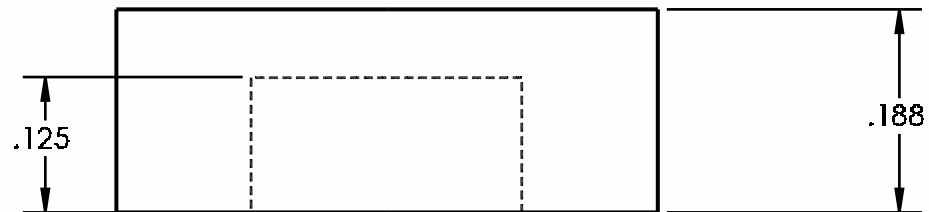
A4



B

c

E

F

.500

Modify dimension
for press fit onto rotation
shafts; or use setscrew

UNLESS OTHERWISE SPECIFIED:
DIMENSIONS ARE IN MILLIMETERS
SURFACE FINISH:
TOLERANCES:
 LINEAR:
 ANGULAR:

FINISH:

DEBUR AND
BREAK SHARP
EDGES

DO NOT SCALE DRAWING

REVISION

	NAME	SIGNATURE	DATE			
DRAWN						
CHECK'D						
APPRO'D						
MFG						
Q.A				MATERIAL:		
				Stainless Steel		
				Q. QUANTITY: 6		

CHK'D

APPR'D

4. FG

64

SIGNATURE	DATE
-----------	------

DATE _____

MATERIAL:	
------------------	--

Stainless Steel

Q U A N T I T Y : 6

TITLE:	
--------	--

Sample Holder

DWG NO.	
---------	--

20101122-sample-holder

SCALE:4:1

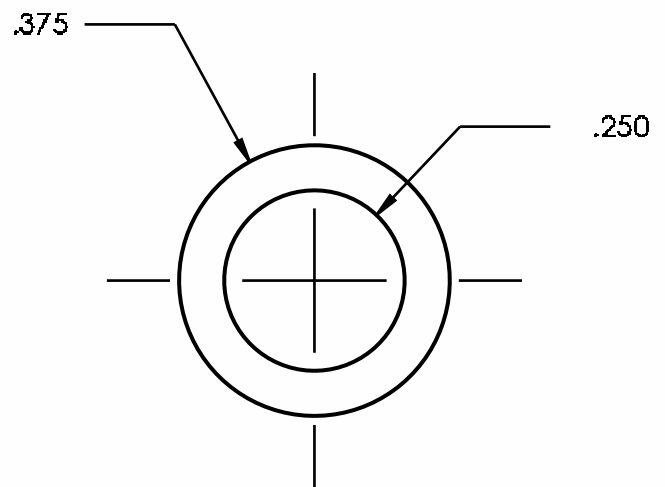
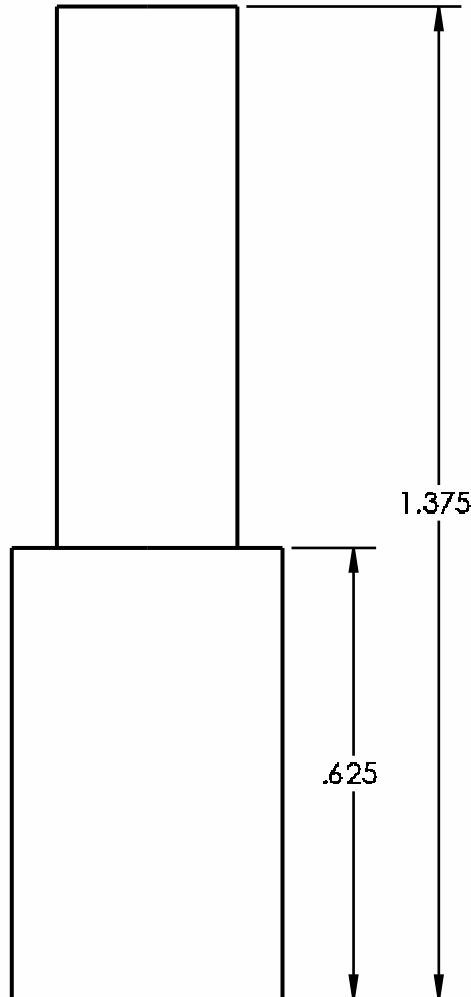
SHEET 1 OF 1

A4

B

c

E

F

UNLESS OTHERWISE SPECIFIED:
DIMENSIONS ARE IN MILLIMETERS
SURFACE FINISH:
TOLERANCES:
LINEAR:
ANGULAR:

FINISH:

DEBUR AND
BREAK SHARP
EDGES

DO NOT SCALE DRAWING

REVISION

	NAME	SIGNATURE	DATE			
DRAWN						
CHECK'D						
APPRO'D						
DATE						
QTY				MATERIAL:		
				Stainless Steel		
				QTY: 1		

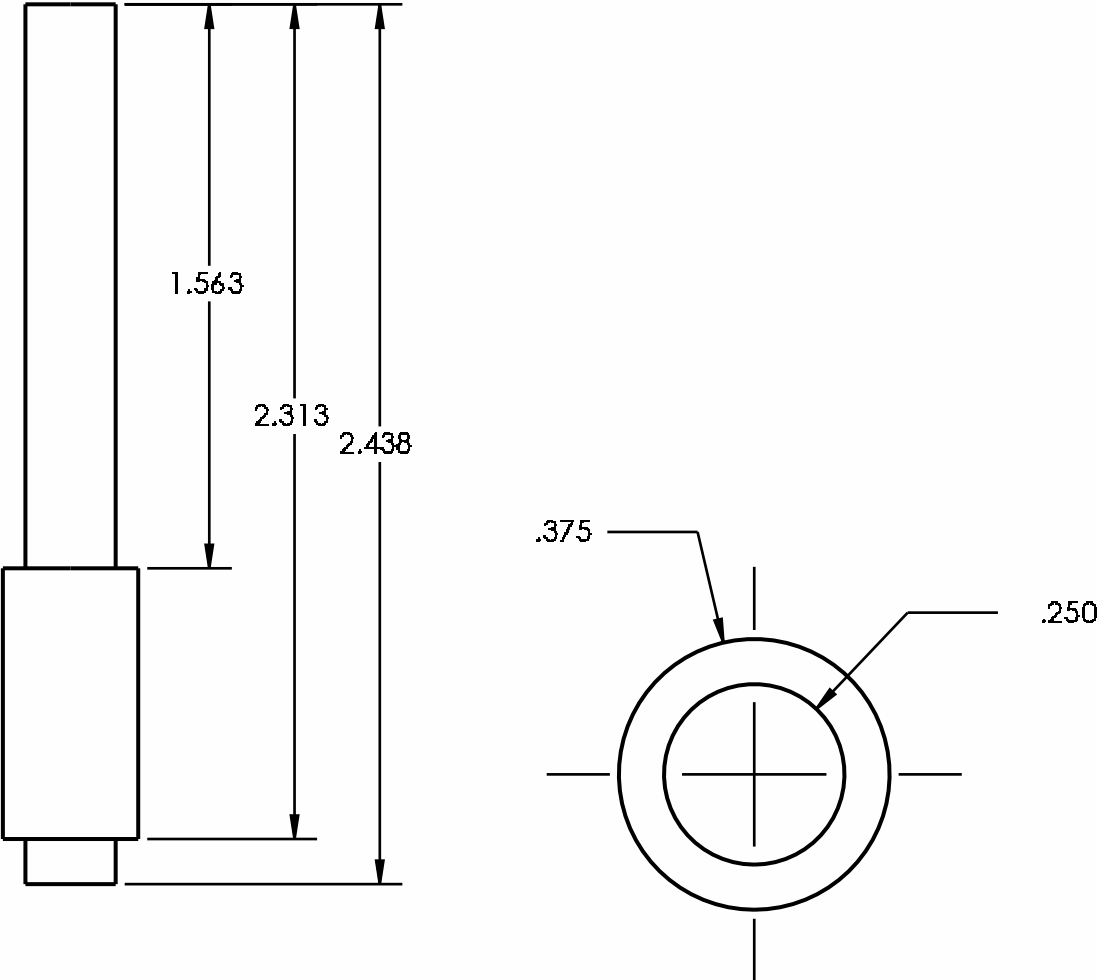
TITLE:	
Rotation Shaft - 01 times	
DWG NO.	A4
20101122-shaft-01-times	
SCALE:2:1	SHEET 1 OF 1

	1	2	3	4
A				
B				
C				
D				
E				
F				
UNLESS OTHERWISE SPECIFIED: DIMENSIONS ARE IN MILLIMETERS SURFACE FINISH: TOLERANCES: LINEAR: ANGULAR:		FINISH:		
DRAWN		SIGNATURE		
CHK'D		DATE		
APP'D				
MFG				
QA				
		MATERIAL:		
		Stainless Steel		
		QTY: 1		
		DEBUR AND BREAK SHARP EDGES		
		DO NOT SCALE DRAWING		
		REVISION		
		TITLE:		
		Rotation Shaft - 1/3 times		
		DWG NO.		
		20101122-shaft-03-recipracol-times		
		A4		
		SCALE: 2:1		
		SHEET 1 OF 1		

Side view of a shaft. The shaft has a total length of 1.50. The top section has a diameter of .13. The middle section has a diameter of .75. The bottom section has a diameter of .94.

Top view of a shaft. The shaft has a diameter of .50. The inner hole has a diameter of .38. The outer diameter of the shaft is .25.

Bottom view of a shaft. The shaft has a diameter of .50. The inner hole has a diameter of .25.

	1	2	3	4		
A						
B						
C	<div></div>					
D						
E						
F	UNLESS OTHERWISE SPECIFIED: DIMENSIONS ARE IN MILLIMETERS SURFACE FINISH: TOLERANCES: LINEAR: ANGULAR:		FINISH:			
			DEBUR AND BREAK SHARP EDGES			
			DO NOT SCALE DRAWING			
			REVISION			
DRAWN		NAME	SIGNATURE	DATE	TITLE:	
CHK'D					Rotation Shaft - 03 times	
APP'VD						
ARG						
Q.A						
				MATERIAL:	DWG NO.	A4
				Stainless Steel	20101115-shaft-03-times	
				QANTITY: 1	SCALE: 2:1	SHEET 1 OF 1

1

3

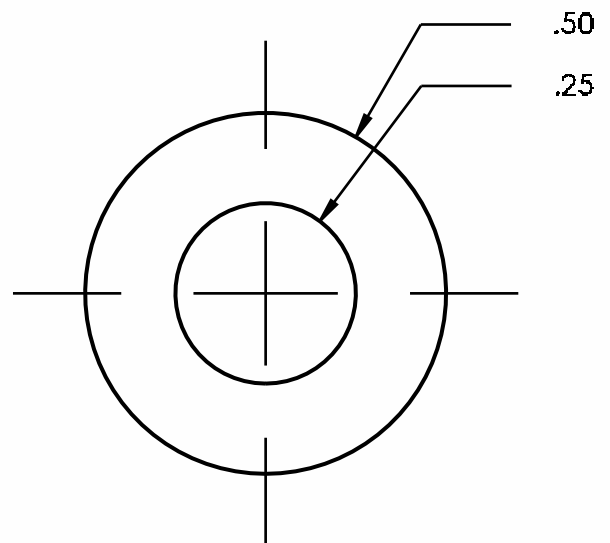
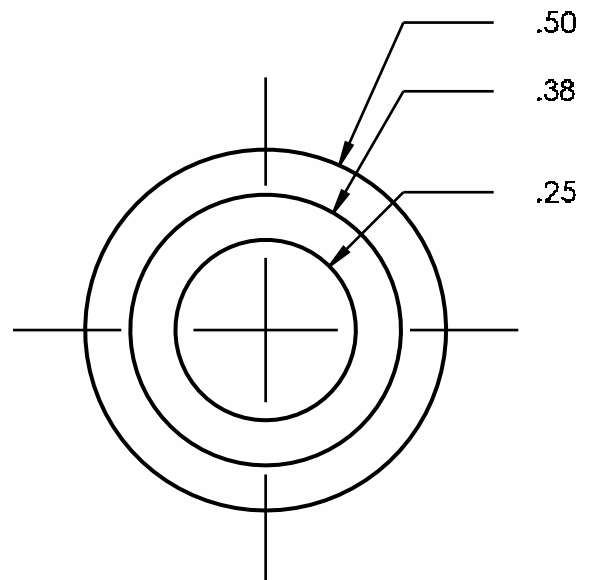
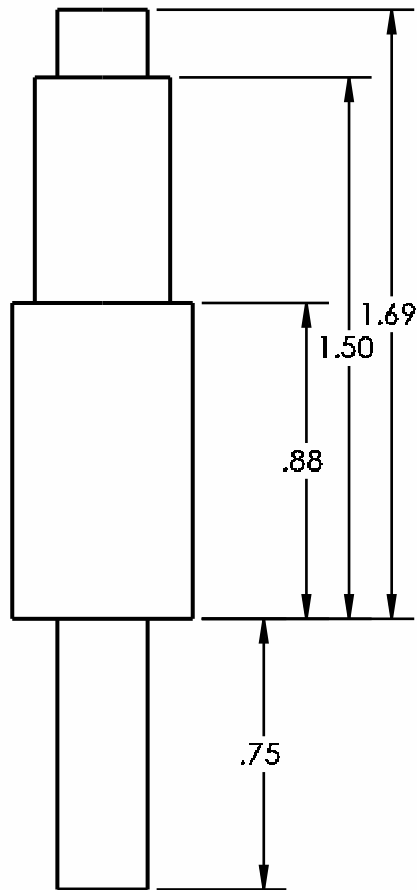
3

4

B

c

E

F

UNLESS OTHERWISE SPECIFIED:
DIMENSIONS ARE IN MILLIMETERS
SURFACE FINISH:
TOLERANCES:
LINEAR:
ANGULAR:

FINISH:

DEBUR AND
BREAK SHARP
EDGES

DO NOT SCALE DRAWING

REVISION

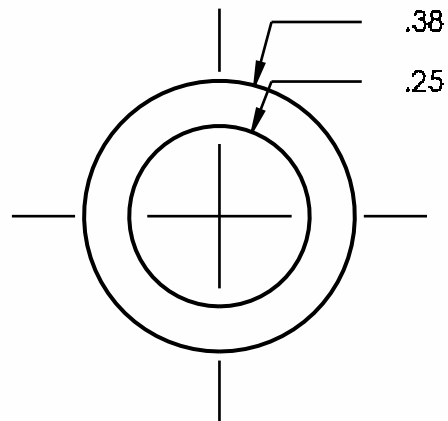
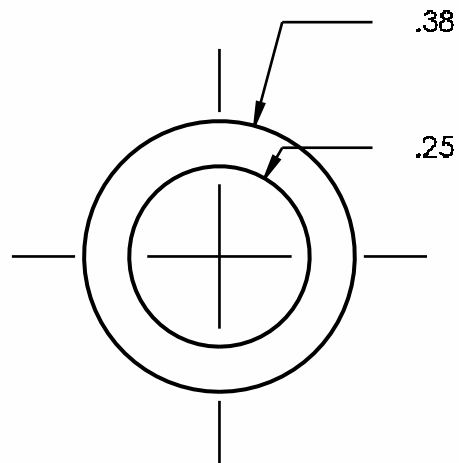
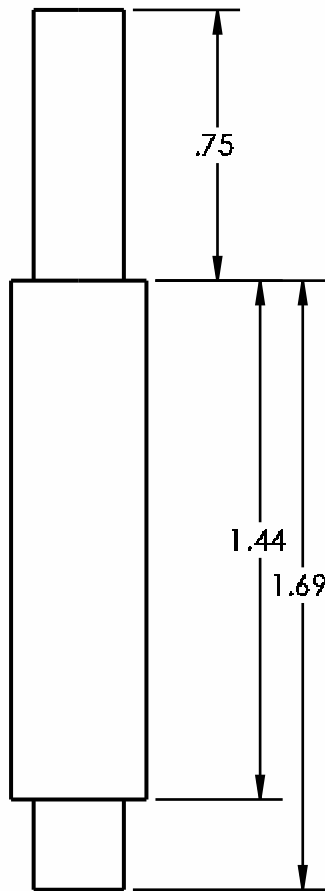
	NAME	SIGNATURE	DATE		
DRAWN					
CHK'D					
APP'VD					
MFG					
Q.A.				MATERIAL:	
				Stainless Steel	
				Q. QUANTITY: 1	

TITLE:	
Rotation Shaft - 06 times	
DWG NO.	A4
20101122-shaft-06-times	
SCALE:2:1	SHEET 1 OF 1

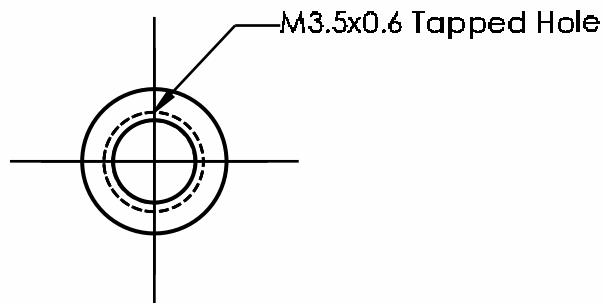
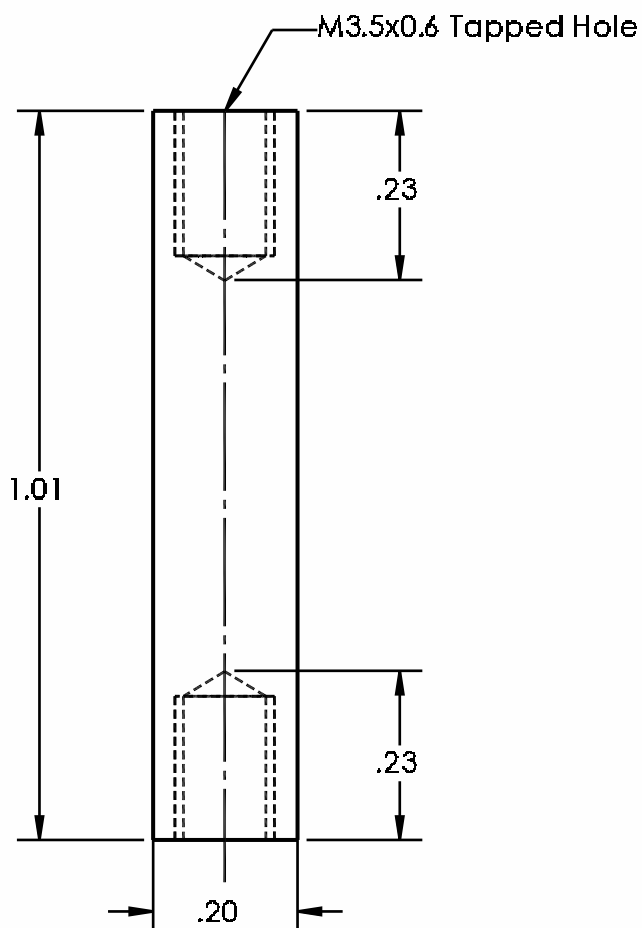
B

c

E

F

UNLESS OTHERWISE SPECIFIED: DIMENSIONS ARE IN MILLIMETERS SURFACE FINISH: TOLERANCES: LINEAR: ANGULAR:		FINISH:		DEBUR AND BREAK SHARP EDGES		DO NOT SCALE DRAWING		REVISION	
NAME		SIGNATURE		DATE		TITLE:			
DRAWN						Rotation Shaft - 16 times			
CHK'D									
APP'D									
MFG									
Q.A.				MATERIAL:		DWG NO.		A4	
				Stainless Steel		20101122-shaft-16-times			
				Q.ANTITY: 1		SCALE: 2:1		SHEET 1 OF 1	

**B**

c

D

E

UNLESS OTHERWISE SPECIFIED:
DIMENSIONS ARE IN MILLIMETERS
SURFACE FINISH:
TOLERANCES:
LINEAR:
ANGULAR:

FINISH:

DEBUR AND
BREAK SHARP
EDGES

DO NOT SCALE DRAWING

REV 5.00 N

	NAME	SIGNATURE	DATE			
DRAWN						
CHECK'D						
APPROV'D						
WFG						

DRAWN

CHK'D

APPRD

4. FG

Q A

MATERIAL:

Stainless Steel

TITLE: Support Post; Middle Plate to Top Plate

DWG NO.	
---------	--

20101122-support-post-middle-to-top

A4

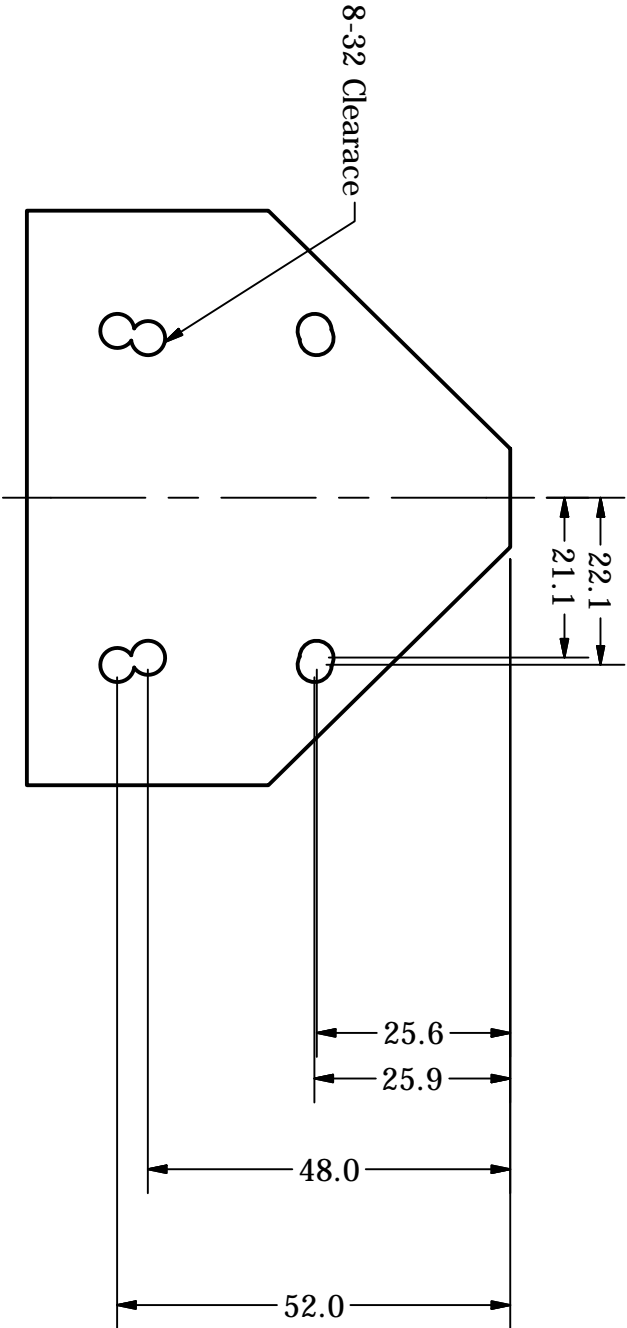
Q U A N T I T Y : F O U R

SCALE:4:1

SHEET 1 OF 1

2

1



B



A

B



A

DRAWN	Josh S	6/4/2011
CHECKED		
QA		
MFG		
APPROVED		

TITLE			
Revisd Rotaion Stage Base			
SIZE	DWG NO		
A	Rotation Stage Bottom Plate (Revis		
SCALE	SHEET 1 OF 1		

2

1

COLOPHON

This document was typeset using the typographical look-and-feel classicthesis developed by André Miede. Miede's style was inspired by Robert Bringhurst's seminal book on typography "*The Elements of Typographic Style*", which I (Joshua) find to be a singularly attractive book. classicthesis is available for both L^AT_EX and L^yX:

<http://code.google.com/p/classicthesis/>

Happy users of classicthesis usually send a real postcard to the author, a collection of postcards received so far is featured here:

<http://postcards.miede.de/>

Final Version as of August 29, 2012 (classicthesis version 1.0).